**Development of Ferrite-coated Soft Magnetic Composites:**

**Correlation of Microstructure to Magnetic Properties**

A Thesis

Submitted to the Faculty

of

Drexel University

by

Katie Jo Sunday

in partial fulfillment of the

requirements for the degree

of

Doctor of Philosophy

June 2017

# Dedications

To my loving parents, Heidi and Milt Sunday. Thank you for everything.

# Acknowledgments

I would like to express my gratitude to my advisor, Mitra L. Taheri, for her persistent encouragement for my research and myself. Without her, none of this would be possible. I have the great fortune of being a member of the DCG research group and would like to thank past members Steven Spurgeon and Ian McDonald, as well as current members Dan Scotto D'Antuono, Wayne Harlow, Matthew Hartshorne, Andrew Lang, Jamie Hart, Adam Falcone, and my numerous undergrad research students. I would also like to thank the MSE department staff and fellow MSE students, Amber Choquette, Alex Krick, and Katie Van Aken. You have all made the past five years at Drexel unforgettable.

Thank you to my committee members, Steve May and Garritt Tucker (Drexel University), James Rondinelli (Northwestern University), and Iver Anderson (Ames Lab/Iowa State University); your guidance and wisdom throughout this process has been greatly appreciated. Thank you to GKN–Hoeganaes Corp., for the constant allowance of materials, equipment, and most valuably, time during my PhD studies. More specifically, thank you to Fran Hanejko, for the endless amount of advice, knowledge, and mentorship you have provided me. Thank you to Kris Darling at Army Research Lab for initial help and support for this thesis work. I would not be here today without the guidance from past teachers, professors, mentors, and friends in the Wilson School District, RPA Engineering, Carpenter Technology, and Polytechnic Institute of NYU. Thank you all for helping me get to where I am today and inspiring me to pursue my PhD.

Last, but always not least, I would like to sincerely thank and extend my deepest gratitude to my family and fiancé. To my parents, thank you for always supporting me and being by my side every step of the way. To Kathleen, I am forever grateful for your patience, love, and encouragement, and look forward to what the future has in store for us.

# Table of Contents

# List of Tables

# List of Figures

## Abstract

Development of Ferrite-coated Soft Magnetic Composites:
Correlation of Microstructure to Magnetic Properties
Katie Jo Sunday
Mitra L. Taheri, PhD

Soft magnetic composites (SMCs) comprised of ferrite–coated ferrous powder permit isotropic magnetic flux capabilities, lower core losses, and complex designs through the use of traditional powder metallurgy techniques. Current coating materials and methods are vastly limited by the nonmagnetic properties of organic and some inorganic coatings and their inability to withstand high heat treatments for proper stress relief of core powder after compaction. Ferrite–based coatings are ferrimagnetic, highly resistive, and boast high melting temperatures, thus providing adequate electrical barriers between metallic particles. These insulating layers are necessary for reducing eddy current losses by increasing resistivity in order to improve the overall magnetic efficiency and subsequent frequency range. The goals of this work are to correlate ferrite–coated Fe powder composites microstructure for the coating and core powder to magnetic properties such as permeability, coercivity, and core loss.

We first explore the relevant concepts of SMC materials from their composition to processing steps to pertinent properties. This thesis employs a suite of characterization techniques for powder and composite properties. We use X-ray diffraction, scanning electron microscopy, and transmission electron microscopy to provide a complete understanding of the effect of processing conditions on ferrite–coated Fe–based SMCs. Magnetic, mechanical, and electrical properties are then analyzed to correlate microstructural features and determine their effect on such properties.

In the second part of this thesis, we present a proof of concept study on $Al_2O_3$– and $Al_2O_3$–$Fe_3O_4$–coated Fe powder composites, illustrating magnetization is highly dependent on ferromagnetic volume. We then expand on previous work to compare an ideal, crystalline state using $Fe_3O_4$–Fe thin film heterostructures to a highly strained state using bulk powder studies. $Fe_3O_4$–coated Fe composites are produced via mechanical milling and analyzed for magnetic core loss dependence on

particle size, cure temperature, and microstructure of both coating and core powder. We present a significant increase in core loss related to eddy current loss from coating particles sintering and Fe grain growth. Lastly, a more resistive coating material, NiZnCu–ferrite, is applied for improved resistivity, which leads to lower eddy current loss and improved magnetic performance. By highlighting the importance of microstructure and composition on magnetic properties, a closer look at interfacial features and local microstrain are necessary and accomplished in this work. Future developments of ferrite–based SMC coatings are required to transform the use of electromagnetic devices in today's society.

# Chapter 1: Introduction

## 1.1 Motivation

Our world is focused on making devices faster, lighter, and more innovative; why should electric motors be any different? Electric motors convert electrical energy to mechanical energy using direct current (DC) from stored energy, say in batteries, or alternating current (AC) from generators or the power grid. They are found in electric cars, small household appliances, industrial fans and pumps, machine tools, as well as in large ships and planes for propulsion. Current motor designs use silicon-steel laminations, with thicknesses ranging from 200 $\mu$m to 1000 $\mu$m, with insulating coating materials or air gaps in between each layer (Fig. 1.1) to reduce current flow from one layer to another, in order to minimize undesired eddy currents. Continually reducing lamination thickness has been the primary method to decrease eddy current losses; however, a limit has been reached that has sharply increased manufacturing costs and complexity. For these reasons, utilizing ferrous powder in place of strip material to reduce eddy current paths by introducing a resistive coating is the next iteration for improving electric motor efficiency and increasing the frequency range for electromagnetic applications.

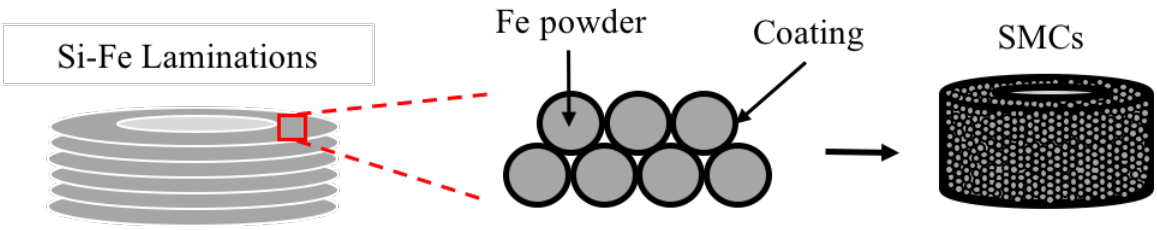


**Figure 1.1:** Traditional silicon steel laminations with air gaps to be replaced by electrically insulated ferrous powder then compacted and cured to form a soft magnetic composite (SMC).

Soft magnetic composites (SMCs) comprised of electrically insulated ferromagnetic powder (Fig. 1.1) have several worthy advantages to traditional steel laminations used in many electric motors still today, which overheat and fail at high applied frequencies (>400 Hz) [1, 12, 13]. Exceeding these limits lead to eddy currents dominating, resulting in overheating. By introducing powder metallurgy

(PM) techniques to process these systems, thicknesses of the conductive material are reduced and therefore core loss values are minimized, ultimately improving electrical efficiency. Advantages of SMCs include but are not limited to, three-dimensional magnetic flux carrying capabilities, thermal isotropy, high magnetic permeability, low total core losses, structural freedom for complex designs, and decreased size/costs [1, 14–16]. In addition, manufacturing cost and waste material can be reduced since minimal processing steps are required and subtractive methods are not necessary. Electrically insulating each ferrous particle with a coating material allows for minimal eddy current build-up and thus reduced core losses, which control the operating frequencies of these materials. In addition, the nature of powder metallurgy allows customers to reduce the material consumption with a smaller motor design or obtain more power from similar dimensions as their lamination competitors, which opens up an enormous market for electromagnetic devices [17]. These components have the ability to bridge the gap between traditional laminated steel cores limited to frequencies of a few hundred Hz and ferrite cores limited to above a few MHz (Fig. 1.2). The elimination of failure/overheating of electromagnetic devices often because of eddy current buildup resulting from poor insulation of ferromagnetic layers can be completed with SMC materials [18]. However, the limiting factor of current SMC designs is the insulating materials inability to withstand post-compaction heat treatments, which leads to metal-on-metal contact points and thus large eddy current paths [1, 19]. Continuous research on SMCs has shown their vast potential for direct current (DC) and alternating current (AC) applications that improve the magnetic induction of core materials at low to high applied frequencies by allowing new innovative designs developed by engineers.

A well-known and highly referenced review on soft magnetic composite materials was published by H. Shokrollahi and K. Janghorban in 2007 [1], which highlights much of the theory behind these material systems. During the last decade, studies have focused on increasing magnetic permeability and lowering core losses of SMCs to result in higher frequency applications, nominally from 400 Hz to a few kHz [4, 20–28]. Various applications of soft magnetic composites have been recently studied, including two types of permanent magnet synchronous motors (Fig. 1.3a) – transverse flux motor (Figure 1.3b) and claw pole motor [3, 29, 30], two types of crankshaft induction hardening coils –

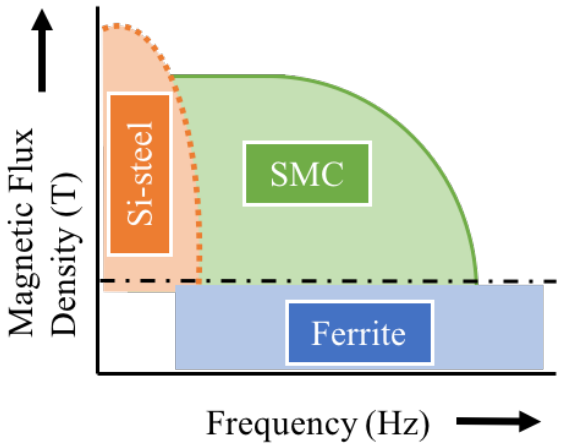


**Figure 1.2:** Diagram illustrating potential range of magnetic flux density and frequency for SMC materials.

elotherm (rotational) and clamshell (non-rotational) [24, 31, 32], and brushless DC motors [33, 34], to name a slight few. A high magnetic induction and low coercivity are necessary to increase permeability and efficiency, obtained by having minimal structural boundaries so that magnetic domains can move easily and reduce the required energy input to obtain similar magnetic responses. Lowering core losses is completed by reducing hysteresis and eddy current losses, simultaneously. This is obtained by having the least amount of nonmagnetic inclusions and a high electrical resistivity while maintaining good mechanical strength. In this thesis we use high purity ferromagnetic powder as the core material and a thermally stable, electrically resistive coating material, to reduce core losses. However, the addition of a nonmagnetic coating layer will greatly reduce the overall magnetic permeability, which yields a problematic balance of properties. For this reason, soft ferrites are studied as an insulating coating of the ferrous powder in this thesis.

## 1.2 Problem Statement

The continuous development of SMCs is crucial for potential electromagnetic device applications at high applied frequencies. SMCs incorporate electrically insulated particles with the capability of high magnetic permeability and low core losses depending on material selection, processing, and curing temperature. The predominant limiting factor in current SMC designs is the thermal insta-

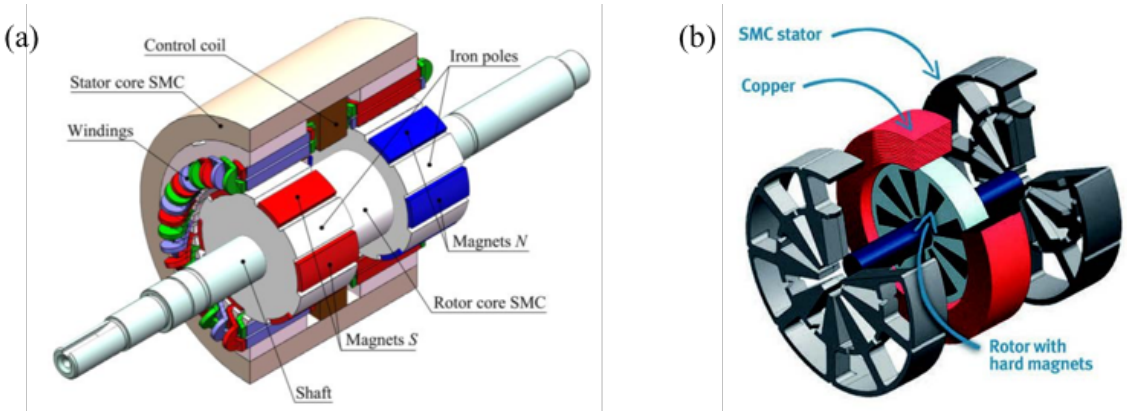


**Figure 1.3:** Two synchronous motor designs using SMC materials, (a) new design developed by Barba et al. [2] and (b) transverse flux motor developed by GKN Sinter Metals [3].

bility of the coating material at high curing temperatures, which leads to large eddy current paths and potential failure from overheating [1]. The coating material needs to be electrically insulating, thermally stable, and compressible at low compaction pressures and iron stress-relieving temperatures (570°C–775°C). Organic coatings, including epoxy resins and silicone polymers, have been extensively studied as binders to allow for high densities and resistivity, because they are capable of completely isolating ferrous particles. However, these materials cannot withstand post-compaction heating above 450°C before they begin to degrade [35, 36]; ultimately leading to high electrical conductivity from metal–on–metal contact points. Low magnetic saturation ($B$<0.65 T) and low magnetic permeability (<225) are result of dislocations remaining in Fe and large amounts of non-magnetic regions, from not reaching higher temperatures [35]. Organic coatings are thus not viable for applications requiring low coercivity and low eddy current loss because the internal strain and dislocations brought on by compaction cannot be relieved via curing below 500°C and remain insulating [19, 37–39]. Therefore, inorganic coatings (mostly oxides), are more suitable due to higher thermal stability and improved soft magnetic properties if minimal coating material is applied or a ferrimagnetic material is used [40–43]. These coating materials consist of phosphates [44], magnesium oxide (MgO) [45, 46], silica ($SiO_2$) [20, 40], alumina ($Al_2O_3$) [41, 47], and ferrites [42, 43]. Ceramic materials have high melting points and are electrically insulating, corrosive and wear resistant, making them good coating selections [41]. These materials however, are dia- or antiferromagnetic which

decrease magnetic permeability considerably by decreasing the overall magnetic volume [48]. Therefore materials that exhibit ferro- or ferrimagnetism are optimal for soft magnetic applications as core and coating materials.

Ferrite-coated ferromagnetic powder compacted and cured are advantageous over traditional steel laminates because of reduced core losses, high permeability, good green strength, and formability for complex designs [14–16, 28]. Ferrite coatings have improved magnetic and electrical properties as compared to organic coatings and ceramic materials [15, 35]. However, there is a lack of proper stress relieving temperatures, small particle sizes, and thermally unstable coating materials previously used in literature, leaving room for numerous processing parameter improvements to the field. A balance between ferromagnetic volume and electrically resistive coating layers that allows for maximum permeability and density, while minimizing core loss has yet to be determined. In addition, the effect of interfacial microstructure on magnetic properties have yet to be determined via powder systems. A large component of this field is not only the materials, but equally important are the processing methods employed to obtain the final part geometries and desired properties. Research to date has been limited by non-uniform coating layers, expensive methods, and low curing temperatures. All of these downfalls permit various material and processing parameter improvements for future SMCs. Soft ferrites are the only class of inorganic materials that allow for high electrical resistivity while maintaining good magnetic properties and keeping costs low [49]. One of the more important challenges faced today is the ability to control the coating process and allow for sufficient isolation of ferrous particles throughout the processing steps. Our research studies the effects of ferrite coatings on Fe powder by comparing crystalline thin films to bulk powder studies utilizing simple mechanical milling techniques. Previous work by McDonald [11] and Spurgeon [50] are used to compare uncapped $Fe_3O_4$–Fe–MgO heterostructures to the work presented in this thesis of La capped $Fe_3O_4$–Fe–MgO heterostructures.

First, we must understand the current state of this research field and how we can improve on this knowledge to advance the field of soft magnetic composites for electromagnetic device applications. Several groups study the use of soft ferrite coatings on ferrous powder, but there is a lack of under-

standing of core powder and coating microstructure on the magnetic and electrical properties. In addition, often groups use expensive and time consuming methods for production of ferrite coatings, which will be difficult to scale up to a production setting. Highlighted studies will now be discussed.

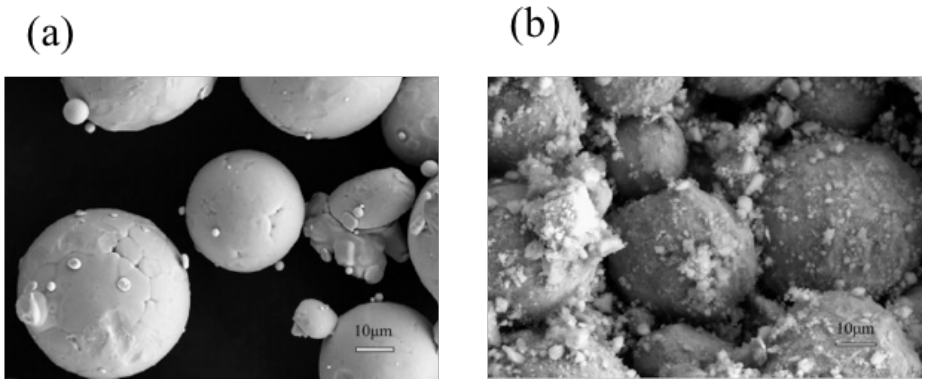


**Figure 1.4:** Fe powder before coating (a) and after coating (b) with NiZn–ferrite nanopowder [4].

Several research groups have studied $Fe_3O_4$–coated Fe powder SMCs [18, 43, 51–53]. Zhao et al. used acidic bluing and surface oxidation to obtain $Fe_3O_4$ coated Fe powder [43, 51]. Subsequent annealing temperatures were limited to below 500°C for 1 h after compaction at 800 MPa. Low permeability was found for surface oxidized powder and low magnetization for the acidic bluing process. These results are most likely found because of the small particle sizes used and the stressed internal microstructure from low curing temperatures, both are not discussed. Xu et al. used very high compaction pressures (∼1.7 GPa) and curing temperatures (750°C) for annealed Fe–Si–Ni powder, ball-milled then coated with phosphate, which resulted in improved magnetic properties most likely from higher densities and internal stress relief, although microstructure, density, and coating layer thickness were not reported on [22]. Peng et al. coated pure Fe powder with $Ni_{0.5}Zn_{0.5}Fe_2O_4$ particles via ball-milling techniques, then subsequently microwave annealed the powder at 800°C for 30 min, compacted at 1 GPa, and microwave annealed again [54]. Once again, high compaction pressures were used to improve sintered density; however, microwave annealing did not allow for internal stress relief because Fe weakly absorbs microwave energy. Likewise, powder core microstructure and coating thickness were not elaborated on. Similar material systems, Fe ($d_{ave}$∼20 to 40 $\mu$m) and 10 wt% $Ni_{0.5}Zn_{0.5}Fe_2O_4$ ($d_{ave}$∼40 nm), used spark plasma-sintering (SPS) with lower compaction

pressures of 600 MPa; however, samples had very lower magnetization ($B$=1.65 T) as a result of low density [4]. The low magnetization is also attributed to the small Fe particle size, spherical shape, and non-uniform coating shown as agglomerations on Fe in Figure 1.4. Most coating studies use Fe particle sizes below 50 $\mu$m, which result in lower magnetization because of more particle boundaries hindering domain wall movement. In addition, if spherical particle shapes are used, lower density from lack of mechanical interlocking will almost always result, unless expensive and time consuming processing methods are used to combat this. All studies have reported low core losses; however, toroid samples were not tested at maximum induction ($\sim$1 T), most used below 100 mT [22, 40, 51]. Therefore, these results do not allow for proper comparison to industry standard testing procedures. All research discussed here did not elaborate on the effect of coating microstructure on magnetic or electrical properties.

Outstanding questions from state of the art consist of the following:

1. How does the microstructure of the core powder and coating layer thickness affect soft magnetic properties of a ferrite–coated SMC component?

2. Can low compaction pressures be coupled with high curing temperatures for large particle sizes and allow for proper stress relief to obtain high magnetic permeability and low core loss?

3. Can traditional powder metallurgy processes (dry coating methods, die compaction, and sintering temperatures) be used for ferrite–based coatings on Fe SMCs?

This thesis studies the effect of microstructural defects, namely grain size, dislocations, and strain, and coating layer thickness of Fe–ferrite heterostructures on soft magnetic properties such as magnetization, permeability, coercivity, and core loss. Three coating materials are studied, $Al_2O_3$, $Fe_3O_4$, and NiZnCu–ferrite, to express the effects of various magnetic and electrical properties on Fe SMCs.

A complete understanding of structural and magnetic behaviors of the material systems is necessary to optimize the desired properties of SMCs from a powder and composite point-of-view. A proof of concept study uses $Al_2O_3$ as a coating material on Fe powder with various coating concentrations

developed via high energy ball milling. $Fe_3O_4$–Fe thin film heterostructures are used to compare interfacial microstructural defects to magnetic saturation for highly crystalline (epitaxial) materials, essentially replicating a coating/iron interface in an ideal state. Comparing thin film bilayers to Fe powder and micron-sized ferrite particles will allow for the magnetic property dependence on microstructural defects to be determined. Coated iron powder is produced using traditional powder metallurgy techniques to form toroid shaped composites for magnetic comparison to thin film bilayers.Lastly, a more resistive coating material (NiZnCu-ferrite) is applied to Fe powder and analyzed for optimum magnetic properties and frequency range. All studies help determine the dependence of microstructural defects in the core and coating layers to magnetic properties, from the ideal state (thin films) to a highly strained state (powder composites). The goals of this thesis utilize a wide-array of processing methods and characterization techniques, which will be discussed in subsequent sections, to analyze structure–property relationships of these magnetic material systems.

## 1.3 Organization of the Thesis

This thesis is organized into the following structure:

**Chapter 2 - Background** In this chapter we introduce the necessary concepts pertaining to magnetic permeability and core loss with respect to structural material properties. We illustrate the importance of magnetic characterization and how structural properties affect magnetic response. Various powder metallurgy techniques are discussed with respect to SMC development. Lastly, we discuss the effects of various material systems, pertaining to the core and coating regions used in SMCs in order to optimize frequency applications and flux density simultaneously.

**Chapter 3 - Techniques and Methods** In this chapter we describe the processing methods for developing the various material systems in thin film, powder, and composite form. We describe the experimental methods for coating Fe powder and obtaining test pieces for evaluation of electrical, magnetic, mechanical, and microstructural properties. We conclude with brief explanations pertaining to specific characterization techniques employed for this thesis.

**Chapter 4 - Alumina Coatings** A proof of concept study is described in this chapter, for applying a coating material to iron powder via mechanical milling methods, nominally high energy ball milling. We present iron powder that is mechanically milled with alumina media, to yield plastically deformed, $Al_2O_3$–coated iron particles. Various milling times and media ball sizes are investigated to maintain particle size, insulate powder uniformly, and optimize magnetic properties after compaction and curing. Powder and composites are measured for magnetic saturation, elastic modulus, and hardness to be compared to image analysis of particle shape and size. Additionally we describe the effect of magnetite particle additions to the $Al_2O_3$–coating layer on magnetic saturation and layer thickness.

**Chapter 5 - $Fe_3O_4$ Coatings** In this chapter thin film $Fe_3O_4$–Fe bilayers are initially studied for comparison of interfacial microstructural defects of varying film thickness to magnetic saturation measurements. This work compares uncapped thin films to La capped thin films for isolation of surface oxidation. The highly crystalline state is then compared to highly strained state of ball milled Fe for a solid comparison of strain to magnetic properties.

In the second part of this chapter we present a thin film replication study of the coating–core interface for $Fe_3O_4$ and Fe, respectively, using bulk materials. We analyze the effect of coating layer thickness and microstructure for a highly strained state. Various Fe particle sizes are used and coated with magnetite particles by means of mechanical milling in this study. We demonstrate the effect of iron particle size on density, mechanical strength, and magnetic properties such as permeability, coercivity, and core loss. We determine medium particle sizes cured at 700°C allow for the best overall properties, relatively high density, good permeability, and low core loss.

In the third part of this chapter we highlight the dependence of coating microstructure and magnetic properties using higher temperatures, nominally 700°C to 1000°C, for $Fe_3O_4$–coated Fe powder composites. We present a significant increase in core loss related to eddy current loss at low frequencies for these material systems. We attribute the increase in core loss to Fe grain growth and densification of coating particles leading to reduced grain boundaries

in coating layers. We illustrate the importance of both core and coating microstructure and composition on structure–sensitive properties such as coercivity and remanent induction.

**Chapter 6 - NiZnCu–ferrite Coatings** In this chapter we utilize the parameters best-suited for ferrite–coated Fe powder developed throughout the thesis. We now compare three coating amounts to optimize magnetic permeability and core loss simultaneously. This chapter uses more resistive NiZnCu–ferrite as a coating material of 5 wt%, 10 wt%, and 15 wt% on Fe powder of particles sizes above 75 $\mu$m. We study magnetic measurements under increasing frequency to determine the optimal application ranges for each material system.

**Chapter 7 - Conclusions and Future Work** In the final chapter we summarize the primary findings for each coating material studied in this thesis. We explain the importance of coating composition, microstructure, and resistivity along with core powder microstructure on magnetic properties for SMC materials. Lastly, we suggest future work to be completed as a continuous of these studies.

# Chapter 2: Background

## 2.1 Introduction

The development of more efficient and cost effective electromagnetic devices is crucial in today's society. Inductors, transformers, and electric motors are prime examples of how advancements to their design and materials can improve everything about them, such as weight, speed, and cost. A few disadvantages to electric motors are the concepts of core loss, low resistance, and overheating [55] that lead to failure at high applied frequencies, nominally 400 Hz for aerospace motors [13]. All three drawbacks are related to the motor core, mostly the rotor and stator components traditionally comprised of silicon steel laminations, or more recently soft magnetic composites (Fig. 1.3). SMCs incorporate ferromagnetic particles coated with electrically resistive materials that are compacted and cured [56]. SMCs permit low core losses and high magnetic permeability at various frequency ranges for diverse applications such as aerospace and automobiles. The future of SMCs lies in balancing high electrical resistivity, high mechanical strength, and high magnetic performance utilizing both a core and coating material.

A comparison of research studies from literature to commercially available materials is shown in Table 2.1 for resistivity, strength, and DC magnetic properties and Table 2.2 for core loss comparison. Low induction and permeability indicate that there has been no significant improvements over the past few years to effectively replace lamination steels. Although Frayman et al. present the lowest core loss values at 50 Hz, a permeability of 190 is too low for significant improvement over lamination steels [25]. Further improvements, but more importantly understanding of these systems are needed for future SMC developments. A core material that allows for the highest magnetic permeability, obtained by having a high density, low coercivity, and high magnetic induction, coupled with a coating material that allows for low core losses, obtained by having a high electrical resistivity and good magnetic capability, will be the ideal solution for SMC applications. The fields of soft magnetic composites and powder metallurgy have powerful potential to redesign the way we use

electromagnetic devices, and will continue to grow for years to come.

**Table 2.1:** Properties of existing soft magnetic materials compared to literature.

| Sample | Resistivity ($\mu\Omega$·m) | TRS (MPa) | Induction @ 10,000 A·m$^{-1}$ (T) | $\mu_{max}$ |
|---|---|---|---|---|
| 1P Somaloy 130i [57] | 8000 | 35 | 1.40 | 290 |
| 5P Somaloy 700 HR [57] | 700 | 60 | 1.57 | 600 |
| AncorLam (450°C) [25] | – | 124 | – | 500 |
| $Fe_3O_4$–epoxy–Fe [18] | 280 | – | 1.35 | 309 |
| Novel coating (100% $N_2$ at 650°C) [25] | – | 33 | – | 190 |
| Novel coating (Modified Atm) [25] | – | 28 | – | 190 |

**Table 2.2:** Core loss of existing soft magnetic materials compared to literature.

| | Core loss @ 1 T (W·kg$^{-1}$) | | | |
|---|---|---|---|---|
| **Sample** | **50 Hz** | **100 Hz** | **400 Hz** | **1000 Hz** |
| 1P Somaloy 130i [57] | – | 12 | 54 | 145 |
| 5P Somaloy 700 HR [57] | – | 6 | 32 | 104 |
| AncorLam (450°C) [25] | 6 | – | 59 | 170 |
| $Fe_3O_4$–epoxy–Fe [18] | – | 19 | 91 | 206 |
| Novel coating (100% $N_2$ at 650°C) [25] | 5 | 60 | – | 180 |
| Novel coating (Modified Atm) [25] | 4.5 | 40 | – | 110 |

The objective of this research is to study the effect of microstructure of the coating and core material on magnetic permeability and core loss and develop a material system with low core loss, high magnetic permeability, and good mechanical strength for tunable frequency applications. Lattice defects, most notably dislocations, and elemental impurities are the most influential microstructural component to electrical and magnetic properties of powder cores [58]. Microstructure parameters such as grain size, defect density, and strain state are analyzed in the core powder and near the coating–core interface to obtain high soft magnetic properties and electrical resistivity. This research studies the coating material via a suite of ferrimagnetic coatings, namely ferrites, to fine tune coating layer thickness and stoichiometry for improved properties. The interfacial region is studied through both fundamental and applied experimental techniques to determine the role of these microstructural features and their effect on magnetic properties. We specifically concentrate on grain size, dislocation densities, and microstrain, discussed in the subsequent sections as these defects pertain to specific magnetic properties. This new understanding leads to improved control of coating and core parameters for lower core losses and higher magnetic permeability of SMCs. We first must introduce the necessary information to understand each property, how they are characterized, and

in what instances they are significant.

## 2.2 Magnetic Properties

### 2.2.1 Hysteresis Loop Characterization

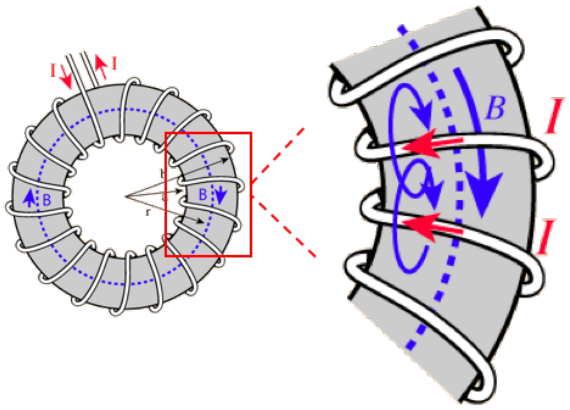


**Figure 2.1:** Schematic diagram of toroid test in which current is applied to copper winding and a magnetic field is induced in the sample.

To characterize a material for a magnetic response we introduce the concept of magnetism, essentially an electric charge ($e^{-1}$) in motion will create a magnetic field [59]. Therefore we can introduce an electric current to a material system causing a path of moving electrons, which generates a magnetic response from the magnetic spins rearranging in the material. These magnetic spins will attempt to rearrange to align with the applied field, but microstructural defects, chemical impurities, and magnetic energies may hinder these movements [58]. Internal magnetic energies at play include magnetostatic, magnetocrystalline, and exchange energy [59]. For BCC Fe, the magnetization will attempt to align with the easy axis (100), determined by spin–orbit coupling and the least close-packed direction. This competing energy is termed magnetocrystalline energy, in which the magnetic spins tend to align with a preferred crystallographic direction. A second contending energy is exchange energy, where electron spins are inclined to align together, favoring single domain formation. The origin of this energy is Coulomb repulsion [60]. However, a single magnetic domain will act as a magnet, creating an external demagnetizing field, leading to the third energy of importance. Magnetostatic energy attempts to reduce any field outside the material, and tends to form multi-domain structures. These three energies are competing with one another to

form an internal magnetic domain structure. Now, when an applied field is introduced, a fourth external energy tries to align the magnetic spins with the applied field, called Zeeman energy [59]. All of the magnetic energies are involved with magnetizing a material and are greatly affected by the composition and microstructure of the sample. The determination of individual energy contributions for the material systems studied are beyond the scope of this thesis.

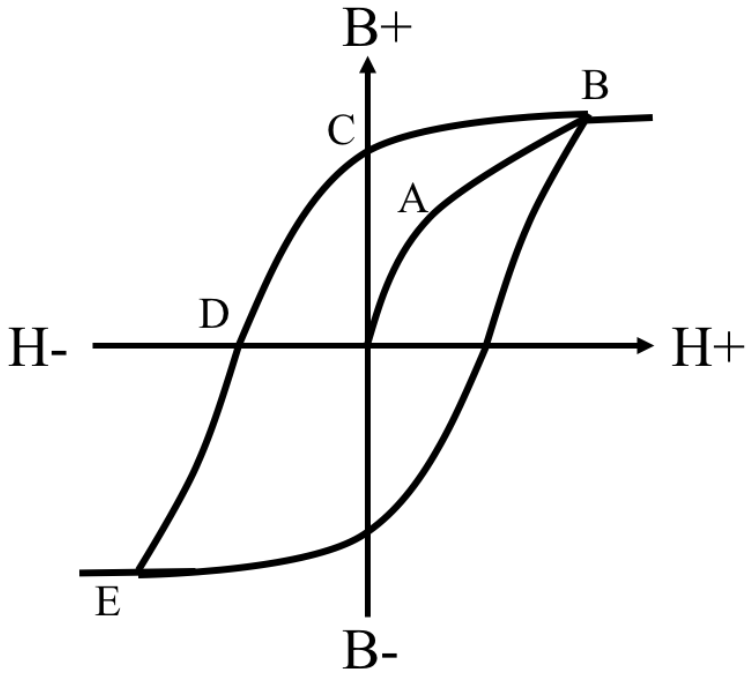


**Figure 2.2:** Schematic drawing of hysteresis loop. Initial magnetizing curve (A) corresponds to domain movement, while (B) corresponds to spin rotation and point C represents remnant induction ($B_r$), point D represents coercivity ($H_c$), and lastly point E represents negative saturation.

We now explain the method to which a material is tested and the responding properties of importance for this thesis. For simplicity purposes, we will describe magnetic testing as a hysteresis loop is obtained for a toroid shaped sample, to illustrate the properties of interest. A material is first subjected to a positive current through the primary windings (Fig. 2.1), which results in a voltage difference observed in the secondary windings, measured by a fluxmeter. As we increase the current, the magnetic response in the material also increases because the magnetic domains begin to move, in order to best align with the applied field. This action causing the domain boundaries to actually

move and maximize the domain area [58]. This motion of domain walls is highly dependent on intrinsic material properties, such as microstructure and impurities, discussed later on. Any defect or nonmagnetic inclusion will greatly effect the domain wall motion and subsequently pin walls at these regions, making it more difficult to magnetize a material. We can illustrate the actions of the domains by an arbitrary hysteresis loop seen in Figure 2.2, where the initial increase in magnetic response (part A) is attributed to the movement of magnetic domains. Once the domains are fully pinned with respect to various imperfections, the magnetic spins within the domains will attempt to rotate and align with the applied field [59]. A material is said to be saturated when the domain wall motion has maximized domain size and all spins within those domains have aligned with the applied field to the best of their ability. This is seen when the graph levels out, or slope equals zero (part B), even as the field is being increased; the value of magnetic flux ($B$) at which this occurs is termed the magnetic saturation ($M_s$). The relationship between $B$ and the applied field ($H$) indicates how easily a material is magnetized, clearly effected by composition and microstructure. An important property is called permeability ($\mu$), which is the ratio of $B$ to $H$ [59]. Permeability is unitless since both $B$ and $H$ are measured in Gauss (G) or Oersted (Oe), which are equivalent. For this thesis, maximum permeability ($\mu_{max}$) is used, which is the highest slope of the initial magnetizing curve seen in part A of Figure 2.2.

The process of obtaining a complete hysteresis loop is needed to determine important magnetic properties to fully characterize a materials capabilities. After saturation has been completed, the applied current is removed and applied in the opposite direction. The response of the material during this stage in the hysteresis loop is critical for characterizing "soft" and "hard" magnetic potential. The hysteretic nature of a loop is result of a materials ability to retain the same magnetic structure before and after it is magnetized. As the domains begin to move and spins attempt to realign to the opposite field, a certain amount of spins will remain aligned with the initial field even as the overall applied field becomes zero. As the curve crosses back over the y-axis, seen at point C in Figure 2.2, a certain remnant induction ($B_r$) is still present. As the applied field continues to increase in the opposite direction, the material will reach a point where the spins will all cancel out and the

material has a net magnetization of zero (part D). If this occurs at a low applied field (<10 Oe) a material is said to be magnetically "soft". If a higher applied field (>1 kOe) is needed to reach zero net magnetization, a material is described as being magnetically "hard". This property is termed coercivity ($H_c$) and is defined as half of the width of the hysteresis loop at zero magnetic induction ($B$=0). Further increasing the current in the opposite direction will further saturate the material to a negative value (part E), comparable to the initial magnetization (part B). The hysteresis loop is completed by once again reversing the applied field and increasing back in the original direction to subject the domains and spins to realign with the field. Now that we have a firm understanding of the basic magnetic hysteresis loop, we can discuss the significance of specific microstructural features on magnetic characterization.

### 2.2.2 Magnetic Permeability, Coercivity, and Saturation

#### Role of Chemical Composition and Purity

Structure sensitive properties such as permeability, coercive force, and residual magnetism are greatly affected by impurities and chemical composition [58]. Interstitial impurities (H, C, N, and O) are used in Fe for a variety of reasons. For strengthening Fe, carbon is preferred as opposed to hydrogen which may lead to brittle fracture. Likewise, for resistivity nitrogen is preferred over oxygen because it is more soluble at lower temperatures. Although interstitial impurities will increase electrical resistivity and mechanical strength, additions of even 0.1% will reduce magnetic properties drastically for SMC core materials. SMCs rely on the coating material for resistivity and particle shape and size for overall strength. Substitutional impurities (Si, V, Cu, and Sn) of up to 1% in Fe do not greatly affect magnetization, and therefore can be used to improve other properties such as electrical resistivity and mechanical strength if possible [58]. Schafter et al. presented an Fe–Si–Cu composition that allowed for improved mechanical strength and electrical resistivity without decreasing magnetic properties greatly by relying on a liquid phase formation of Cu to obtain uniform coating layers [61]. Additions of Si to NiFe powder resulted in low magnetic saturation ($M_s$) values of ~150 emu·g$^{-1}$ for $Fe_{70}Ni_{20}Si_{10}$ powder as compared to ~214 emu·g$^{-1}$ for $Fe_{80}Ni_{20}$ powder [62]. The addition of Si greatly improved electrical resistivity, but drastically decreased saturation. Iron alloys such as

NiFe and CoFe have higher magnetic permeability and higher magnetic flux density, respectively, as compared to pure Fe, and are advantageous for soft magnetic applications. Without any coating material, pure Fe sintered composites have relative permeabilities between 2900 and 4700, while the addition of Ni greatly increases this value (to 21,000 for Fe–50%Ni) [35]. However, these additions have very high material costs associated with them, often too high to justify the improved magnetic properties [35, 63].

In addition to the core powder being influential to magnetic properties, the coating material chemistry is extremely important. Nonmagnetic regions, nominally organic coatings or ceramics, drastically reduce magnetic permeability, since they act as internal demagnetizing fields as found by Wulf et al. for SMCs of more than 1 wt% organic resin [56]. The use of ferrites as coating materials can reduce the effect of nonmagnetic boundaries [43]. However, soft ferrites are quite brittle and thus do not deform, but rather shear during compaction if not properly bonded to core surfaces [64]. Operating frequencies of ferrites range from 1 kHz to well over 100 kHz with DC permeability ranging from 500 to 5,000 as compared to Si–Fe alloys (6,000 to 18,000) [65]. Additionally, dielectric coatings and dislocations in the ferrous core decrease permeability because cavities between particles reduce local magnetic saturation and dislocations hinder domain wall movement, which is the reason for stress relieving temperatures [40]. Magnetic property dependence of structural features at the interface of ferrite-coated powder material has not been studied in depth.

**Role of Microstructure**

With regards to soft magnetic properties such as permeability, coercivity, and saturation magnetization, lower amounts of interstitial sites, higher densities, and coarser grain sizes are desirable [6]. Microstructural defects such as dislocations and grain boundaries impede the motion of domain walls, thus distorting and enlarging the magnetization curve. Grain size and magnetic volume have large effects on density, magnetic saturation, coercivity, mechanical strength, and DC losses as seen for amorphous and nanocrystalline materials [36]. Composites with larger particle and grain sizes allow for improved densities, low coercivities, and low hysteresis losses because of the lack of non-magnetic inclusions and defects such as airgaps or grain boundaries. For example, non-oriented

electrical steel sheets with larger grain sizes (∼170$\mu$m) had improved core loss, magnetic induction, and permeability at 50 Hz with less magnetic field [66]. Likewise, for powder materials, grain size can be largely controlled by particle size, where Anhalt et al. presented increased densities and lower coercivities for larger particle sizes that allow for higher Fe volume fractions [67]. Magnetic domains are therefore not pinned due to smaller grain sizes and require less energy to move, thus lowering demagnetizing fields, and increasing magnetic performance.

Saturation magnetization values were found to increase from 164.7 emu·g$^{-1}$ to 254.4 emu·g$^{-1}$ for ball milled and then annealed Fe–Si–Ni powder because of the internal stress relief allowing for less regions of discontinuity within ferromagnetic regions [22]. The effect of a larger grain size is clear in increasing magnetic performance, where amorphous and nanocrystalline materials simply cannot outperform crystalline powder. For powder materials, if additional nonmagnetic regions are found between particles, the affect to magnetic saturation and coercivity will be more dominant than grain size. Particle boundaries may have more regions of air gaps and thicker inclusions leading to larger demagnetizing fields. Small particle sizes not only result in low density, but also significantly more regions of boundaries due to low surface to volume ratios. Nominally if we assume spherical particles, the surface area ($SA$) and volume ($V$) are calculated by the following:

$$SA = \pi D^2 \tag{2.1}$$

$$V = \frac{\pi D^3}{6} \tag{2.2}$$

$$\frac{SA}{V} = \frac{D}{6} \tag{2.3}$$

where $D$ is the diameter of the spherical particle. With these equations we can estimate a particle with diameter ∼300 $\mu$m to have a surface area to volume ratio = 50 following Eq. 2.3, which is much larger than a particle size of ∼30 $\mu$m of $SA/V$=5. Therefore, the larger particle sizes will allow for less particle boundaries overall and will improve density and magnetic performance. An optimal average Fe particle size is between 110–120 $\mu$m with compaction pressures ranging between 600–1100 MPa for $SiO_2$–coating [21] and phenolformaldehyde resin coating [36]. Grain size plays a

key role in reducing core loss. Shiozaki et al. discovered an optimal grain size for magnetic steel to be between 100–150 $\mu$m [66], and confirmed a direct proportionality between eddy current loss and grain size [68]. In SMCs, these grain sizes can be obtained using similar particle sizes and annealing temperatures above 600°C [69].

### 2.2.3 Core Loss

Core losses reduce a materials magnetic performance at elevated frequencies, therefore requiring more power to obtain a similar flux density than at lower frequencies. Core loss ($P_{total}$) is expressed by the following equation:

$$P_{total} = P_h + P_e + P_a \tag{2.4}$$

where $P_h$ and $P_e$ are the hysteresis and eddy current loss contributions, respectively, $P_a$ is the anomolous loss component [1]. For simplicity purposes, in determining the contributions of hysteresis and eddy current losses, $P_a$ is ignored. Core loss is an important consideration for powder parts manufacturers because it determines the correct frequency application for their product, often tested using a standard toroid sample with ASTM standard A103 [70]. Several properties play key roles in minimizing hysteresis and eddy current losses, often not optimized simultaneously.

### 2.2.4 Hysteresis Loss

Hysteresis loss is the main component of core loss at low frequencies, determined by,

$$P_h = f \oint H dB \tag{2.5}$$

where $f$ is frequency (Hz), $H$ is magnetic field strength (T), and $B$ is magnetic induction (G). This equation allows for the assumption that no eddy current losses are present at frequencies below 50 Hz, when a coating layer is electrically insulating. $P_h$ is related to the coercivity and permeability of a material; lower coercivities result in lower hysteresis losses [1]. This component can also be calculated by measuring the area of the B–H loop. A larger $H_c$ will increase the area enclosed by

the loop and effectively raise $P_h$. As previously mentioned, the microstructure of a material has a large effect on coercivity. Likewise, particle size and subsequent boundaries effect hysteresis losses. SMCs that utilize organic binders are forced to use low temperature curing, because the coating breaks down, which results in strained ferrous grains and high hysteresis losses [71]. Therefore, using large grained, high purity ferromagnetic powder and post–compaction annealing to relieve impurities and work hardened regions, pinned domain walls can be eliminated and thus hysteresis losses reduced [69]. Nonmagnetic coating regions also act as pinning sites, maybe even more so than Fe grain boundaries or dislocations, because internal demagnetizing regions are localized at the coating. For this reason, ferrimagnetic insulators are optimal coatings for SMCs to minimize domain walls being pinned at particle boundaries.

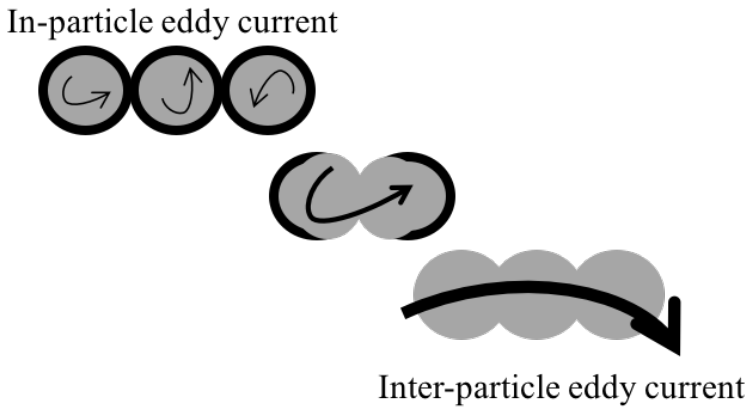


**Figure 2.3:** Diagram illustrating in-particle eddy currents as opposed to inter-particle eddy currents for SMC materials.

### 2.2.5 Eddy Current Loss

Although powder purity is fundamental for high magnetic permeability and low hysteresis losses as previously mentioned, the formation of eddy currents is in response to poor resistivity of the core powder and improper insulation between particles. The metallic core has a high resistivity when impurities are plentiful, such as alloys of two or more elements [35], especially oxygen which are not beneficial for reducing hysteresis losses. More internal defects and smaller grain sizes allow for more interruptions of electron paths and thus lower electrical conductivity, obtained by introducing strained powder and small particle sizes. The internal strain state of ferrous powder and composites

with respect to magnetic properties have been studied greatly [72, 73]; however, the effect of a coating material surrounding the core powder has not been well documented. In addition, coating–core interfacial interactions have not been experimentally researched as heavily, although computational diffusion studies are available [74].

Eddy current losses are more dominant at higher frequencies as determined by the following,

$$P_e = \frac{CB^2 f^2 d^2}{\rho} \tag{2.6}$$

where $B$ is magnetic induction (G), $d$ is the thickness of the material (m), $\rho$ is the electrical resistivity of the material ($\Omega$·m), and $C$ is a proportionality constant [1]. Significant losses are found when higher frequencies are applied, ultimately causing excessive heating of the material, due to eddy current formation. In SMCs, eddy currents are classified in two ways, flowing within single particles (microscopic eddy currents) or throughout the entire SMC cross-section (macroscopic eddy currents), seen in Figure 2.3, with the latter being related to current laminations [75]. Nonmagnetic coating layers or highly resistive materials act as barriers between microscopic eddy currents and drastically reduce this portion of the overall core loss. Macroscopic eddy currents in powder SMCs result from improper insulation of particles and need to be avoided for SMCs to be applicable at high frequencies. Inorganic, high temperature protective coatings are capable of electrically insulating ferrous powder even after compaction and heat treatment, to eliminate eddy currents and improve efficiency of devices.

## 2.3 Powder Metallurgy

### 2.3.1 Processing Steps

The processing methods to form SMCs often follow conventional powder metallurgy techniques, such as milling or mixing of metal powder potentially with alloying elements, then compacting, curing, and secondary operations, as depicted in Figure 2.4 [5]. Mixing of powder leads to uniform distribution of all materials including ferrous powder, coating particles, lubricants, and binders. Large scale mixers allow for several tons of powder, however, most research in laboratories study

powder batches below a few pounds. Ball mills, double cone mixers, shear mixers, and acoustic mixers all have the capability to be employed for SMC development. Milling of various elemental powder allows for the development of mechanically alloyed core materials, often annealed to control grain size and increase magnetic permeability [22]. Smaller grain sizes, nominally nanocrystalline materials have very high coercivity ($H_c$>1000 A·m$^{-1}$) and are less compressible as compared to large grained-ferrous alloys ($H_c$<10 A·m$^{-1}$) [76]. Therefore intense milling can only be employed if subsequent annealing takes place. Several groups have proved annealing ball milled powder greatly improves magnetic saturation; however, subsequent processing steps to coat powder with phosphates and ferrites have led to reduced magnetic permeability [7, 22, 51]. As previously mentioned, in order for ferromagnetic powder to be used, each particle must be coated with an electrically resistive material to confine eddy currents within individual particles and reduce eddy current buildup by increasing electrical resistivity. The procedure for coating powder has been a large area of research and will be discussed in the following section.

### 2.3.2 Coating Methods

Coating materials that bond well to itself and the ferrous core powder have great potential for improving density and mechanical strength of SMCs. Dry mixing methods allow for minimal lubricant or binder to be added and therefore contamination of interstitial impurities are kept to a minimum. Wet chemistry techniques for coating iron-alloy powder surfaces with protective layers often have uncontrollable phase transformations and layer thicknesses, which can lead to degraded magnetic properties. Specific methods used for coating ferromagnetic powder for SMC applications include surface oxidation [51, 77], microwave treatment [7], sol-gel method [42, 78, 79], and microemulsion method [40, 80]. As an example, the formation of undesired oxides, nominally maghemite ($Fe_2O_3$) and hercynite ($FeAl_2O_4$), were found for chemical reactions of MgO [79] and $Al_2O_3$ [81] coated Fe composites, respectively. Zhao et al. produced $NiFe_2O_4$-coated FeCo powder from centrifugation of a melt mixture [82]. As $NiFe_2O_4$ content increased the magnetic permeability decreased, most likely result of antiferromagnetic-like exchange interactions at the interfaces because of the powder being heated to the boiling temperature. Guicheteau et al. used five different aqueous acidic solutions to

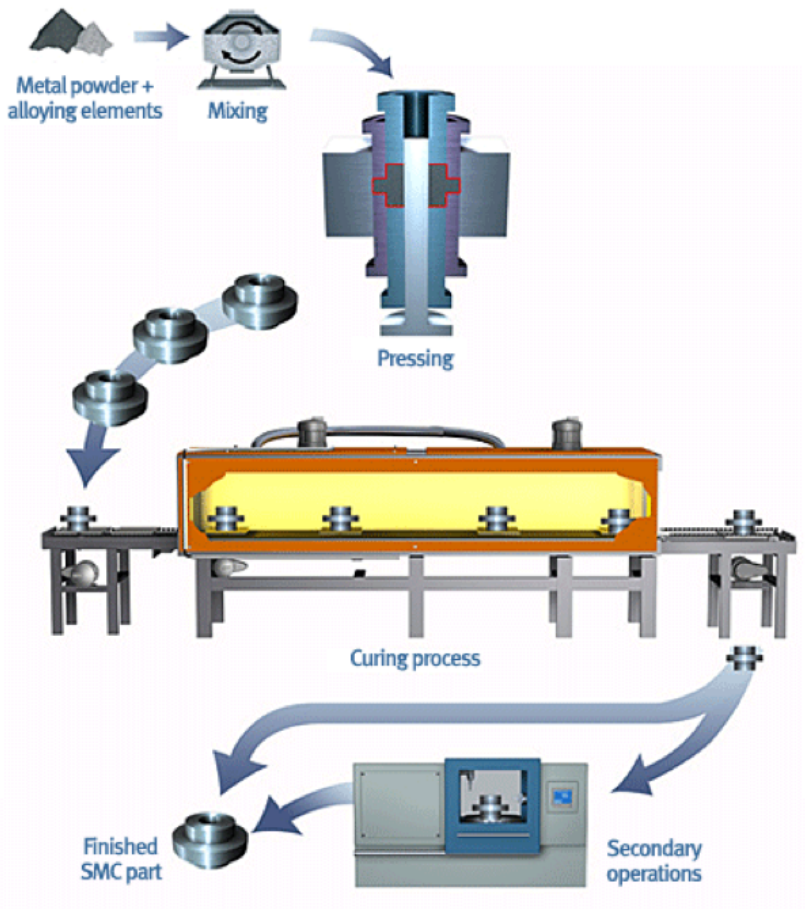


**Figure 2.4:** Procedure for manufacturing a soft magnetic composite part [5].

surface treat iron powder and produce Ni–Zn ferrite layers [83]. Studies formed a non-uniform layer of magnetite nanoparticles, which created a weak interaction between the coating and core easily broken by sonication. Much research has been focused on the production of nanoparticles to improve properties by producing a uniform coating layer with isotropic magnetic flux capabilities [84, 85]. Wu et al. found Mn–Zn ferrite coated SMCs formed FeO and MnO above 400°C using nanoparticles, and showed very low magnetic saturation values [42]. Agglomerates of nanoparticles are often an unavoidable factor without the use of chemical surfactants aiding in additional processing steps and consequently increasing time and cost. Fe–based SMC materials were produced by acidic bluing to form iron oxide coated particles, compacted and heat treated at 450°C for 1 h by Zhao et al. [43]. This low temperature did not allow for work-hardened regions to be relieved after compaction. In addition, low densities and the formation of $Fe_2O_3$ proved this method to be ineffective for high magnetic permeability applications. Most wet chemistry techniques use chemicals with high safety concerns, making them undesired coating solutions for industrial manufacturing.

Dry coating methods, based on Van der Walls interactions and static forces between large (host) powder and small (guest) particles, have also been developed that avoid long chemical processes and safety concerns. Mechanical milling conventionally used for deformation and refinement purposes as well as blending, can also be used as coating methods [86, 87]. In addition, ball milling can be used to alter the internal microstructure of powder, shown by Xu et al. for ball milled Fe–Si–Ni powder discussed previously [22]. A particles magnetic response is directly related to the purity and size and can be controlled via the preparation and processing methods [1]. In addition, adding organic fillers during milling can reduce intensity and allow for the surface composition of milled powder to be modified and the particle size and shape maintained [88]. We can similarly adopt this notion by using ferrite particles as a filler in milling processes to coat larger iron particles uniformly [53]. Although, the coating and core interface are not chemically bonded after dry coating methods are employed, subsequent compaction and annealing steps can produce a composite of coated powder, without the use of organic binders. This concept of no added organic binder is foreign to current research and provides this thesis a unique quality.

### 2.3.3 Compaction and Heat Treatment

Coated particles are densified by the application of pressure to form the desired part shape [6]. High green densities, nominally the density after pressing, but before heat treating is necessary for maximum permeability and saturation induction. Compaction follows these steps, outlined in Figure 2.5; filling the die cavity, application of initial pressure leading to rearrangement of particles, application of additional pressure leading to deformation to minimize pores and maximize mechanical interlocking, and lastly ejection from the die (not shown). The initial powder fill, dependent on the packing density is crucial for particle repacking and reduction of pores. The conventional process for developing SMCs from coated powder requires high compaction pressures (>800 MPa) to maximize density and heat treatment temperatures between 570–775°C for proper iron stress relief [6, 89]. Ideally compaction pressures are below 800 MPa, however materials that do not compress well because of very small grain sizes or hard coating materials may require higher pressures, even up to 3 GPa [22, 48, 90]. Even small amounts of cold work will increase the coercivity of a material by inducing dislocations and increasing microstrain as previously discussed [89]. The act of compaction actually rearranges particles and allows air gaps to be filled during pressing. However, it should be noted that softer materials will deform first if needed, nominally Fe in ferrite–based coating systems.

After compaction, iron–based SMC materials need to be cured to properly relieve the stress and dislocations brought on by the deformation step of compaction. The low temperature range of 570–775°C does not allow for sintering of particles to improve density and mechanical strength, often necessary for handling components during assembly and winding of motor cores, making a high green density all the more important. Curing is necessary to preserve the coating layer so that no metal–on–metal contact points are found and in-particle eddy currents can be obtained as opposed to inter-particle eddy currents, shown in Figure 2.3. A unique approach of "double press – double cure" (2P2C) developed by K.S. Narasimhan et al. is capable of achieving high densities (>7.5 $g{\cdot}cm^{-3}$) using warm (80°C) compaction between 700–830 MPa and multiple curing and compacting steps [91]. This technique initially compacts the powder, then cures at 400°C for 1 h, then represses the compacts under the same conditions, and finishes with a second curing step of 450°C to insure

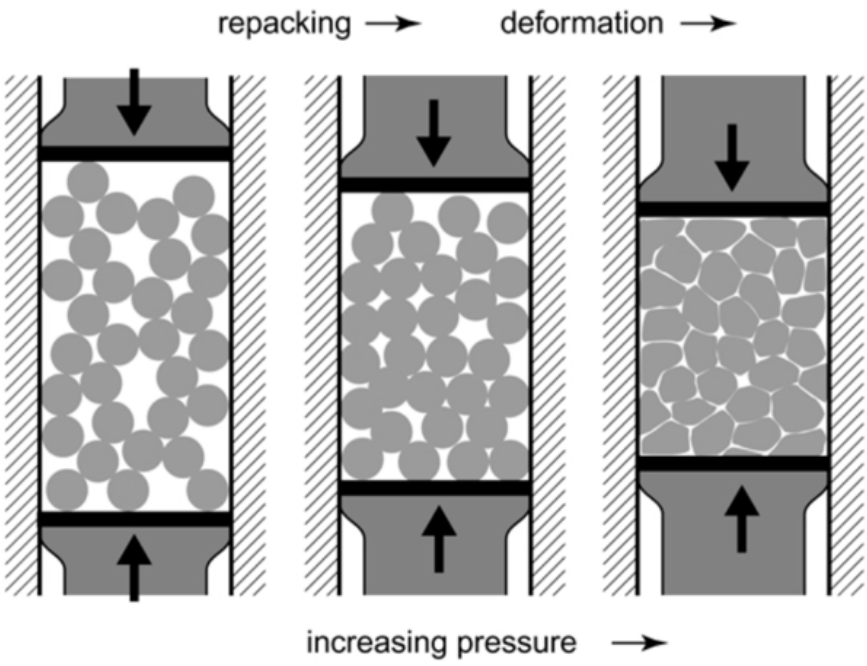


**Figure 2.5:** Schematic illustrating stages of compaction. Initial stage allows for particle repacking at low pressures. Increasing pressures allows for deformation of particles to reduce pores and create mechanical interlocks [6].

minimal porosity and maximum density, without diminishing the coating material. A long process like this may be effective in reducing core loss, but is not industry–friendly because of the expense and time associated with the extra steps. Therefore, an ideal approach to forming SMC materials will keep compaction pressures below 800 MPa, with curing temperatures as high as possible to reduce processing time.

## 2.4 Material Selection

By and large, selecting the proper material for any application is of the utmost importance. SMCs require materials with superb soft magnetic properties to be functional at the desired frequency and possess the mechanical integrity to be handled in a manufacturing facility and perform at high speeds. The soft magnetic properties of interest include high magnetic permeability (high magnetic saturation and low coercivity), which are obtained by the least amount of nonmagnetic inclusions, and low hysteresis loss. A great comparison of magnetic properties for typical electrical

machine cores is presented for various lamination alloys, an amorphous iron, and a soft magnetic composite, in which each system possesses a leg up on their competition in one way or another [92]. The performance of soft magnetic materials is largely dependent on the applied frequency, which depends on the materials electrical resistivity. Ferromagnetic materials (iron– and nickel–alloys) are applicable at low frequencies (<2 kHz) because they are strong conductors, while ferrimagnetic materials (ceramic oxides or ferrites) are more resistive and therefore are applicable at much higher frequencies (>80 MHz), but suffer in overall magnetization capabilities from the additional oxygen content [1]. Combining the two types of magnetic materials by utilizing a ferrimagnetic coating and a ferromagnetic core powder allows for applications requiring high magnetic induction and low losses. SMCs will bridge the gap between these two materials traditionally used for very different frequency ranges. Without a doubt, SMCs allow for the highest electrical resistivity using organic or inorganic coatings because of the electrical insulation between particles, ultimately diminishing eddy currents. SMCs utilizing soft ferrite coatings have the potential to allow for high electrical resistivity while creating excellent soft magnetic properties by maximizing the ferromagnetic volume.

### 2.4.1 Core Materials

Traditionally, SMCs have been comprised of ferromagnetic powder, including pure Fe, Fe–Si alloys (high electrical resistivity), Fe–Ni alloys (high magnetic permeability), and Fe–Co alloys (high magnetic flux density), seen in Table 2.3 [1, 92]. Each system has its own unique magnetic and electrical behavior, with Fe having the absolute lowest cost, often a dominating factor, with relatively high soft magnetic characteristics. Pure Fe powder is used as the core material in this thesis because of the low cost, high induction, and least amount of elements for easier microstructural analysis after processing. Likewise, several groups focus on pure Fe as a base material which allows for direct comparison of properties for different coating materials [18, 21, 39, 44]. We must note that more recently advancements in amorphous and nanocrystalline materials have shed light on their potential for SMCs. Nanocrystalline materials in regards to SMCs have single– or multi–phase polycrystalline grains that are less than 100 nm in size and are often produced using high energy ball milling for extended periods of time [62, 93, 94]. The majority of these materials are comprised of interfaces,

namely grain boundaries that allow for high electrical resistivity and low eddy current losses, but pin magnetic domains, increasing coercivity and decreasing magnetic induction. Amorphous materials also called metallic glasses having thicknesses as low as 0.025 mm and allow for very low coercivities and core losses, but result in very low densities (<6.2 g·cm$^{-3}$) and low magnetic induction levels (<1.3 T) [90]. For these reasons, amorphous materials are not ideal for SMC applications that require high magnetic performance. The cost to manufacture these amorphous ribbons is also a tremendous expense and often overshadows the low core loss.

**Table 2.3:** Comparison of permeability, flux density, and cost for iron alloy systems; the top row representing the highest values and the bottom row representing the lowest values for each respective property [1].

| **Permeability** | **Flux Density** | **Cost** |
|---|---|---|
| Ni–Fe | Co–Fe | Co–Fe |
| Si–Fe | Fe | Ni–Fe |
| Fe | Si–Fe | Ferritic Stainless |
| Co–Fe | Ferritic Stainless | Si–Fe |
| Ferritic Stainless | Ni–Fe | Fe |

Several properties rely on the overall amount of magnetic phase in the SMC. Higher volumes of magnetic material yield higher density, permeability, and saturation magnetization as to be expected. Higher amounts of electrically resistive material, either being organic or inorganic, will significantly decrease the density and soft magnetic properties, however will reduce the eddy current loss. Optimizing this tradeoff is of the utmost importance for determining the proper material and range of frequency applied. This thesis uses ferromagnetic powder instead of amorphous or nanocrystalline materials to allow for the highest magnetic permeability and induction possible.

### 2.4.2 Coating Materials

Organic and inorganic coatings are utilized separately and combined to insulate the core material so that eddy current losses can be reduced. Only when the amount of nonmagnetic insulation is minimized and ferromagnetic volume maximized, will density and magnetic permeability be at its highest. Organic polymers create an embedded matrix while inorganic materials form an encapsulation around each particle. Organic coatings are mostly thermoset polymers, such as epoxy resins, acrylic powder, polyester powder, polyurethane powder, and hybrids of these [1]. They have good

electrical resistivity, ideal for lower eddy current losses, but greatly lack in thermal stability and magnetic performance. Low saturation (<0.64 T) and low permeability (<225) were found with a 3 wt% resin addition to high purity Fe [35]. These materials allow for complete isolation of particles by way of infiltrating the ferrous powder structure and uniformly distributing insulation layers. However, all types of organic materials cannot withstand temperatures above 450°C before they break down, leaving large pores and metal–on–metal contact points increasing both hysteresis and eddy current losses. Benefits of combining both types of coating materials have shown reduced core loss and improved mechanical strength, but the magnetic performance ultimately suffers [19, 28].

Inorganic coating materials on the other hand are capable of withstanding temperatures well above the stress relieving range of Fe composites. Coating materials previously studied include phosphates (Fe, Mn, Zn), oxides (Al, Mg, Si), and soft ferrites (Fe, Ni, Mn, Zn) [19–21, 28, 40, 77, 81, 95]. Inorganic coatings allow for higher curing temperatures to minimize hysteresis losses and maximize magnetic permeability as well as maintain the isolation network between ferrous particles, for reduction of eddy current losses. For example, alumina ($Al_2O_3$) can withstand high cure temperatures (>900°C) and has a resistivity of $10^{14}$ Ω·cm, but requires high compaction pressures (>1 GPa) or additional lubricants that heighten hysteresis losses from the reduced magnetic volume [48, 78]. Phosphates are one of the more common insulating materials formed using phosphoric acid, but can only withstand temperatures up to 600°C before they degrade [28, 44, 77, 81, 95]. One study of note uses a double layer of phosphate and polyepoxy (organic) on Fe, which minimizes eddy currents and improves magnetic permeability at high applied frequencies (>100 kHz) [28]. However, an organic binder is necessary because of the brittleness of the phosphate which creates cracks and microcavities during compaction thus increasing metal–on–metal contacts. The additional protective layer, in this case polyepoxy, yields a more uniform coating and increases electrical resistivity, however, this comes at a cost to the magnetic performance. Silica is also a coating material of note, seeing much attention in recent years [19–21, 39, 40, 81]. Low core loss values of 3.5 $W \cdot kg^{-1}$ at 50 Hz and 1 T have been presented for $SiO_2$–coated Fe powder [21] and silicate glass ($SiO_2$–$Na_2O$–CaO) coated Fe powder [23]. This presented core loss value is much lower than that of commercially available

Somaloy 500 with $Fe_3P$ coating layers (6.1 $W \cdot kg^{-1}$) [57]. However, very low magnetic flux densities are presented for the silicate glass composites of 57 vol% Fe ($B_s$~1.05 T) and 82 vol% Fe ($B_s$~1.57 T) [23]. Ideal coating materials do not reduce the overall magnetic permeability or flux density of the SMC, which limits the application of all organic and some inorganic coatings.

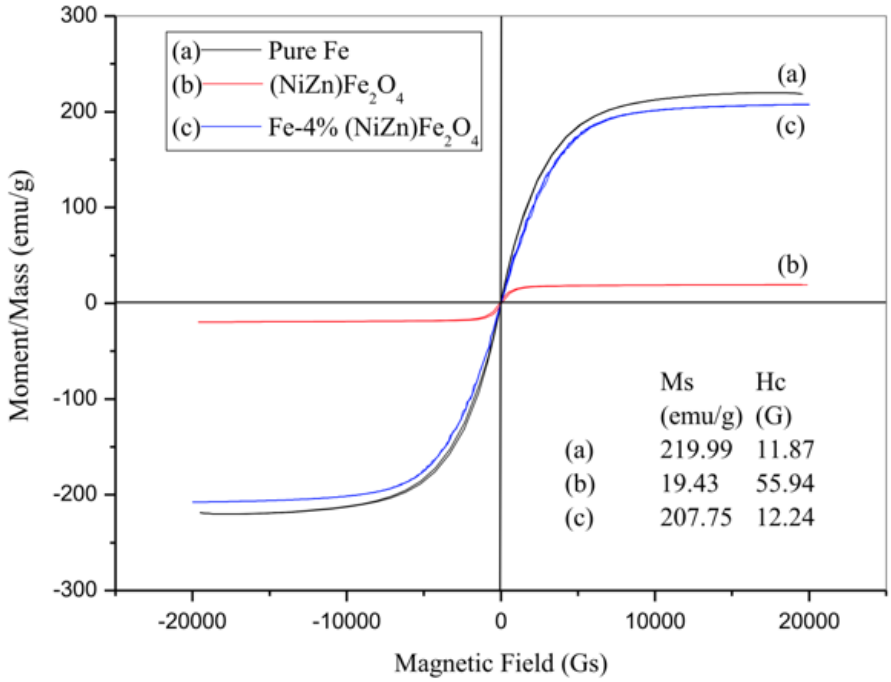


**Figure 2.6:** Magnetization curves for (a) Fe particles, (b) NiZn ferrite powder, and (c) Fe with 4 wt% NiZn ferrite powder [7].

### Soft Ferrites

Increasing electrical resistivity is key to reducing eddy current losses; however, if this drastically reduces the magnetic permeability of the system as is the case for previous organic and inorganic materials discussed, then the coatings are not practical. Soft ferrites are promising coatings materials because they can withstand high temperatures (up to 900°C), and allow for increased resistivity and improved magnetic performance [4, 7, 18, 26, 27, 42, 96]. Typical magnetic saturation and resistivity values for various ferrites along with acceptable AC frequency range applications are presented in Table 2.4. Electrical resistivity has been shown to increase from 0.2 $\mu\Omega \cdot m$ for uncoated Fe to 280 $\mu\Omega \cdot m$ for $Fe_3O_4$–coated Fe [18] and further to 686 $\mu\Omega \cdot m$ for $(NiZn)Fe_2O_4$–coated Fe [4]. Additionally, minimal reduction in magnetic saturation shown in Figure 2.6 for $(NiZn)Fe_2O_4$–coated

Fe composites with 4 wt% coating, much improved from nonmagnetic coatings [7]. Phase transitions for $Fe_3O_4$–coated Fe composites have shown detrimental effects on core losses [51]. Curing up to 600°C oxidizes $Fe_3O_4$ to FeO, which reduces the overall ferromagnetic volume, increasing coercivities (>650 A·m$^{-1}$) and lowering permeabilities (<100) [96]. $Fe_3O_4$ may not be the best solution for SMC coatings since it has a low resistivity, but allows us to study the effect of microstructure and coating particles on magnetic properties. Ferrite coatings of higher resistivity are much stronger candidates for SMCs. Higher curing temperatures (780°C) for MnZn–ferrite coated Fe–Si powder significantly reduced inter–particle eddy currents using ∼6.1 wt% coating material [27]. Higher magnetic permeability should have been obtained, but low densities (<5.6 g·cm$^{-3}$) and high porosity volumes (20%) were found. To date, magnetic permeability results for ferrite coatings have not greatly surpassed lamination steel standards and continue to demand improved scientific discoveries.

**Table 2.4:** Comparison of magnetic and electrical properties and respective frequency ranges acceptable for standard ferrite materials.

| | **Magnetic Saturation** (emu·g$^{-1}$) | **Resistivity** (Ω·cm) | **Frequency Range** |
|---|---|---|---|
| Crystalline Fe | ∼220 | $10^{-6}$ | < 400 Hz |
| $Fe_3O_4$ | ∼90 | $10^{-2}$ | < 1 kHz |
| $NiFe_2O_4$ | ∼55 | $10^{3}$ | 30–300 MHz |
| MnZn–Ferrite | <50 | $10^{2}$ | 30–300 MHz |
| NiZn–Ferrite | <42 | $10^{6}$ | 300 MHz – 3 GHz |

# Chapter 3: Techniques and Methods

## 3.1 Introduction

In this section we elaborate on the techniques and methods employed for material development and characterization of various electrical, magnetic, mechanical, physical, and structural properties. The processing methods we describe include thin film growth, powder milling and coating methods, and compaction and curing steps. We then discuss the techniques used for analyzing the different material systems. A thorough understanding of interfacial interactions between the coating material and Fe core is accomplished in this thesis. A study on thin film bilayers, which replicates the coating–core interface in an ideal state, allows for a more in-depth understanding of structural and magnetic behaviors of these materials at interfacial regions as shown in Figure 3.1.

Pure iron is the primary core material studied in this thesis because of its relatively high Curie temperature of 770°C, high melting point of 1538°C, and high magnetic saturation of ∼220 emu·g$^{-1}$ [97]. Likewise, iron is widely used in soft magnetic applications because of its good magnetic permeability and low cost compared to alloys of Co–Fe and Ni–Fe, previously shown in Table 2.3. This research concentrates on a suite of inorganic coating materials, including a ceramic oxide, alumina ($Al_2O_3$), and soft ferrites, magnetite ($Fe_3O_4$) and nickel zinc copper ferrite (NiZnCu-$Fe_2O_4$). $Al_2O_3$ is studied because of its high electrical resistivity, $Fe_3O_4$ is studied because of its high magnetic saturation, and NiZnCu–ferrite is studied because it provides a solid balance of the two. Powder composite studies use $Al_2O_3$ and $Al_2O_3$–$Fe_3O_4$ coatings as an introductory system as proof of concept (Ch. 4). Additional studies focus on $Fe_3O_4$–coated Fe to determine temperature dependence of microstructural defects on magnetic properties (Ch. 5). Local microstructure within the core powder and at the interfaces are studied to reduce internal strain and confine eddy currents within particles for core loss reduction. An optimal milling process and stress relieving temperature is then determined and used to study NiZnCu–ferrite coating materials (Ch. 6). Comparisons of all coating studies are made in Ch. 7, to determine the ideal coating material, of the three coating

types studied, for optimization of SMCs in electromagnetic devices.

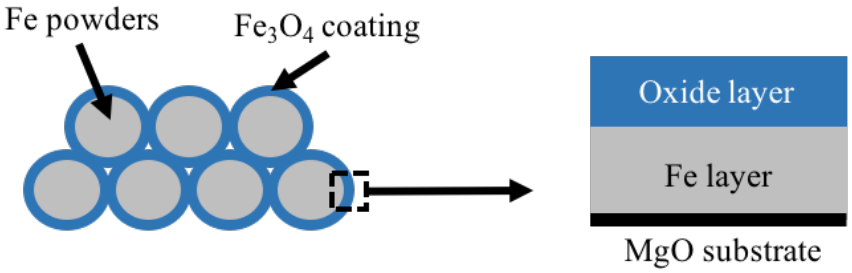


**Figure 3.1:** Schematic of coating–core interface from powder system replicated with a thin film bilayer for comparison.

## 3.2 Thin Film Studies

This thesis studies the effect of interfacial properties of $Fe_3O_4$–Fe systems from an ideal crystalline state (thin films) to highly strained state (powder composites). This is accomplished by replicating the $Fe_3O_4$ coating on Fe in thin film form, as shown in Figure 3.1, and correlating the microstructural features to magnetic properties. These $Fe_3O_4$–Fe bilayers are studied to analyze the dependence of layer thickness, microstrain, and interfacial defects on magnetic saturation and coercivity, to be correlated to bulk powder studies. In Ch. 5, we provide a complete study from ideal to strained state of the $Fe_3O_4$–Fe system, using thin films and powder materials.

### 3.2.1 Sample Preparation and Related Experimental Methods

$Fe_3O_4$–Fe single crystal thin film systems are deposited on commercial MgO (100) substrates using molecular beam epitaxy (MBE) in a high (2 x $10^{-9}$ Torr) vacuum with substrate heating (∼300°C). Details on the MBE system can be found in Ref. [98]. MgO is the primary substrate used because of the almost doubled lattice parameter of $Fe_3O_4$ (∼8.4 Å) leading to minimal lattice mismatch [99]. Thin film systems vary Fe thicknesses from 5 to 50 nm with a constant $Fe_3O_4$ layer of ∼30 nm. Deposited thin films are characterized using X-ray diffraction (XRD) and reflectometry (XRR) for composition, crystallinity, and film layer thickness. Transmission electron microscopy (TEM) is used with electron energy loss spectroscopy (EELS) to study diffusion and element rich regions of the layer interfaces. Lastly, bulk magnetic properties are measured using vibrating sample magnetometry

(VSM). These techniques are described in more detail later in this chapter.

## 3.3 Powder Studies

**Table 3.1:** Relevant properties for each coating material used in this thesis compared to Fe.

| **Material** | **Density** ($g \cdot cm^{-3}$) | **Magnetization** ($emu \cdot g^{-1}$) | **Resistivity** ($\Omega \cdot cm$) |
|---|---|---|---|
| Fe | 7.85 | 220 | $10^{-6}$ |
| $Fe_3O_4$ | 5.15 | 90 | $10^{-2}$ |
| NiZnCu-$Fe_2O_4$ | 5.25 | 50 | $10^{8}$ |
| $Al_2O_3$ | 3.95 | 0 | $10^{14}$ |

The primary ferromagnetic powder in this thesis is high purity Ancorsteel 1000C iron powder, provided by GKN–Hoeganaes Corporation in Cinnaminson, NJ. Ancorsteel 1000C is produced by atomization into irregular, homogenous particles with compressibility ratings of 7.1 $g \cdot cm^{-3}$ at 550 MPa [100] with very low oxygen and nitrogen levels, ideal for soft magnetic applications. Iron particles are initially sieved to obtain the desired distribution of particle sizes for each study. Three size classifications, coarse (250 to 420 $\mu$m), medium (105 to 250 $\mu$m), and fine (45 to 105 $\mu$m), are achieved for research described in Ch. 4 and 5, to determine particle size dependence on structural and magnetic properties. Ancorsteel 1000C as-received particle sizes are sieved to remove particles below 75 $\mu$m for Ch. 6. Although, spherical shapes are ideal for minimizing coating layers and improving packing densities, green densities will greatly suffer due to lack of mechanical interlocking during compaction [6]. For this reason, irregularly shaped powder are preferred and utilized in this thesis.

Coating materials include $Al_2O_3$, $Fe_3O_4$, and NiZnCu–$Fe_2O_4$. The relevant material properties for these coatings are presented in Table 3.1. Their effect on density and magnetization when added to Fe composites are shown in Figure 3.2, where we clearly see a decrease in density and magnetization as coating amount is added. $Fe_3O_4$ has the least detrimental effect on magnetization and similar effect on density as compared to NiZnCu–ferrite. Particle sizes used for coating material are between 1–5 $\mu$m for $Fe_3O_4$ studies and between 0.4–0.6 $\mu$m for NiZnCu–ferrite studies. $Fe_3O_4$ particles are graciously provided by GKN–Hoeganaes Corporation. Low sintering (900°C) NiZnCu–ferrite particles (LSF50) are graciously provided by Powder Processing & Technology, LLC in Valparaiso, IN.

Nanometer sized particles are not used in this thesis because the driving force for agglomerations increase as particle size decrease, therefore uniform coating layers would be significantly more difficult to produce [6].

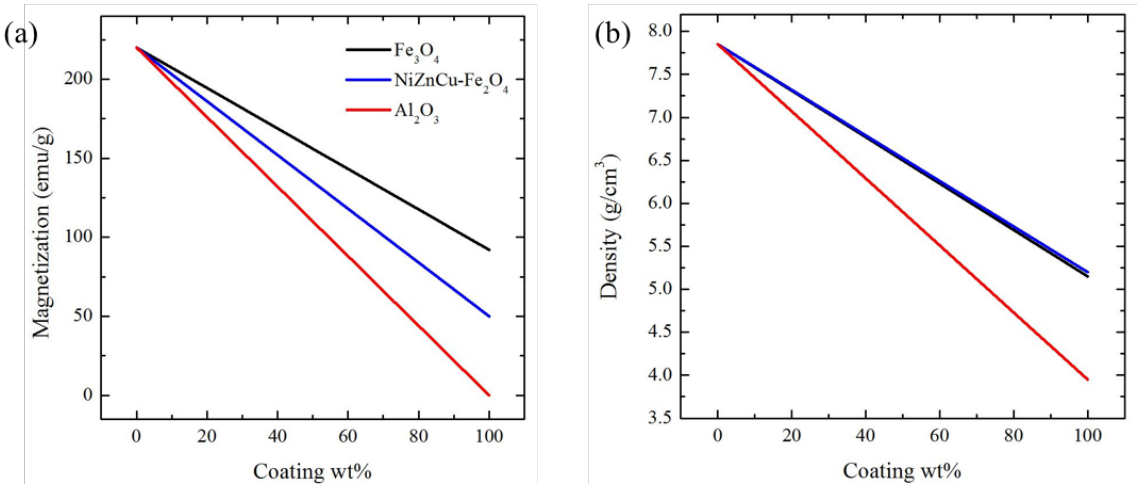


**Figure 3.2:** Theoretical calculations of saturation magnetization for each coating material based on coating percentage of Fe composites (neglecting porosity).

### 3.3.1 Coating and Mixing Processes

Iron powder is used in the as-received irregularly shaped (or sieved condition) and mechanically milled forms. A high energy SPEX8000M mixer operating at 1425 RPM at 50 Hz [101], shown in Figure 3.3a, is used at room temperature and in a laboratory environment to plastically deform and/or coat ferrous powder, without producing undesired oxide layers. The milling process is used to deform powder by creating particle–on–particle collisions, particle–on–media ball collisions, and particle–on–vial collisions. Two types of milling media are used for this study, alumina and hardened steel, with $Al_2O_3$ media balls ranging from 0.5 to 3 mm diameters and hardened steel media balls of 2 mm diameters. Likewise, alumina and hardened steel vials are used that allow powder samples of ∼50 g to be milled for each trial. Initial milling of iron powder with media balls is used to minimize porosity and reduce surface area by means of plastic deformation. Traditional coating methods utilize wet chemistry or chemical reactions as well as liquid or binder materials, while this research focusses on dry coating methods with no added liquids, to minimize processing steps, safety concerns, and nonmagnetic volume in the powder composite itself. Iron particles are pre-milled with

media balls when desired and then subsequently milled with finer sized ferrite particles to coat the surfaces and not deform further. For research studies that do not deform particles, nominally all ferrite coating studies in this thesis, no media balls are used. We instead add coating particles to the mix as compared to other researchers using organic binders, and rely on the corresponding mechanics associated with the milling process as seen in Figure 3.3b. This research is described in greater detail in studies by Sunday et al. [48, 53, 102].

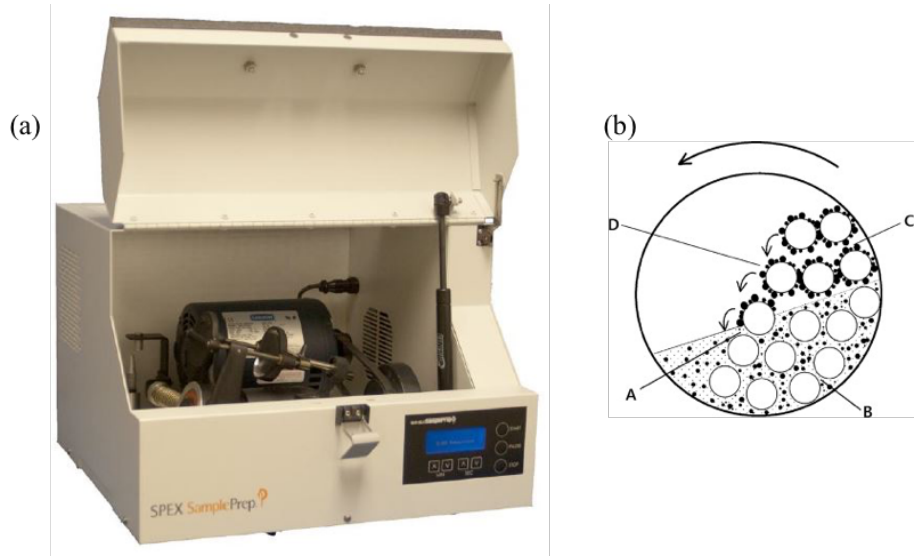


**Figure 3.3:** High energy SPEX8000M ball mill (a) with corresponding diagram illustrating the mechanics associated with the milling process (b).

An additional mixing technique is explored for NiZnCu–ferrite studies to minimize contamination from milling media, reduce processing times, and increase sample amount. A Resodyn$^{TM}$ LabRAM II acoustic mixer (Resodyn$^{TM}$ Acoustic Mixers, Inc., MT) shown in Figure 3.4 is used to coat Fe powder with sub-micron sized ferrite particles in less than 10 minutes. This method allows for more powder to be coated at one time, nominally a batch in this research is approximately 300 g, six times the amount coated in a SPEX8000M mixer (∼50 g). However, with the NiZnCu–ferrite coating particle sizes ranging from 0.4–0.6 $\mu$m, a lubricant is necessary to reduce agglomerations and increase green density. In addition, a lubricant is added in order to improve the die stripping and eliminate any chance of composites breaking during ejection. All samples with NiZnCu–ferrite coatings use 0.5% or 1.5 g of PEG 6000 lubricant, added directly to the powder blend. The temperature of the

powder is measured after acoustic mixing, to determine effectiveness in melting the lubricant and assisting with proper coating distribution.


**Figure 3.4:** Resodyn$^{TM}$ LabRAM II acoustic mixer.

### 3.3.2 Compaction and Curing Processes

The compaction step is necessary to form the desired shape unless using a molding process that requires excess amounts of organic materials, harmful to magnetic properties. It is very important to maximum packing density (arrangement of particles to increase die fill) and green density (density of part after compaction) to eliminate any pores that cannot be removed through the heat treatment process. We use uniaxial die compaction for all samples in this thesis. Fe particles coated with $Al_2O_3$ or $Al_2O_3$–$Fe_3O_4$ are compacted into cylinders of 3 mm diameter with ∼2 mm height using 3 GPa compaction pressure at Army Research Laboratory in Aberdeen, MD. The press used is a hydraulic tabletop press specifically for TEM–sized samples. Fe particles coated with $Fe_3O_4$ or NiZnCu-$Fe_2O_4$ are compacted using 800 MPa compaction pressures at GKN–Hoeganaes Corporation. Sample geometries include toroidal shapes with outer diameter (OD) ∼35 mm, inner diameter (ID) ∼25 mm, and height ∼6 mm and bars of dimensions approximately 32 mm x 13 mm x 13 mm. Toroid shapes are necessary for magnetic testing discussed later, where this specific geometry allows for symmetrical winding of copper wire and the applied current to flow through the sample. Bar geometries are

necessary for testing hardness, resistivity with a four-point probe method, and mechanical strength with a three-point transverse rupture test. The compaction step introduces stress into the material, which subsequently results in internal strain within deformed particles. As discussed previously, any amount of cold work will induce dislocations and inclusions, which in turn will drastically effect magnetic properties, such as permeability and coercivity. For this reason, a curing step is always needed after compaction of ferrous powder tailored for soft magnetic applications.

SMC materials are traditionally cured between 570–775°C in order to properly relieve stress developed during compaction. This low temperature range is not sufficient to allow for reduction of pores through particle sintering to increase density and mechanical strength, which results in the need to maximize green density after compaction. This is accomplished by maximizing packing density, the best arrangement of particles filling the die with the least amount of pores, and compaction pressure. German defines the ideal packing density to be for spherical particles with a 7:1 ratio of coarse to fine particle sizes [6]. As we previously explained, in Ch. 2, compaction pressures above 800 MPa are difficult for industry to adopt because of the space requirement and large cost associated with a larger press. This thesis utilizes a suite of curing temperatures, between 500°C to 1000°C. Samples of $Al_2O_3$–coated Fe and $Al_2O_3$–$Fe_3O_4$–coated Fe are cured in a tube furnace with an argon and hydrogen (3%) atmosphere for 1 h. Samples of $Fe_3O_4$–coated Fe and NiZnCu–$Fe_2O_4$–coated Fe are cured in a table top furnace in pure nitrogen for 1 h. Inert gas atmospheres are used for all samples in this thesis to minimize oxidation to Fe powder and undesired phase transformations of coating materials.

## 3.4 Microstructural and Chemical Composition Characterization

We analyze powder properties before and after milling/coating, compacting, and curing by employing various techniques, most notably X-ray diffractometry and various electron microscopy methods. These methods are used for determination of coating thickness, chemical composition, microstructure, and uniformity as well as core powder size, shape, internal strain, and porosity. We then test the magnetic properties using VSM and toroid AC/DC testing and correlate them to the structural properties found. In this section we describe these techniques and the processing parameters used

for this thesis.

### 3.4.1 X-ray Diffraction

In this thesis, non-destructive X-ray diffractometry is used for phase identification and microstrain analysis of powder particles during all stages of the developmental process and for determination of thin film layer thickness, crystallinity, and phase identification. This technique generates diffraction patterns from the interaction between high speed electrons and atoms of a material that emit short wavelength, high energy X-rays. When the electron beam enters the outer shells of electrons of an atom, energy is released in the form of X-rays, which is inversely proportional to the wavelength. We use this method because the short wavelength of X-rays is on the same length scale as a solids atomic bonds, Ångrströms [103]. This technique relies on Bragg Law,

$$n\lambda = 2dsin(\theta) \tag{3.1}$$

where $n$ is the order of reflection (an integer), $\lambda$ is the wavelength of incident radiation, $d$ is the lattice spacing, and $\theta$ is the angle of incidence [103], illustrated by Figure 3.5. Only when diffracted X-rays are reinforced with additional inphase X-rays, from parallel planes of atoms, will this equation be satisfied. A characteristic line spectra or diffraction pattern can then be generated corresponding to the different orientations of each present element within a material. Since polycrystalline samples contain all possible lattice plane orientations, the diffraction pattern can be analyzed for phase identification and microstrain measurements. When a material is stressed elastically and the strain is uniform over a large region, a shift in the diffraction pattern along the x-axis will be present, corresponding to new lattice spacings as shown from Figure 3.6a to 3.6b. On the contrary, if a material is deformed plastically, and instead of large variations in lattice spacing, small differences within individual grains are present, diffraction peaks will broaden, not shift. This equivalent broadening of peaks is then used to calculate nonuniform microstrain. Essentially, cold working a metal will result in an observed peak broadening, as long as the lattice spacing does not change.

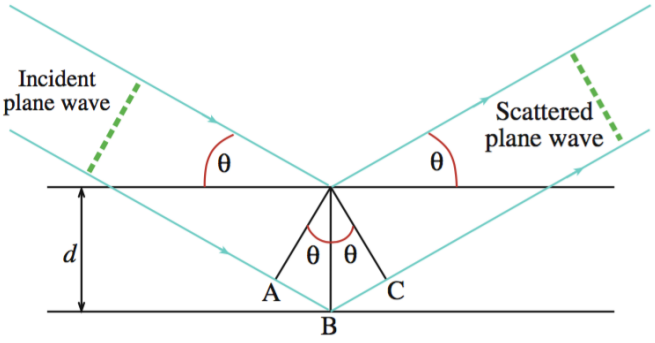


**Figure 3.5:** Illustration of diffraction concept for an incident plane wave on a specimen with parallel planes of atoms and AB + BC are equal to the path difference between reflected waves [8].

We analyze $Al_2O_3$–coated Fe particles after various milling conditions are applied, $Fe_3O_4$–coated Fe particles after milling, and compacting then curing, and thin film bilayers of $Fe_3O_4$–Fe on MgO. For powder particles and composites, XRD is used to identify phase and microstrain [89, 104]. For thin films, XRD is used to determine phase identification and lattice mismatch, while XRR (x-ray reflectometry) is used for layer thickness measurements analyzed using GENX software [105]. As XRD uses refracted X-rays, XRR uses reflected X-rays generated when the incident beam is angled less than 5° from the specimens surface. In thin film heterostructures, these reflected beams interact with each layer and are entirely dependent on thickness. GENX software measures layer thicknesses from an XRR pattern when sample geometry and scattering length densities of each layer are known.

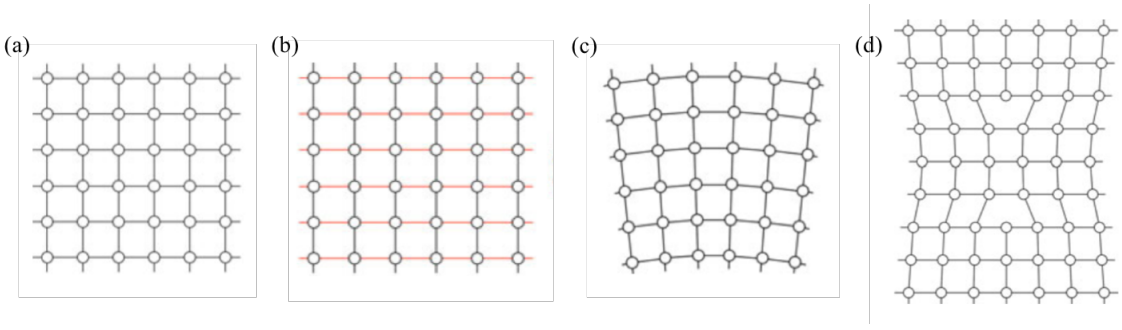


**Figure 3.6:** Effect of strain on cubic crystal structure, for (a) unstrained state, (b) elastically strained (11%) state, (c) "bent" crystal, and (d) plastically strained state showing two opposing edge dislocations [9].

The experimental measurements are carried out using a Rigaku SmartLab diffractometer with

Cu-K$\alpha$ ($\lambda$=1.54 Å) with Parallel Beam (PB) optics for thin films and Bragg-Brentano (BB) optics for powder and composite samples. In addition, a graphite crystal monochromator is used to rotate the crystal 90° to change the surface from curved to flat for improved signal–to–background ratios of XRD scans of coated powder with large particle sizes and rough surfaces. Phase identification for all samples are verified with Jade software analysis using standards JCPDS Card No: 06-0696 (Fe), JCPDS Card No: 019-0629 ($Fe_3O_4$), JCPDS Card No: 06-0615 (FeO), and JCPDS Card No: 46-1212 ($Al_2O_3$). The corresponding X-ray generator parameters and scan conditions for each sample type are presented in Table 3.2.

**Table 3.2:** Testing specifications for each sample XRR or XRD measurements.

| | **Thin Films** | **Thin Films** | **Powder** | **Composites** |
|---|---|---|---|---|
| | **XRR** | **XRD** | | |
| Optics Alignment | PB | PB | BB | BB |
| Tube Voltage (kV) | 40 | 40 | 40 | 40 |
| Tube Current (mA) | 44 | 44 | 30 | 30 |
| Scan Range (°) | 0.400 – 4.000 | 20 – 80 | 5 – 120 | 5 – 120 |
| Step Size (°) | 0.01 | 0.02 | 0.02 | 0.02 |
| Speed (°/min) | 0.1 | 1 | 7.5 | 7.5 |

### 3.4.2 Scanning Electron Microscopy

Scanning electron microscopy (SEM) is utilized for analyzing particle shape and size before and after milling, microstructure of core powder and coating layers after compaction and heat treatment, and chemical composition of core powder and coatings. This method uses a beam of electrons focused onto a specimen, and rastered along a given region to capture a high magnification image. As the beam of electrons interacts with the sample, both X-ray and electron signals are emitted, as illustrated in Figure 3.7. We use the emission of secondary electrons (SE) from conduction or valence bands for topographical information, since the low energies (<50 eV) are nearest to the surface and can escape. Those electrons with energies emitted greater than 50 eV, but less than the incident beam voltage are termed backscattered electrons (BSE). Typical SE and BSE images of the same sample (different regions) are shown in Figure 3.8. Since the depth of BSE is greater than SE, image resolution may suffer; however, BSE are sensitive to the atomic number of specimen allowing for different brightness corresponding to different elements [106]. The acceleration voltage of the

electron beam ranges from 0.5–30 keV, allowing for various penetration depths depending on the atomic number of the material. Higher atomic masses have smaller penetration depths using the same accelerating voltage, due to more BSE generation. Experimental results are obtained using an FEI XL30 microscope with Schottky Field Emission Gun equipped with EDAX energy dispersive x-rays (EDX) microanalysis and TSL electron backscatter diffraction (EBSD) analysis. Typical instrument settings for four image types collected are shown in Table 3.3.

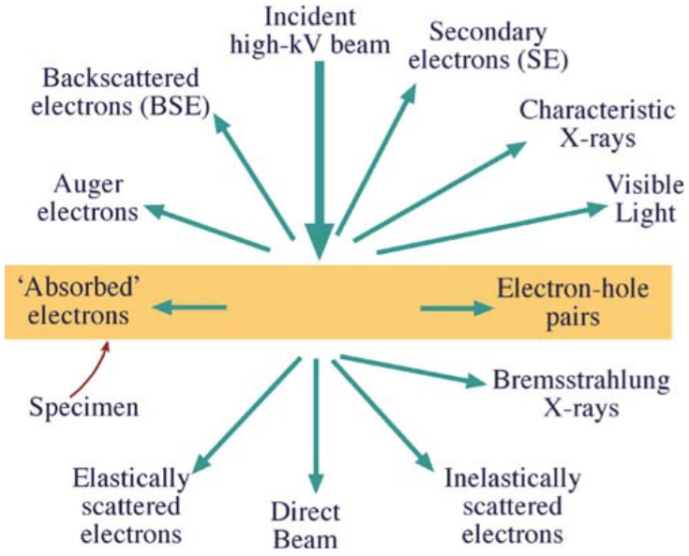


**Figure 3.7:** Various types of signals generated from an electron beam interacting with a thin specimen [8].

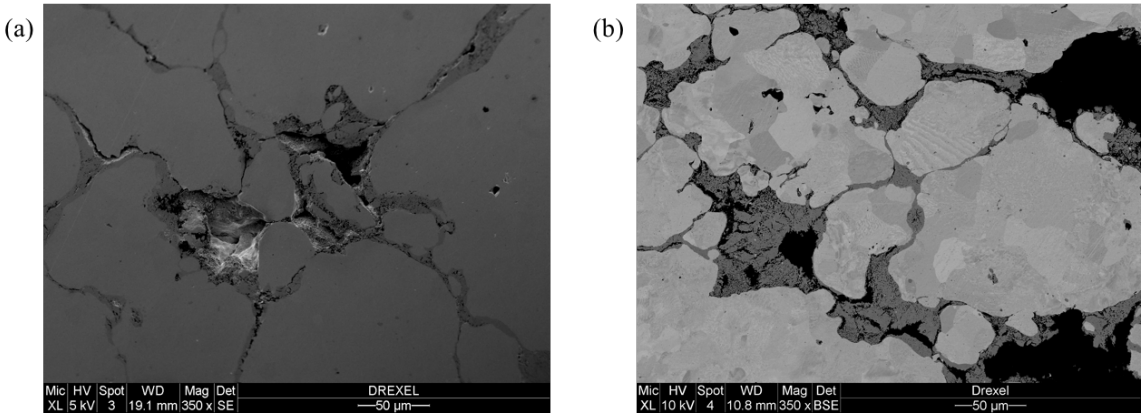


**Figure 3.8:** SEM images using (a) secondary electrons (SE) and (b) backscattered electrons (BSE) of the same sample for $Fe_3O_4$–coated Fe composites.

**Table 3.3:** Various SEM parameters for different image types.

| | SE | BSE | EDS | EBSD |
|---|---|---|---|---|
| Acceleration voltage (kV) | 5 | 10 | 15 | 20 |
| Working distance (mm) | 12 | 12 | 12 | 18–20 |
| Spot size | 3 | 4 or 5 | 4 or 5 | 4 or 5 |

### Energy Dispersive X-ray Spectroscopy

In this thesis, we use EDS (energy dispersive spectroscopy) to characterize a materials chemical composition related to specific regions in a sample. As described previously, BSE images display compositional contrast from the various elements in a specimen. EDS allows for the determination of those particular atomic number elements using the emission of characteristic X-rays shown in Figure 3.7. A typical EDS spectra is shown in Figure 3.9, where the x-axis is the energy level of the generated X-rays with the y-axis being the intensity of the number of X-rays received by the detector [107]. This elemental spectra permits semi-quantitative sample stoichiometry to be calculated, extremely useful for our coating material after processing. Corresponding distribution maps using BSE can be processed to illustrate individual elemental contributions for specific regions within the scan area, exemplified in Figure 3.10. The scan area is shown outlined with the black box in Figure 3.10a, with elemental distribution maps of Fe, O, Al, and C in Figure 3.10b. This technique allows for determination of the exact location of individual elements for powder composite samples.

### Electron Backscatter Diffraction

Electron backscatter diffraction (EBSD) is used for qualitative microstructural evaluation of the core Fe powder in composite samples. Our system is equipped with EDAX–TSL OIM (orientation imaging microscopy) software for data collection and analysis. This method allows for determination of grain size, crystallographic orientation, texture analysis, and local misorientation between points [9]. By scanning an electron beam across a polycrystalline specimen tilted at 70° from the incident beam, low energy loss BSE are channeled as a result from the crystal lattice [107]. The electrons that travel along specific planes will generate Kikuchi bands of widths dependent on Bragg

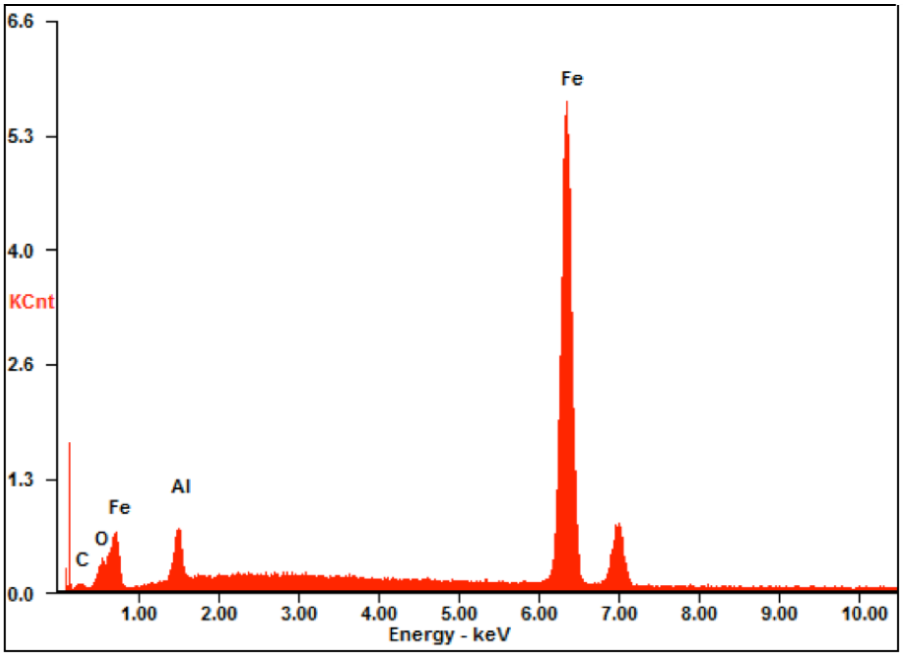


**Figure 3.9:** EDS spectra for powder composite sample shown in Figure 3.10 of $Al_2O_3$–$Fe_3O_4$–coated Fe sample.

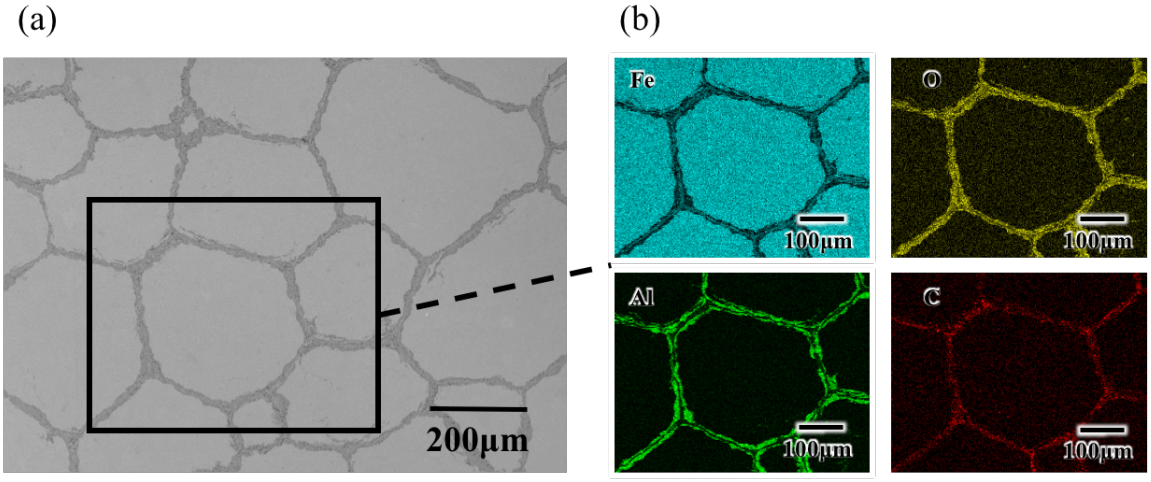


**Figure 3.10:** SEM image (a) of $Al_2O_3$–$Fe_3O_4$–coated Fe sample with corresponding EDS maps (b) of Fe, O, Al, and C.

Law and the distance to the phosphor screen. The Kikuchi lines relate to the crystallographic planes and are indexed to produce EBSD orientation maps (Fig. 3.11). Several analysis methods are used to determine grain size, boundary angles, misorientation, and texture. For example, Figure 3.11a show an inverse pole figure (IPF) map, following color code plot (Fig. 3.11c) with plotted stereographic projections (Fig. 3.11d) illustrating texture analysis. This texture analysis is made possible from the stereographic projections plot by illustrating each crystallographic direction corresponding to a specific crystal symmetry. Lastly, we can illustrate misorientation between each point in a grain by averaging the orientation in the entire grain using grain orientation spread (GOS) maps, discussed further in Ch. 5. This analysis tool allows us to identify misorientations within individual grains, essentially mapping grain boundaries below 15°. Therefore we highlight GOS maps to represent subgrain density, where dislocation density is the marker of stress remaining in the grain.

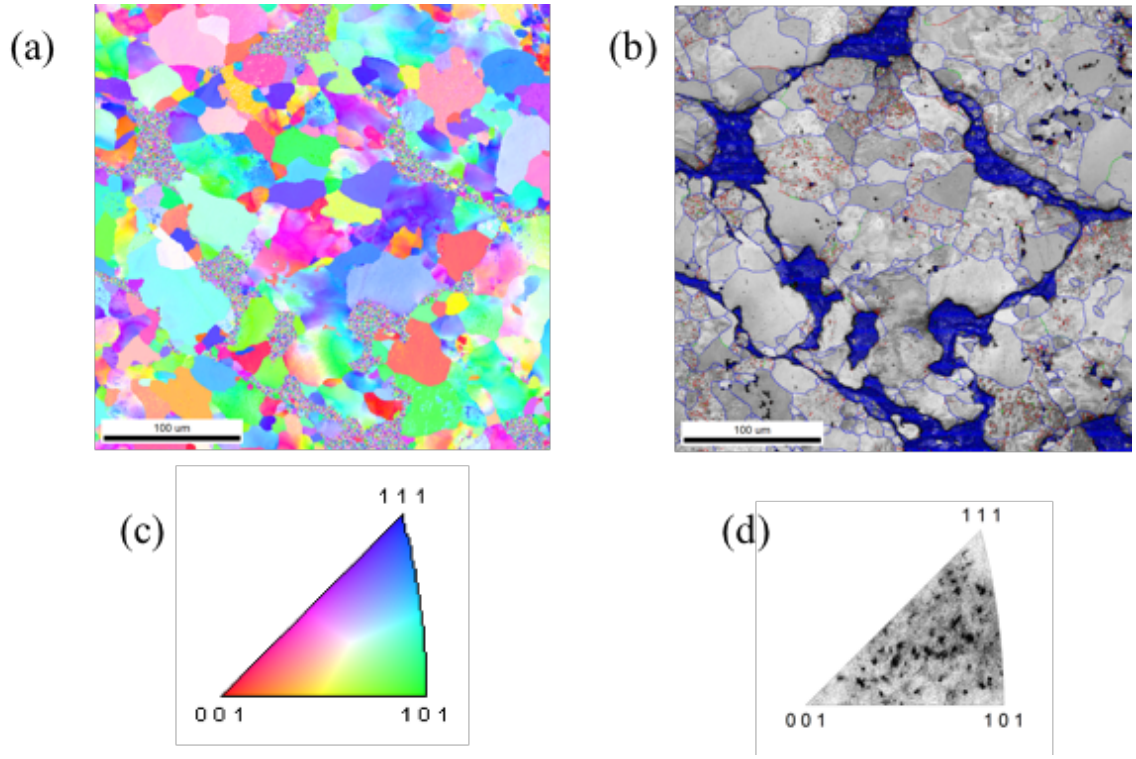


**Figure 3.11:** EBSD patterns showing (a) inverse pole figure, (b) analyzed image quality (IQ) map in grayscale and rotation angles in color, (c) IPF color code plot with (d) stereographic projections.

### 3.4.3 Transmission Electron Microscopy

High-resolution transmission electron microscopy (TEM) is used to analyze thin film cross sections and coating–core powder interfaces for crystallinity, diffusion, and elemental composition. As compared to SEM, TEM uses an even higher energy electron beam (200 keV) to transmit electrons through a thin specimen (<100 nm), illustrated in Figure 3.7. This technique allows for imaging of the crystal structure at the atomic level. A typical TEM image of an amorphous FeCoNbBCu film on a crystalline substrate is shown in Figure 3.12a–b. Similarly, using elastically scattered electrons a selected area diffraction (SAD) spot pattern, shown in Figure 3.12c for a crystalline structure and Figure 3.12d for an amorphous structure, can be produced and indexed for phase identification. Chemical composition of samples is determined using electron energy loss spectroscopy (EELS) based on inelastically scattered electrons, with the amount of energy lost pertaining to the atomic number. Subsequent elemental maps can be generated similar to SEM/EDS, but at a smaller length scale. Lastly, orientation mapping using Nanomegas ASTAR$^{TM}$ determines texture and crystallinity by combining a number of diffraction spot patterns. Crystallographic phases and orientations can be measured and mapped with respect to various regions in the sample.

This thesis uses a 200 keV JEOL JEM2100 quipped with $LaB_6$ electron gun with a double tilt specimen holder. Thin film samples are prepared using traditional cross-section polishing methods and a Fischione low angle ion mill system. Powder composite TEM samples are prepared using a dual beam Focused Ion Beam (FIB) SEM with omniprobe in-situ micromanipulator. Elemental analysis at the coating and core interface is performed using EELS to determine oxygen–rich and iron–rich regions of $Fe_3O_4$–Fe thin films and powder composites [8]. In addition, TEM orientation analysis and phase mapping is performed on thin film samples to determine crystallinity and diffusivity at layer boundaries. TEM is a suitable technique for both material systems studied in this thesis for determination of atomistic characterization of composition and microstructure.

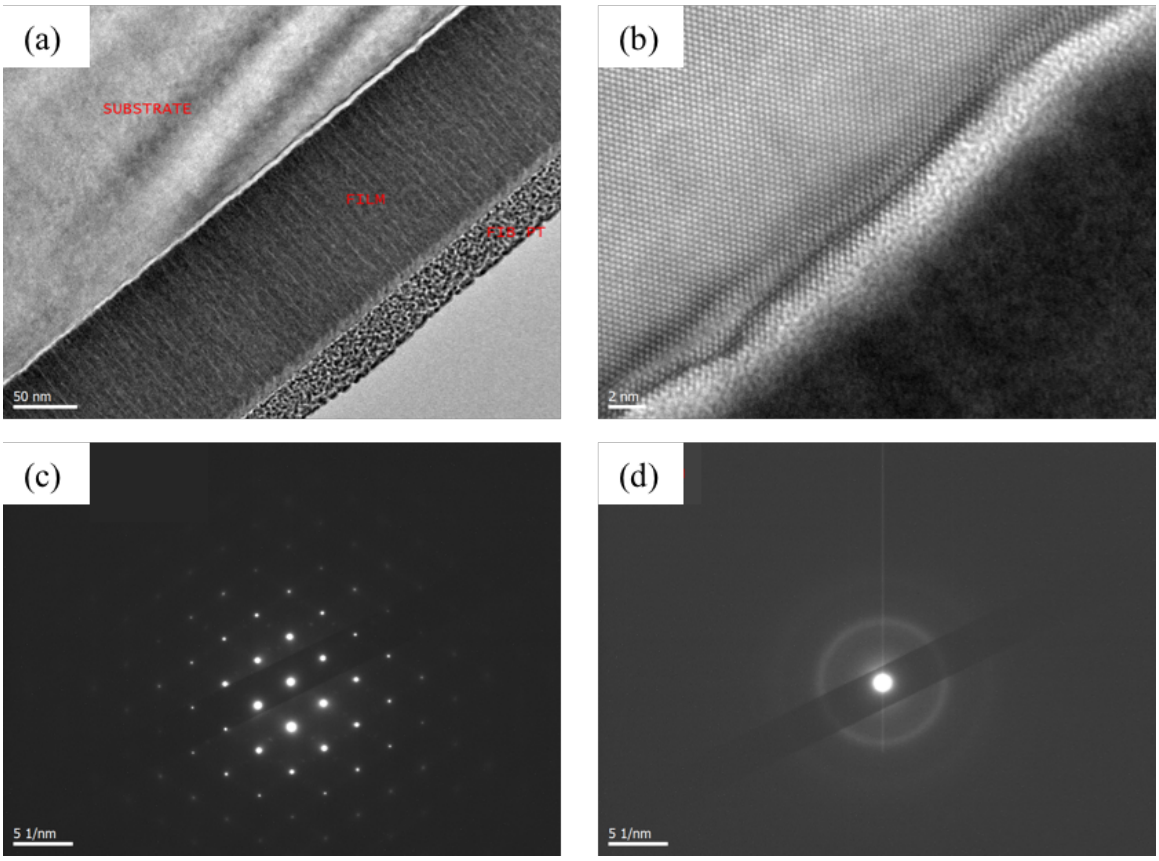


**Figure 3.12:** TEM images (a) of FeCoNbBCu film, crystalline substrate, and FIB deposited Pt, (b) zoomed in view of film and substrate interface, and corresponding diffraction patterns of (c) crystalline substrate and (d) amorphous film [10].

## 3.5 Magnetic Testing and Analysis

The correlation between microstructure and magnetic behavior is necessary to fully understand these material systems and how we can improve their processing conditions. This thesis utilizes vibrating sample magnetometry (VSM) for thin film heterostructures and small powder compacts and toroid shaped samples for testing for DC and AC magnetic properties. These techniques each possess unique characterization tools to allow for well rounded magnetic analysis.

### 3.5.1 Vibrating Sample Magnetometry

VSM is a highly sensitive technique that is based on measuring magnetic flux change from a sample vibrating at 10–100 Hz [108]. An applied magnetic field is varied to induce an electromotive force (emf) in the specimen and a reference magnet measures the response associated with this difference.

Using a reference magnet vibrating at the same frequency allows for very small magnetic moments ($10^{-8}$ A·m$^2$) to be measured [108]. VSM probes the entire sample and plots a corresponding hysteresis loop. Magnetization ($M$), measured in emu·g$^{-1}$ or emu·cm$^{-3}$ depending on sample type, is plotted versus the applied field ($H$). For thin film measurements, B–H loops are manipulated to remove the signal from the diamagnetic substrate, to correctly determine $M_s$. In addition, to obtain the most accurate magnetic saturation ($M_s$) value for each sample, a plot of the inverse magnetic field (1/Oe) versus the magnetic moment per mass (emu·g$^{-1}$) is used. The saturation magnetization is calculated by determining the y-intercept of a portion of the curve closest to a slope of zero, near the largest magnetic moment values.

This thesis uses a Physical Property Measurement System (PPMS) with Quantum Design VSM attachment operating at 40 Hz with $<10^{-6}$ emu sensitivity and temperature range of 2–350 K. A magnetic field up to 16 T is possible, but a maximum of 5 T is used for this thesis. Thin films and powder composites are placed on double–sided nonconductive tape on a fused quartz paddle of diameter 4 mm, which drastically limits the sample size allowed in the PPMS for measuring. Powder particles are placed in a plastic sample holder then in a brass half tube of similar diameter, once again limiting sample amount to ∼80 mg.

### 3.5.2 Direct Current and Alternating Current Toroid Measurements

To supplement VSM results with bulk powder magnetic testing is vital for this thesis. Thin film systems study magnetic responses in an ideal (crystalline) state while bulk powder toroid geometries study a highly strained state. Magnetic characterization of toroid transformers (Fig. 2.1) is based on an electromagnetic equation known as Faradays's Law,

$$\varepsilon = -\frac{d\phi}{dt} \tag{3.2}$$

where $\varepsilon$ is electromotive force (emf) and d$\phi$/dt is the rate of change of magnetic flux in the core [59]. To be applicable for transformers we tune this equation to include the following,

$$\nu = N\frac{d(BA)}{dt} \tag{3.3}$$

where $\nu$ is the induced voltage, $B$ is flux density, $A$ is cross-sectional area, and $N$ is the number of turns in the windings. We can determine for an ideal transformer where the power in equals the power out that the voltage ratio of primary to secondary windings will equal the ratio of turns. Knowing the applied current in the primary windings, we can measure the induced current in the secondary windings to calculate magnetic flux. Direct current (DC) measurements with no cycling of the field is used to measure permeability, remnant induction, and coercivity. When an alternating current (AC) is applied from 50–5000 Hz for this thesis, measurements include core loss, remnant induction, and coercivity. For AC testing, the process of generating a hysteresis loop is by cycling the current back and forth rapidly, following a sinusoidal wave function. For example, a toroid tested at 1000 Hz has the current cycled 1000 time a second. SMC materials have an associated core loss pertaining to material properties of AC measurements. Hysteresis and eddy current loss components of core loss are calculated to correlate microstructure of powder composites to magnetic properties. Toroid shaped samples are tested at a magnetic induction level of 1 T under DC conditions following ASTM standard A773 [109] and under AC conditions by varying frequencies from 50 Hz to 5000 Hz following ASTM standard A927 [110].

## 3.6 Additional Methods

Several additional methods are used to characterize powder after coating and mechanical and electrical properties after heat treatment. Powder properties of importance include apparent density, flow rate, shape, and size. Properties pertaining to powder geometry are found using optical metallography at GKN–Hoeganaes Corporation. These qualitative methods are crucial in determining the coated powder's ability to compress and allow for the highest green density. More quantitative measurements of powder include apparent density and flow rate, both found using a Hall flowmeter comprised of a funnel with 60° walls and 2.5 mm opening at the bottom. An apparent density of a powder is found by measuring the mass of a powder that fills a known volume using a specified

funnel, following ASTM standard B212 [111]. This measurement represents a powders ability to fill a die without agitation. A higher apparent density correlates to a better packing density and therefore a better green density because of less pores. A comparable analysis method is flow rate, following ASTM standard B213 [112], where a known mass (50 g) is poured using the same flowmeter funnel into a cup. For this test, the time the powder takes from start to finish is used to calculate the flow rate. A higher flow rate correlates to more interparticle friction and collisions between particles causing longer times to exit the funnel. After coated particles are compacted and cured, density measurements are performed. Averages of three measurements for each dimension and mass are taken to calculate density of bar and toroid samples. Density measurements are especially important for magnetic characterization and overall comparison of processing conditions.

### 3.6.1 Mechanical Testing

Bar shaped samples are used to obtain hardness values of cured powder compacts using Rockwell HRA scale on a Wilson Hardness Tester with a diamond tip. The tip initially places a minor load on the specimen, which is set as the zero position, then a designated major load is applied. The depth of penetration is measured and a hardness value provided. A softer material will allow more penetration and output a lower hardness value. Bar samples are also tested for transverse rupture strength (TRS) following ASTM standard B312 [113], as shown in Figure 3.13a. Since SMC materials are not sintered, the ASTM standard test method for green strength of compacted specimens is tailored for this thesis. A three point bend test is used to apply a load to the center of the bar specimen. The force at which the sample breaks is used to calculate the strength of the material following,

$$S = \frac{3PL}{2t^2w} \tag{3.4}$$

where $S$ is the strength (MPa), $P$ is the force needed to rupture (N), $L$, $t$, and $w$ are the length, thickness, and width of the specimen (mm), respectively. This thesis uses a Tinius Olsen H50KT instrument for TRS measurements.

Nanoindentation is also used for determining mechanical properties such as elastic modulus and hardness on a much smaller scale. The principle of nanoindentation is similar to that of the hardness tester using Rockwell HRA, however, at the submicron–level. This technique measures the depth of penetration of the indenter tip for a defined load. Although nanoindentation creates indents on the surface of a material, it can be considered a non-destructive characterization method because the defects produced are negligible. The nanohardness is then calculated by the load reached divided by the residual indentation area, measured using a light microscope, or by extracting data from the load–displacement curve. If a higher load is required to reach the same distance as a sample using a lower load, the hardness value will be correspondingly higher. For determination of elastic modulus, the slope of the load–displacement curve is used assuming a Poisson's ratio of 0.3. This thesis uses an MTS Nanoindenter XP with displacement resolution of <0.02 nm and a Berkovich pyramid diamond indenter tip at an imposed maximum depth of 200 nm.

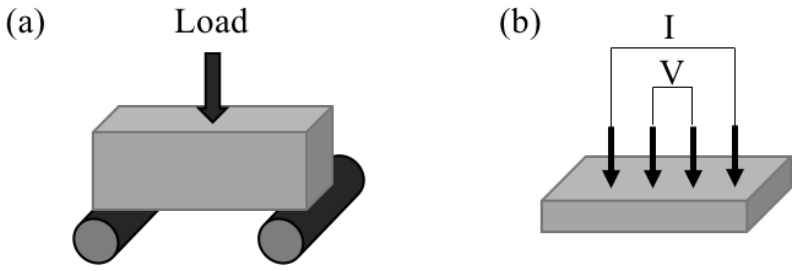


**Figure 3.13:** Schematic of (a) transverse rupture strength setup and (b) four–point probe method setup for electrical resistivity.

### 3.6.2 Electrical Resistivity Testing

A standard four–point probe setup using a Keithley current source and digital multimeter combination is used to measure electrical resistivity of polished bar samples. This technique relies on the instrumentation setup shown in Figure 3.13b, where the outer probes generate a current flow and the inner probes measure the voltage drop. The measured voltage correlates to the resistance of the material. Since there is error with sample polishing by hand, electrical resistivity is not presented, but rather a trend in resistance is illustrated in Ch. 6. A more in–depth approach to determining electrical resistivity is beyond the scope of this thesis.

# Chapter 4: Alumina Coatings

## 4.1 Introduction

Inorganic, high temperature protective coatings are capable of electrically insulating iron powder even after compaction and heat treatment, to eliminate eddy currents and improve efficiency of devices. Alumina ($Al_2O_3$), with its high melting point (2050°C) is a strong candidate for high temperature coatings that confine eddy currents within individual iron particles after compaction and curing steps. The highly stoichiometric structure and large band gap of $\alpha$–$Al_2O_3$ make electronic conduction extremely difficult, which is essential for reducing eddy currents in iron–based composites [114]. In this chapter, we discuss two alumina-based coating studies and the effect of milling time and media ball size on coating structure and magnetic properties. Here we use alumina media balls during mechanical milling to coat iron powder surfaces in the absence of additional coating material. We show, through a combination of structural and chemical analyses along with magnetic and mechanical testing, that "self–coated" powder possesses uniform alumina coatings capable of minimally effecting magnetic saturation and mechanical strength.

Several wet chemistry and dry coating techniques have been developed for coating iron-alloy powder surfaces with protective layers of alumina; however, uncontrollable phase transformations often led to degraded magnetic properties. For example, the formation of maghemite ($Fe_2O_3$) during the thermal decomposition of boehmite ($\gamma$-AlOOH), a precursor to alumina, led to decreased volumes of iron, which thus decreased the magnetic permeability [46, 81]. Alumina–coated iron nanocomposites were also synthesized by wet chemistry; however, the magnetization suffered due to the formation of $FeAl_2O_4$ at reducing temperatures below 800°C [38]. Both studies had extensive processing steps and led to undesired oxidation of the Fe core, which reduced magnetization. Dry coating methods, based on Van der Walls interactions between large (host) Fe powder and small (guest) $Al_2O_3$ particles, have also been developed. Jay et al. used a mechanofusion process to coat Fe powder ($d_{ave}$= 150 $\mu$m) with alumina particles ($d_{ave}$= 9 $\mu$m), then subsequently oxidize and

heat treat the powder to study oxidation kinetics [115]. Due to cracks in the $Al_2O_3$ coating from the processing methods, iron oxide layers formed on Fe surfaces during the oxidation process, which would thus decrease magnetization due to reduced iron content. An additional form of dry coating, is mechanical milling (by high energy ball milling), conventionally used for deformation and refinement purposes, but can also be used for an unique and simple coating method [86–88]. The mechanical forces introduced between the media material and iron powder during milling allow for powder to be internally stressed and externally coated. This allows for improved mechanical strength, while maintaining particle size [116]; but decreases the magnetic permeability by hindering domain wall motion [47]. Therefore, stress-relief temperatures are necessary to improve magnetic properties, but consequently hinder mechanical properties. These temperatures can be reached by using high temperature coatings such as alumina.

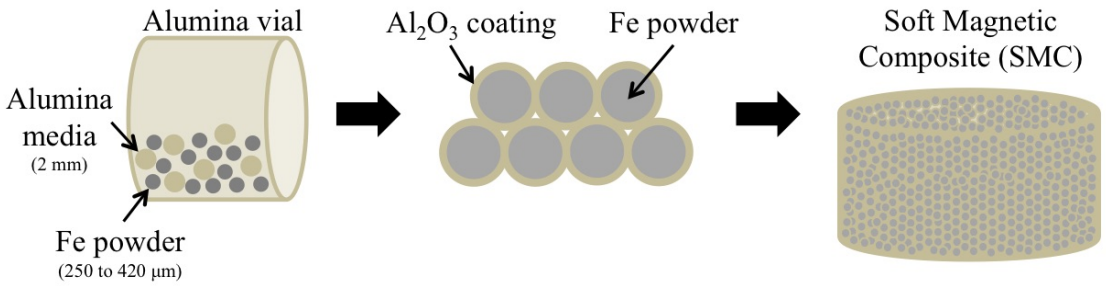


**Figure 4.1:** Procedure for producing alumina coated iron powder via mechanical milling.

## 4.2 Methods and Procedures

We investigate the effect of two types of inorganic coatings on iron powder using X-ray diffraction (XRD), scanning electron microscopy (SEM) with energy dispersive X-ray spectroscopy (EDS), vibrating sample magnetometry (VSM), and nanoindentation. We utilize dry coating methods based on Van der Waals interactions between host (Fe) particles and guest (coating) material and static forces [117]. These forces allow for large powder to be completely coated with smaller particles based on the kinetic energy and amount of contact points that occur. We employ traditional milling techniques to develop a non–traditional coating method for sufficiently insulating metallic powder. Ancorsteel 1000C iron powder sieved to coarse particle sizes of 250 to 420 $\mu$m are ball milled in an

alumina ceramic vial, with one of four alumina media ball sizes (0.5 mm, 1 mm, 2 mm, and 3 mm) to obtain $Al_2O_3$ coating or 2mm hardened steel media balls to obtain $Al_2O_3$–$Fe_3O_4$ dual coatings, with no additional material added. Trials vary from 2 to 24 h with ball–to–powder weight ratios (BPRs) of 2:3. After media balls are removed, $Al_2O_3$–coated Fe particles are either pressed as–coated or coated further with $Fe_3O_4$ particles of 1 to 5 $\mu$m particle sizes with no media balls for 1 h. The later addition is used to produce a dual coating of $Al_2O_3$ then $Fe_3O_4$. The procedure for $Al_2O_3$–coated Fe powder is depicted in Figure 4.1, while the procedure for $Al_2O_3$–$Fe_3O_4$ dual–coated Fe powder is depicted in Figure 4.2. All powder is uniaxially compacted with 3 GPa pressure into 3mm diameter and 2mm height cylinders. Compacts are cured for 1 h at 500°C, 700°C, or 900°C in an argon and hydrogen (3%) atmosphere.

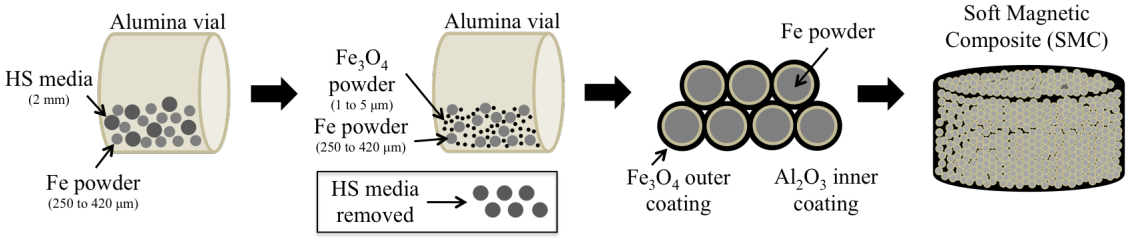


**Figure 4.2:** Procedure for producing alumina coated iron powder via mechanical milling.

The phase identification and structural analysis of alumina-coated or dual–coated powder are determined by XRD with Cu–K$\alpha$ radiation ($\lambda$=1.541 Å). Twelve hour $\theta$–$2\theta$ scans from 5° to 120° with a step size of 0.02° and speed of 7.5 deg·min$^{-1}$ are necessary for proper identification of elemental phases and microstrain caused by peak broadening effects. Williamson–Hall plots are used to analyze the crystallite size and microstrain of milled powder [104] along with the Voigt function method [118] to determine crystallite size (Lorentzian fit) and microstrain (Gaussian fit) on milled powder for a single line analysis [119]. Powder shapes and sizes as well as surface morphologies are examined before compacts are produced using SEM. Cross–sectioned powder compacts are analyzed for elemental analysis using EDS. The presence of aluminum, iron, oxygen, and carbon allow for the determination of coating layer composition and thicknesses of mono $Al_2O_3$ and dual $Al_2O_3$–$Fe_3O_4$ coatings. Saturation magnetization is measured using VSM from ±2 T at room temperature (300K). Mechanical properties such as elastic modulus and hardness are investigated by nanoindentation at

200 nm depth, where measurements are taken within iron regions of the powder compacts. Alumina–coated iron powder is analyzed for magnetic, mechanical, and structural property dependence of milling time and media ball sizes [48]. Dual $Al_2O_3$–$Fe_3O_4$–coated Fe composites are analyzed for magnetic saturation and compared to $Al_2O_3$–coated Fe composites [102].

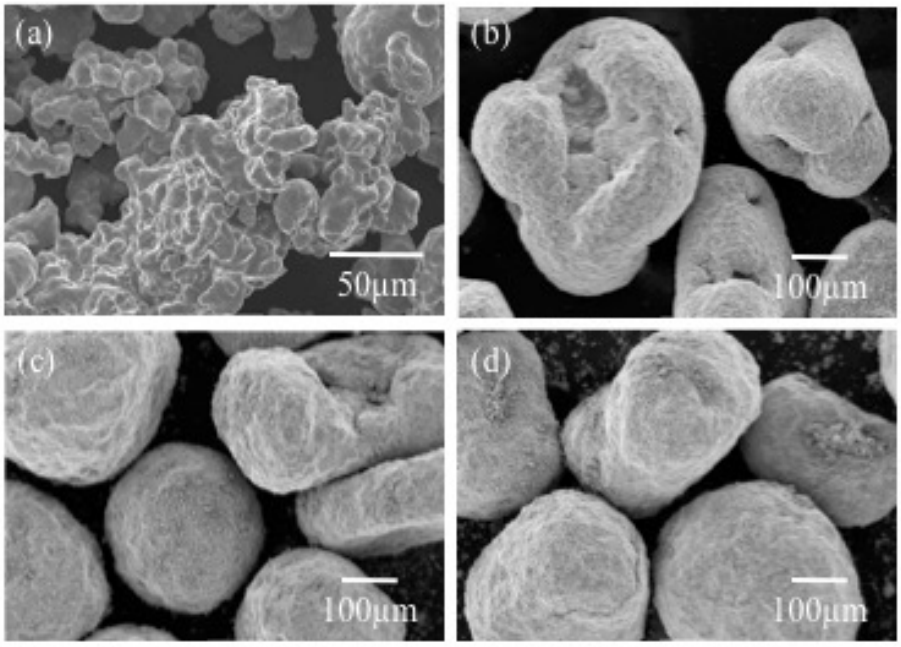


**Figure 4.3:** Iron powder milled with 2 mm media balls for (a) 0 h, (b) 2 h, (c) 8 h, and (d) 24 h in alumina vial.

## 4.3 Results

### 4.3.1 $Al_2O_3$-coated Fe Powder Composites

***Effect of Milling Time***

Iron powder ball milled at room temperature with 2 mm $Al_2O_3$ media balls in an alumina vial at various milling times are shown in Figure 4.3. A clear transition of particle shape from irregular for as-received powder to comparatively spherical for powder milled for 24 h is seen. Extended milling times result in reduced particle surface areas creating rounded edges and spherical morphologies. Ball milled powder are coated directly from the alumina media and media balls, with no additional powder added. A "self–coated" surface is characterized by a textured morphology and submicron sized particles as seen in Figure 4.4, for powder milled for 24 h. Powder milled for long periods of

time (> 12 h) exhibit an excessive amount of agglomerations of finer sized particles in outermost regions, which is an indication of coated surfaces.

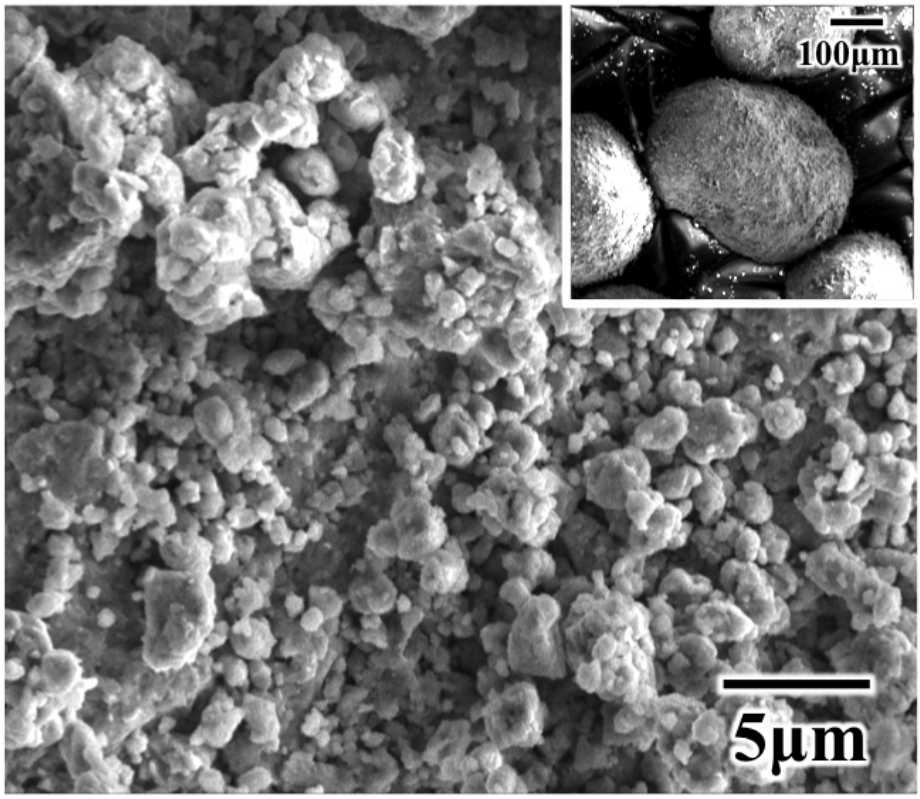


**Figure 4.4:** Iron powder milled for 24 h with 2 mm $Al_2O_3$ media balls in an alumina vial. Inset image shows lower magnification of zoomed in surface.

X-ray diffraction patterns confirm increased microstrain and alumina content on iron powder for increasing milling time from 2 to 24 h (Figure 4.5). Initial, unmilled iron powder displays minimal peak broadening and no trace of alumina content as expected. As milling time increases, Fe peak broadening increases and peak intensity decreases as evident of reduced crystallite size and increased microstrain. $Al_2O_3$ peaks emerge for powder milled for 4 h or longer.

Less deformed powder allow for improved mechanical interlocking and higher densities (7.3–7.4 g·cm$^{-3}$), compared to more deformed powder (∼6.8 g·cm$^{-3}$) using 3 mm balls or times greater than 16 h. Nanoindentation is performed on polished powder compacts to measure elastic modulus and hardness of iron after being milled, compacted, and cured. Figure 4.6 illustrates as milling time increases to 16 h, the hardness of Fe increases slightly, indication of more stressed regions,

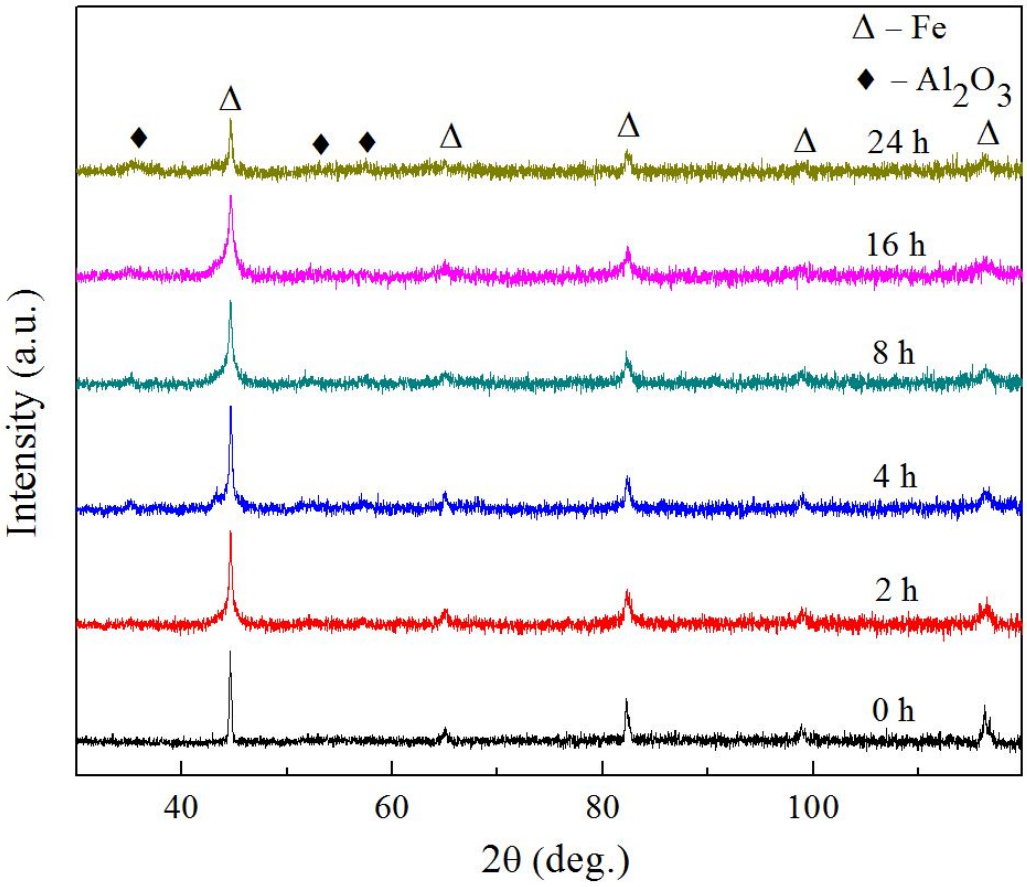


**Figure 4.5:** X-ray diffraction patterns of Fe–$Al_2O_3$ powder milled with 2 mm media balls for various amounts of time.

and decreases at 24 h. Higher curing temperatures, nominally 900 °C compared to 500 °C lead to decreased hardness. Elastic modulus remains relatively constant throughout the experiments.

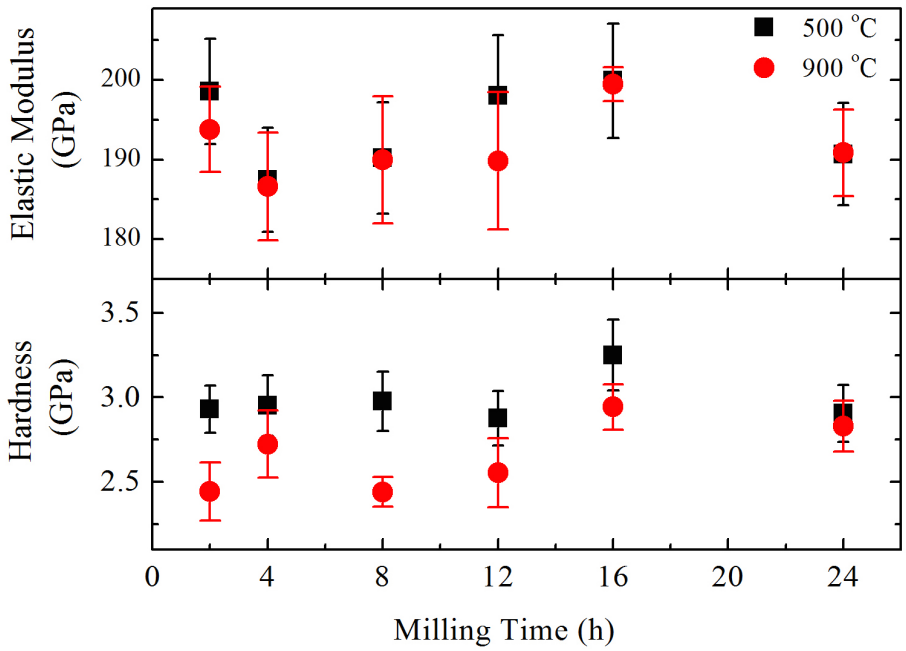


**Figure 4.6:** Nanoindentation results for hardness and elastic modulus for powder milled with 2 mm media balls for various amounts of time.

Cross-sectional SEM images of powder compacts reveal a highly dense, alumina coating on iron powder. Powder milled for 24 h, compacted, then cured at 500 °C, are seen in Figure 4.7, in which light grey regions represent Fe particles, while dark areas bordering iron particles portray $Al_2O_3$ coating as confirmed by XRD. The inset image of Figure 4.7 represents the highlighted region depicting a Fe–$Al_2O_3$–Fe junction. Finer, sub-micron sized particles of alumina are found between iron powder with a layer thickness of roughly 10 $\mu$m. We estimate milling for 24 h produces about 20 vol% coating material shown in red for Figure 4.8a, while milling for 4 h produces ~7 vol% coating shown in red for Figure 4.8b. This analysis is performed using ImageJ assuming there are no pores, since the pores are located between coating particles, making it difficult to depict with a low magnification image.

Complimentary elemental mapping from a magnified region in Figure 4.7 reveals aluminum and oxygen elements uniformly distributed on iron powder surfaces (Figure 4.9a). The oxygen content

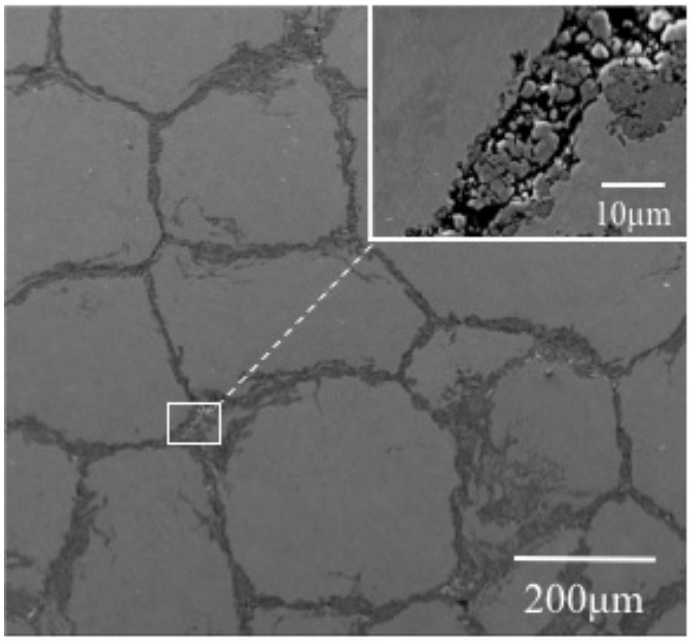


**Figure 4.7:** SEM image of polished powder compact from powder milled for 24 h with 2 mm $Al_2O_3$ media balls, compacted, and cured at 500 °C. Inset shows zoomed in view of boxed area of SEM image.

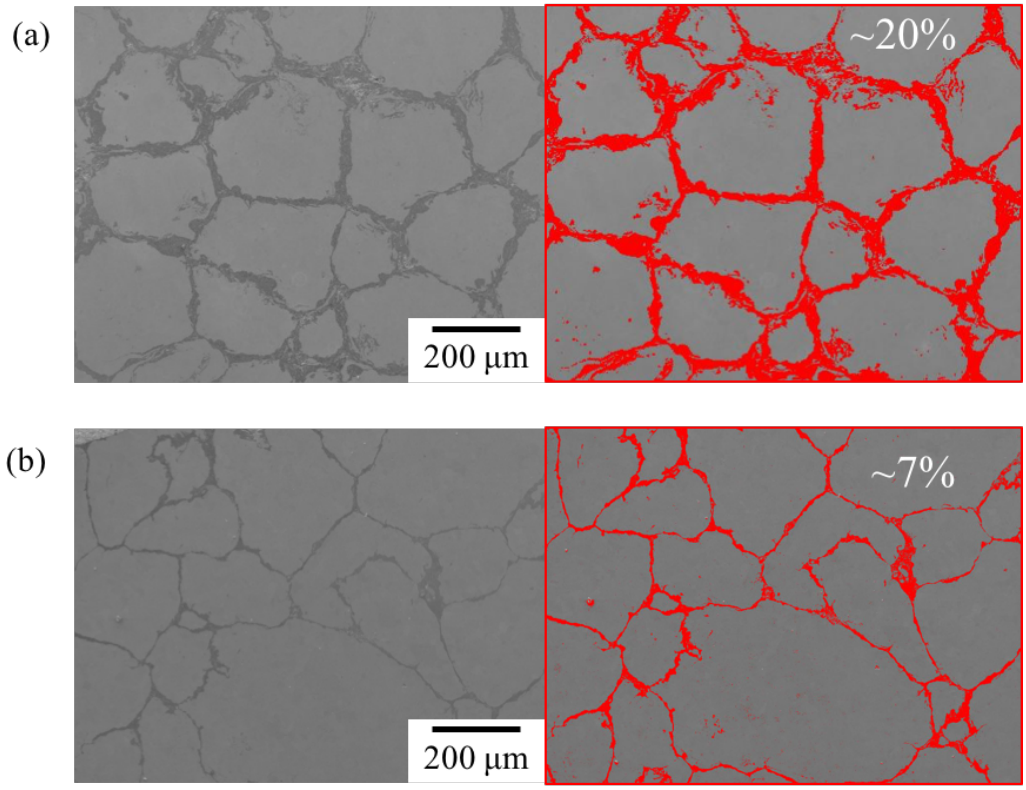


**Figure 4.8:** Image analysis for coating volume percentage for (a) 24 h and (b) 4 h of milling time for $Al_2O_3$–coated Fe composites.

found within the iron powder regions is most reasonably due to exposure to air after mounting and polishing. EDS images exhibit clear isolation of iron particles with oxygen and aluminum, which reduce metal–on–metal contact points. Similar results are found for powder milled for shorter periods of time and higher curing temperatures up to 900 °C. Alumina coating thickness determined by cross–sectional analysis range from 1 to 20 $\mu$m, depending on processing parameters. Therefore, alumina coating of iron powder is effective by means of mechanical milling.

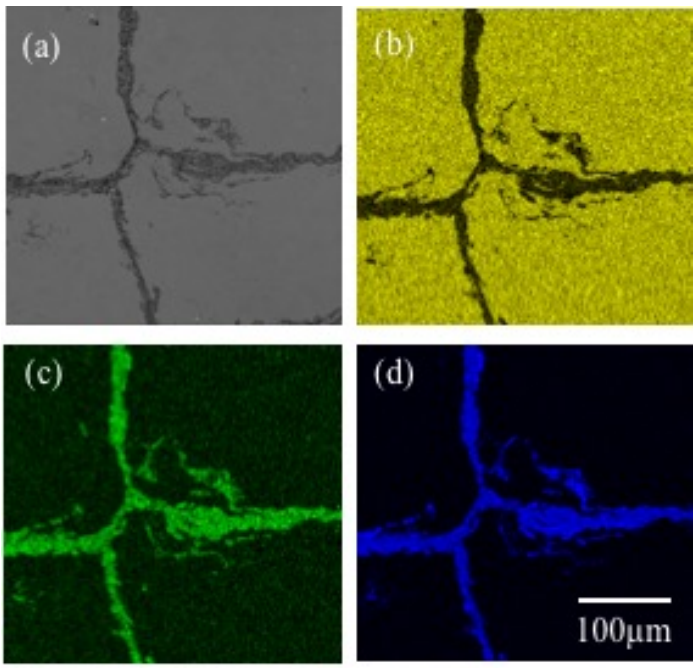


**Figure 4.9:** SEM images and EDS maps of a compact from powder milled for 24 h with 2 mm $Al_2O_3$ media balls, compacted, and cured at 500 °C.

Magnetization saturation and coercivity are evaluated using VSM measurements of cured powder compacts. Figure 4.10 shows hysteresis loops of powder compacts milled for 2, 4, and 24 h, representing soft magnetic properties and low coercivities for all samples. For as-compacted powder composites, magnetization decreases with increasing mill time. Powder compacts cured at 500 °C have higher saturation magnetization than compacts cured at 900 °C. All samples have relatively low coercivites below 15 Oe, shown in inset of Figure 4.10. Figure 4.11 indicates that magnetization decreased with increased mill time. Powder milled for 2 h possess the highest magnetization, comparable to that of pure iron ($\sim$220 emu·g$^{-1}$).

Powder has less deformation and maintains rough morphologies when milled for shorter periods

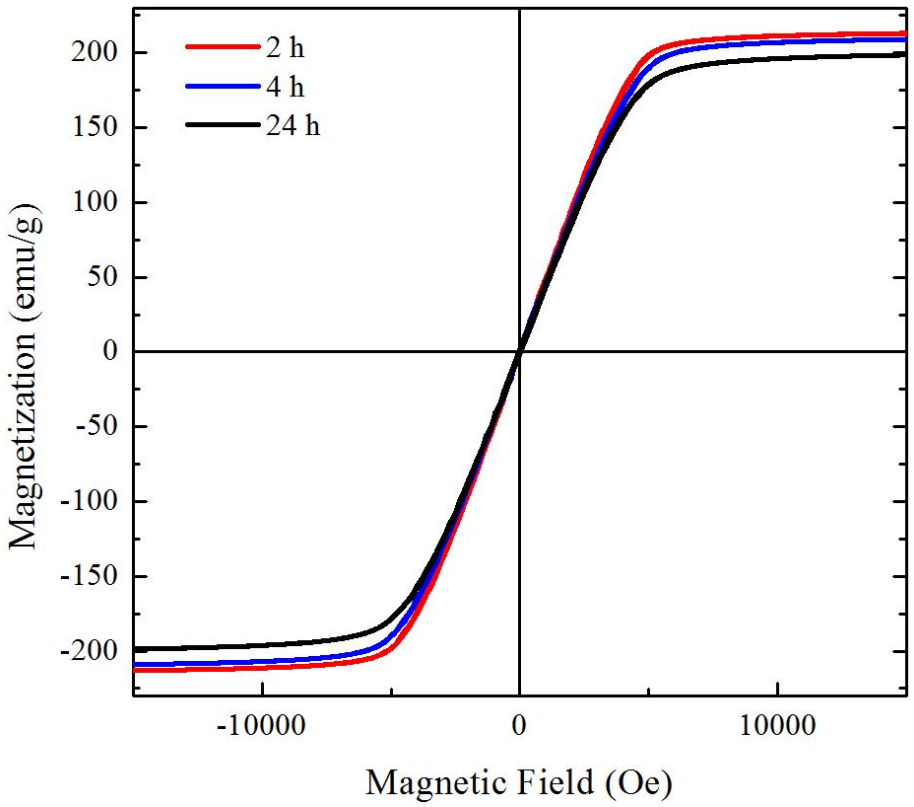


**Figure 4.10:** Hysteresis loops for alumina–coated iron powder milled for 2 h (red), 4 h (blue), and 24 h (black), then compacted and cured at 900 °C.

of time, nominally 2 to 4 h, due to less interactions with the medium, directly related to the small BPRs and media ball sizes. High energy mixers are predominately used for the reduction of particle sizes, often from mm down to nm. High ball–to–powder ratios (BPRs) (8:1 or higher) and large media balls (6–12 mm) reduce particle sizes via plastic deformation and fracturing processes. Liu et al. [86] reduced iron powder by high-energy milling of particle sizes from 25 to 2 $\mu$m after 200 h of milling using BPRs of 10:1 with stainless steel balls of 10 mm and 6 mm. Our methods of utilizing low BPRs of 2:3 and small media balls (2 mm) allow for numerous contact sites leading to minimal size reduction due to reduced kinetic energy and collision velocities [120], however, irregularly shaped particles are still deformed and often fracture to form spherical-like shapes when milled for 12 to 24 h.

Fe particle sizes are maintained in order to improve magnetic properties, due to more ferromagnetic content increasing magnetic saturation and less defects resulting in pinning sites for domain

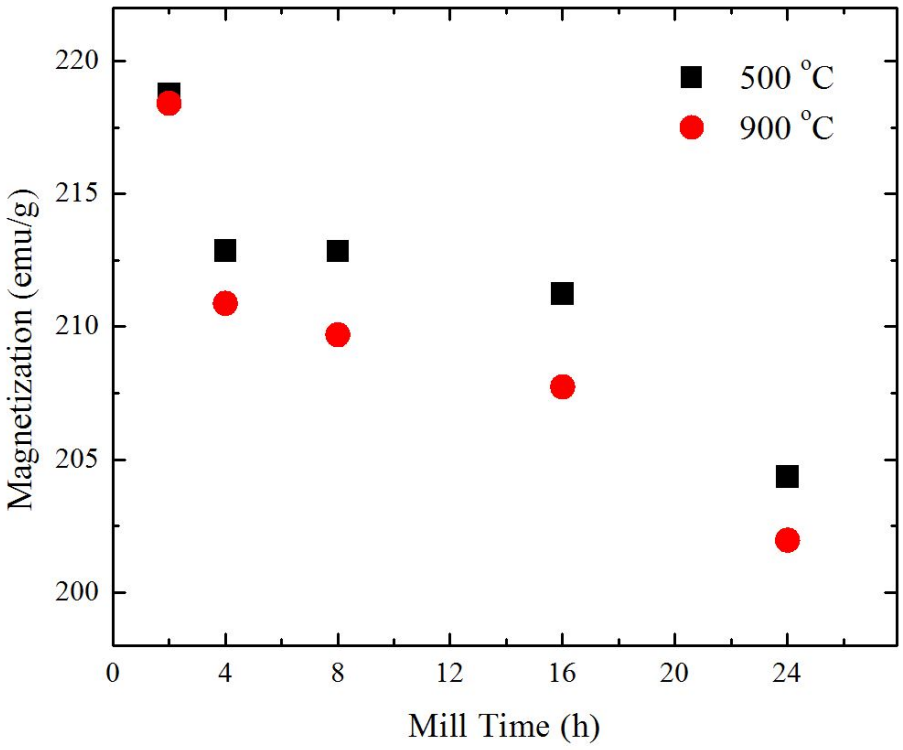


**Figure 4.11:** Magnetization results ($M_s$) using VSM as a function of mill time (h) for alumina–coated iron powder compacts cured for 1 h at the specified temperature.

walls hindering the magnetization process [67]. Larger particle sizes allow higher densities as found by Taghvaei et al. [46] for iron powder of $d_{ave}$=150 $\mu$m compacted at 1 GPa with 0.7 wt% phenolic resin. High uniaxial compaction pressures (>2 GPa) allow for high green densities and minimal amounts of internal pores, thus improving mechanical strength and magnetization. As work hardening intensifies due to longer mill times, spherical-like shapes and $Al_2O_3$ coated surfaces are observed, nominally between 12 to 24 h of mill time. XRD peak broadening indicates increased defect densities, most notably dislocations [121], and decreased crystallite sizes as milling time increases. The largest amount of defects are present for powder milled for 24 h, determined from microstrain and crystallite size calculations based on the Williamson-Hall technique [104]. Results confirm iron powder ball milled using BPRs of 10:1, in which powder milled for the longest amount of time (20 h) have the largest dislocation densities and smallest particle sizes [121].

Higher defect densities and more alumina content lead to a decrease in the magnetization due

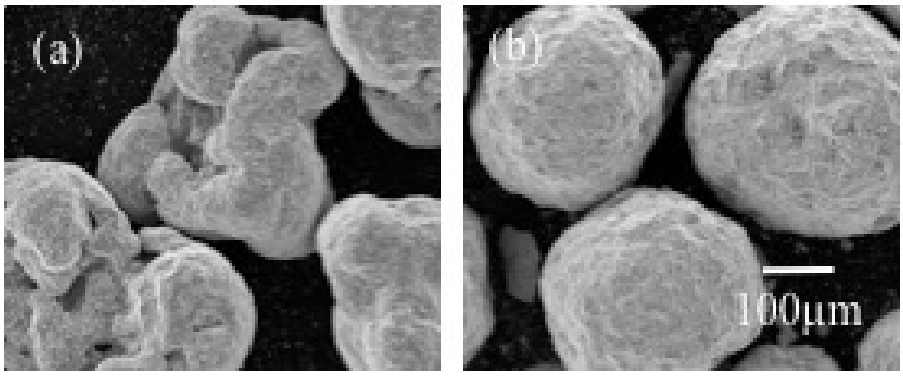


**Figure 4.12:** Iron powder milled for 4 h with (a) 1 mm and (b) 3 mm media in alumina vial.

to the hinderance of domain wall movement. Powder milled for 24 h are thus thought to have the highest defect density and the thickest coating layers for this study due to the low $M_s$. Magnetic saturation for our studies are higher than Fe–$Al_2O_3$ nanocomposites studied by Liu et al. [38]. Fe nanoparticles ($d_{ave}$=35 nm) coated with $Al_2O_3$ (20%) exhibit low magnetic saturation (∼175 emu·g$^{-1}$), much lower than our "self–coated" powder compacts. Thicker $Al_2O_3$ coatings increase the overall resistivity, therefore potentially lowering eddy current losses. However, more $Al_2O_3$ coating leads to lower magnetization and more regions of discontinuity between ferromagnetic volume. The lowest magnetization of about 202 emu·g$^{-1}$ is found for powder milled for 24 h, compacted, and cured at 900 °C, which is much greater than results from literature.

As the amount of crystal imperfections increase, microstrain and thus hardness also increases. Nanoindentation confirm higher hardness for more deformed powder. Increased domain volume leads to increased hardness, as apparent for composites of Fe–$Al_2O_3$ (50/50) with hardness of 4.2 GPa [122]. These matrices have lower densities (∼4.9 g·cm$^{-3}$) compared to that of our compacts with greater than 6.8 g·cm$^{-3}$ densities. Higher curing temperatures result in reduced hardness, due to significantly more stress relief and recovery. Elastic moduli remain constant throughout the milling process. Variance in measurements is due to possible indentation from grain boundaries or alumina coating.

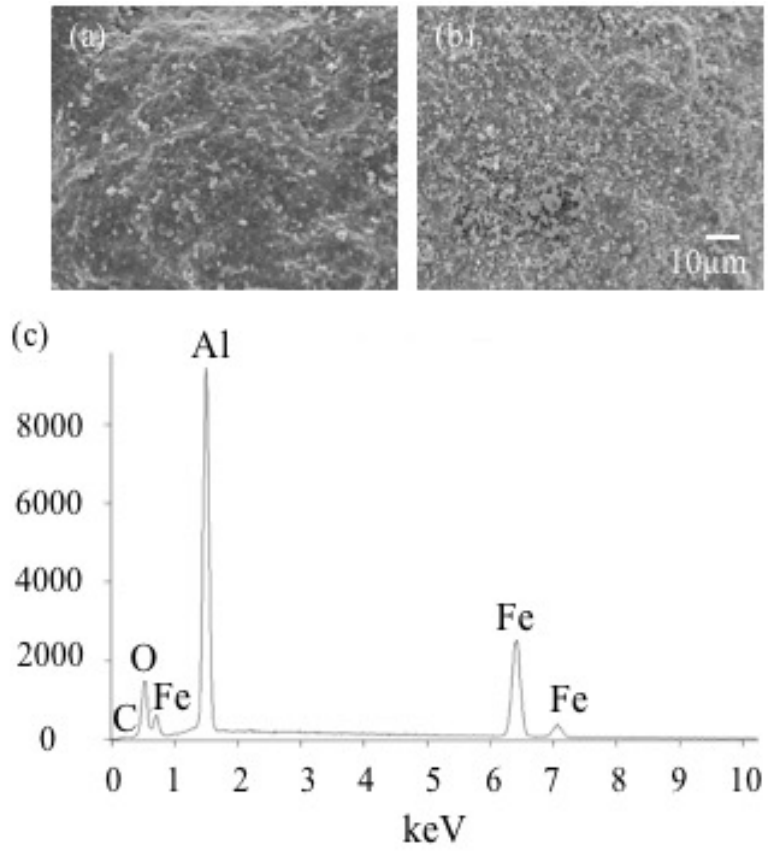


**Figure 4.13:** Surface of iron powder milled for 4 h with (a) 1 mm and (b) 3 mm $Al_2O_3$ media, with (c) EDS spectra of particle in (b).

***Effect of Media Ball Size***

With a constant milling time, structural, mechanical, and magnetic properties are found to depend on media ball sizes, ranging from 0.5 to 3 mm in diameter. SEM images presented in Figure 4.12 show powder milled with (a) 1 mm or (b) 3 mm media balls for 4 h. Spherical particles are obtained when milled with large (3 mm) $Al_2O_3$ media balls, but are not seen in powder milled with smaller (0.5 or 1 mm) media balls.

EDS, performed in conjunction with SEM images, allows for chemical analysis of exterior regions of powder milled for 4 h (Fig. 4.13). Finer particles of aluminum-oxide sufficiently coat iron powder surfaces via ball milling with alumina media. Powder milled with 3 mm $Al_2O_3$ media have increased amounts of agglomerations of finer particles on outermost regions as seen in Figure 4.13b, similar

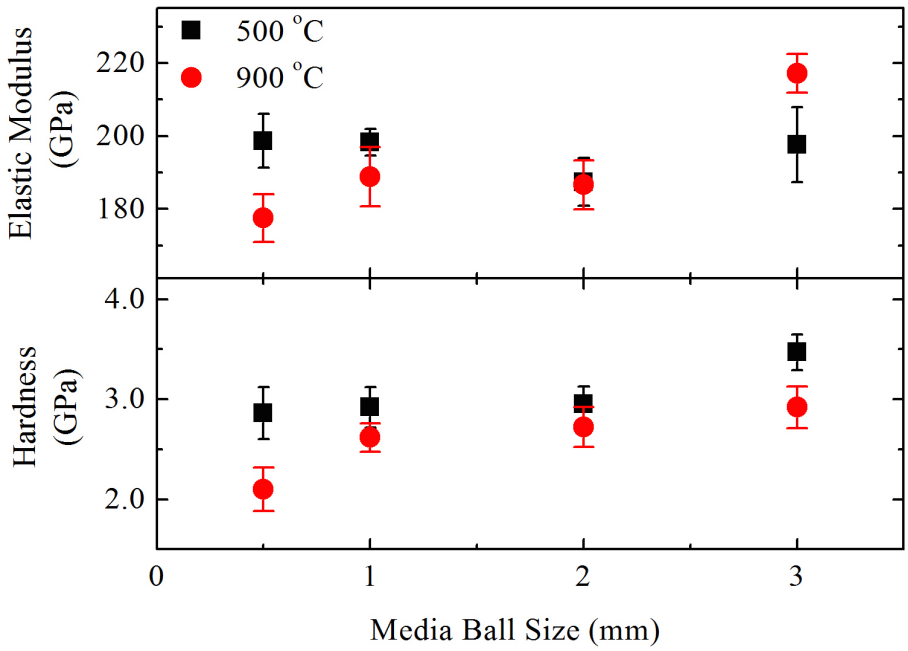


**Figure 4.14:** Nanoindentation results of hardness and elastic modulus for powder milled for 4 h with different media ball sizes.

to that of powder milled for longer periods of time shown previously. The dominant elemental components of the surfaces of milled powder were Al, O, and Fe (Figure 4.13c). All powder milled for 4 h with 0.5 to 3 mm media have evidence of $Al_2O_3$ coating according to XRD data. Fe peaks broaden and peak intensity decreases as media ball sizes increases indication of increased microstrain and decreased crystallite size, similar to previously reported XRD patterns for increased mill times.

We found the hardness of powder milled with 0.5 or 1 mm balls to be slightly lower than the hardness of powder milled with larger media balls, as presented in Figure 4.14. Less deformation and lower defect densities are present when smaller media balls are used, therefore reduced hardness is expected. As before, compacts cured at higher temperatures have lower hardness. Elastic moduli remain relatively constant throughout, as expected. Magnetization is found to depend greatly on media ball sizes. Higher saturation magnetization is measured for powder milled with 0.5 or 1 mm media balls for 4 h, and is found to be similar to that of powder milled for 2 h with 2 mm balls. Powder milled with 3 mm balls for 4 h result in lower magnetization, similar to that of powder milled for 8 or 16 h with 2 mm media balls. As previously reported, higher curing temperatures

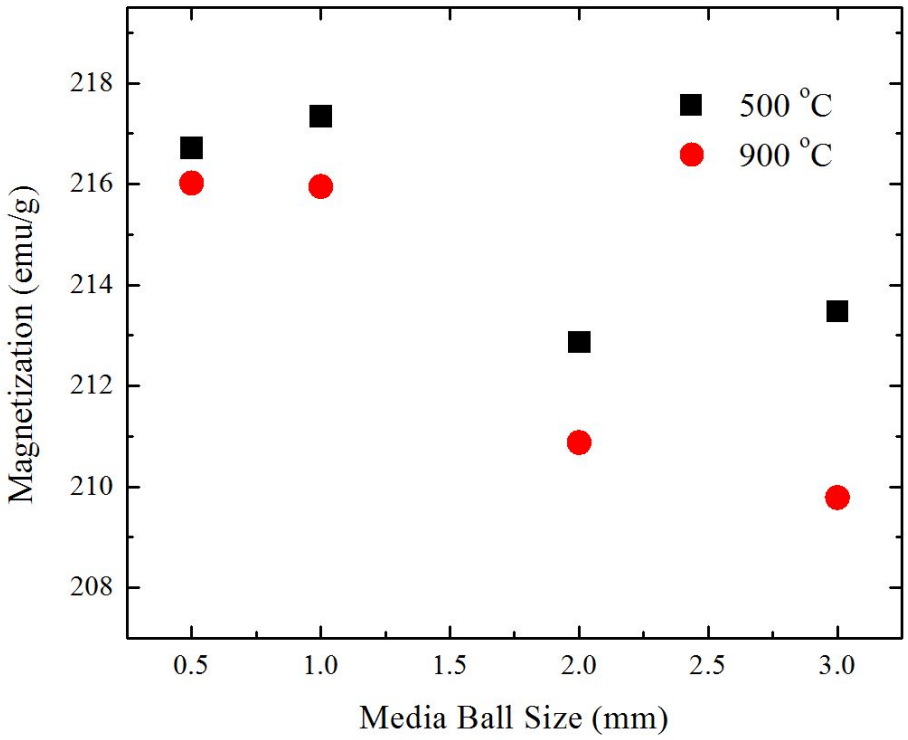


**Figure 4.15:** Changes in the $M_s$ value as a function of media ball sizes.

have lower magnetic saturation of powder compacts.

Reduced amounts of $Al_2O_3$ coating are present for smaller media balls when milling time is held constant, due to reduced surface areas and collision velocities. Shin et al. [120] found that milling efficiency for particle size reduction is directly correlated to ball diameter and rotational speeds. Smaller diameters greatly reduce the media ball speeds due to lower mass and therefore have reduced kinetic energy resulting in less damaging effects. Iron powder milled for 4 h with 3 mm media balls have larger amounts of alumina coating, reducing the overall ferromagnetic volume, and higher amounts of defect densities, increasing the hardness, as compared to powder milled with 0.5 to 2 mm balls. The data shows that powder milled for 4 h with 3 mm media balls, compacted, and cured at 500°C produce the highest hardness (∼3.5 GPa) and high magnetic saturation (∼213 emu·g$^{-1}$). Similar results are found for powder milled for 8 h with 2 mm media balls, indicating smaller media balls can obtain comparable, but require longer milling times. Magnetic saturation is found to be comparable for both curing temperatures, for these two sample sets. Equivalent deformation

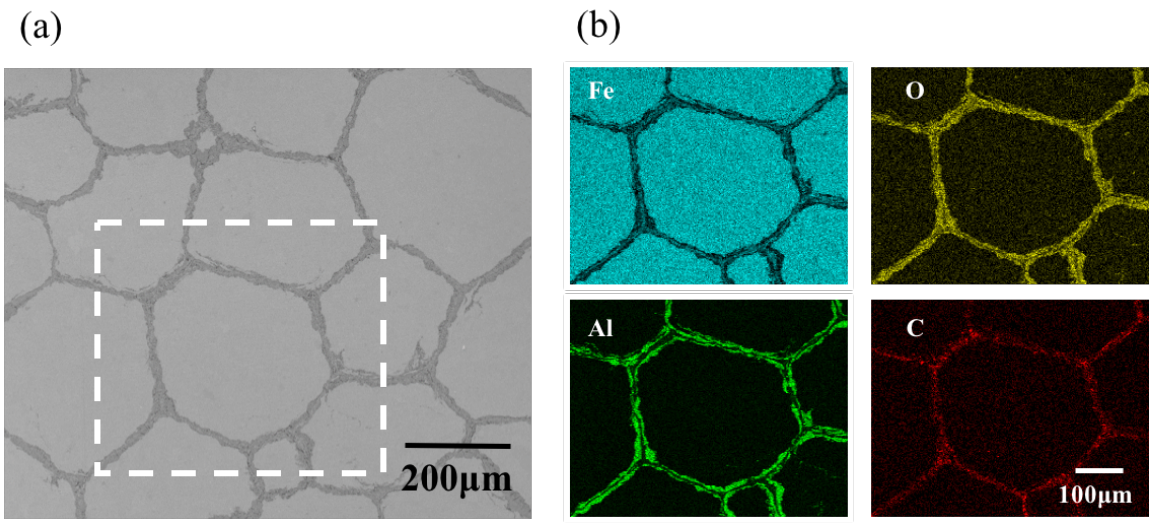


**Figure 4.16:** SEM image and respective EDS maps for a powder compact of $Al_2O_3$–$Fe_3O_4$ dual coated Fe powder.

may have occurred, creating similar defect densities and coating layer thicknesses, which supports similar magnetic properties. Additionally, powder milled for 4 h with 0.5 or 1 mm media balls have comparable magnetic and mechanical results to powder milled for 2 h with 2 mm media balls. These similarities are directly relatable to their structural defects and alumina coating content. Our results permit a tunability of magnetic saturation and hardness, dependent on milling time and media ball sizes.

## 4.4 $Al_2O_3$–$Fe_3O_4$ Dual Coating

The following study is performed to investigate the effect of a ferrimagnetic coating layer addition to $Al_2O_3$–coated Fe particles. Reducing the overall nonmagnetic volume of the system theoretically will improve magnetic saturation. As previously shown, Fe powder mechanically milled at room temperature with alumina media balls in an alumina vial are coated with $Al_2O_3$. Iron powder milled with hardened steel media balls in an alumina vial also become coated with alumina. In fact, a dual layer of magnetite and alumina is developed with the addition of $Fe_3O_4$ submicron particles to the milling process. Powder surfaces analyzed by SEM show large amounts of texture and particle agglomerations, strong indication of a dense coating. XRD patterns of milled powder

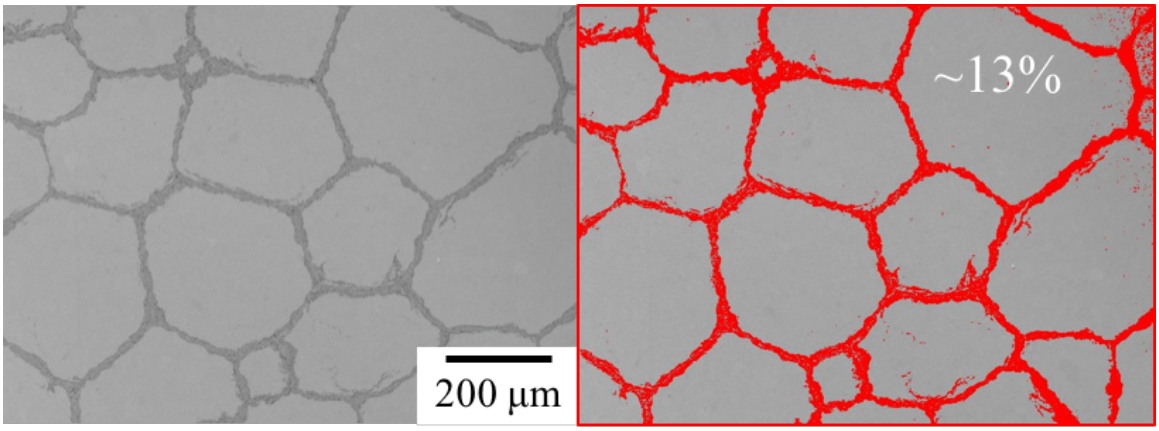


**Figure 4.17:** Coating volume percentage analysis for $Al_2O_3$–$Fe_3O_4$ dual coated Fe powder milled for 4 h with alumina media then 1 h with magnetite particles.

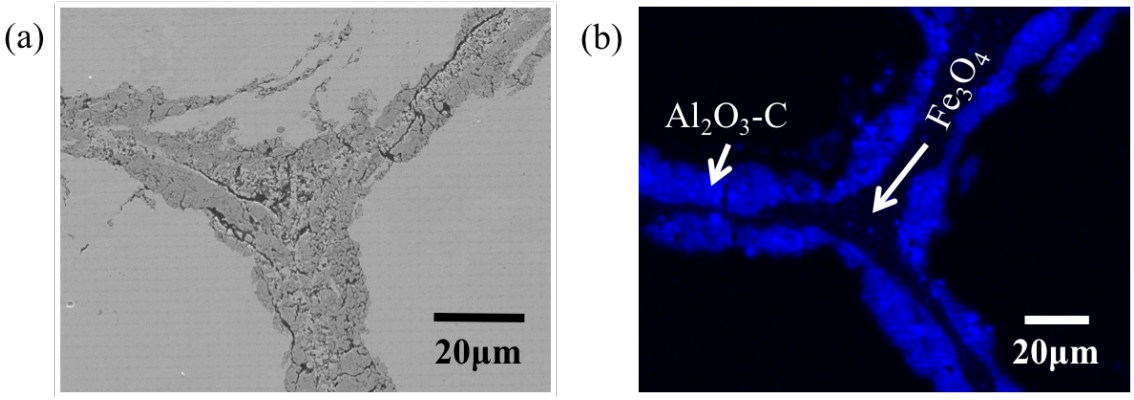


**Figure 4.18:** Higher magnification SEM image (a) illustrating the dual coating of $Al_2O_3$ and $Fe_3O_4$, with EDS map (b) of Al – blue and Fe – black.

expose alumina peaks for powder milled for 4 h or longer in an alumina vial. Diffraction patterns exemplify large regions of peak broadening and decreased peak intensity for longer milling times, evidence of internal defects and stressed regions [48].

EDS maps of powder compacts allow for the elemental analysis of the coating material and metallic powder. Figure 4.16 shows a powder compact from alumina and magnetite coated iron powder produced from the technique illustrated in Figure 4.2. Iron powder are first milled with hardened steel media balls in an alumina vial for 4 h and then milled for 1 h with $Fe_3O_4$ particles after the media balls are removed. Samples are then compacted and cured for 1 h at 700°C to properly stress relieve Fe, but not degrade magnetic saturation, shown in Figure 4.11 and 4.15 for

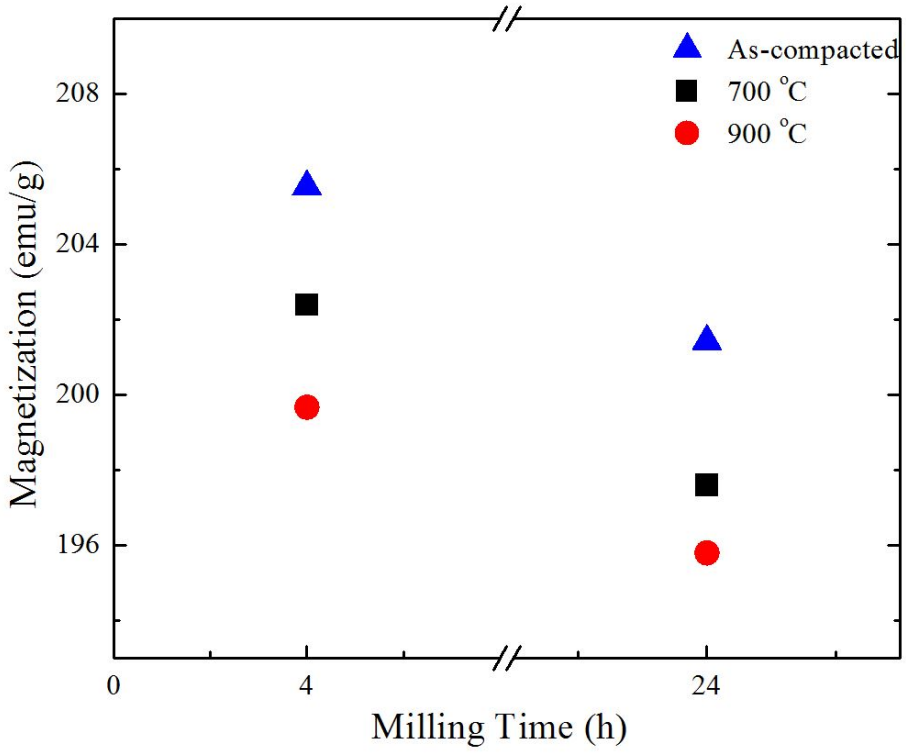


**Figure 4.19:** VSM results for magnetic saturation of $Al_2O_3$–$Fe_3O_4$ dual coated Fe powder milled at 4 h and 24 h.

$Al_2O_3$–coated Fe. Interfaces between iron powder, seen in Figure 4.18 are aluminum–oxide with carbon and iron–oxide material, and most reasonably alumina and carbon from the milling media and magnetite from the added powder. Image analysis determines the coating amount to be about 13 vol% from the cross sectioned SEM image presented in Figure 4.16, reproduced in Figure 4.17 for 4 h of milling in $Al_2O_3$ vial with hardened steel media balls then 1 h with $Fe_3O_4$ particles. This analysis indicates an addition of ∼6 vol% $Fe_3O_4$ is added to the previous analysis of ∼7% coating for milling with alumina media balls for 4 h (Figure 4.8b). Possible phase transformations to $FeAl_2O_4$, $Fe_2O_3$, or FeO may have occurred [115, 123], but are undetectable via SEM. Alumina, carbon, and magnetite content completely isolate iron powder from one another eliminating metal–on–metal contact points.

The highest saturation magnetization for this study is measured for powder compacts milled for 4 h with no neat treatment, shown in Figure 4.19. This indicates that the least amount of $Al_2O_3$

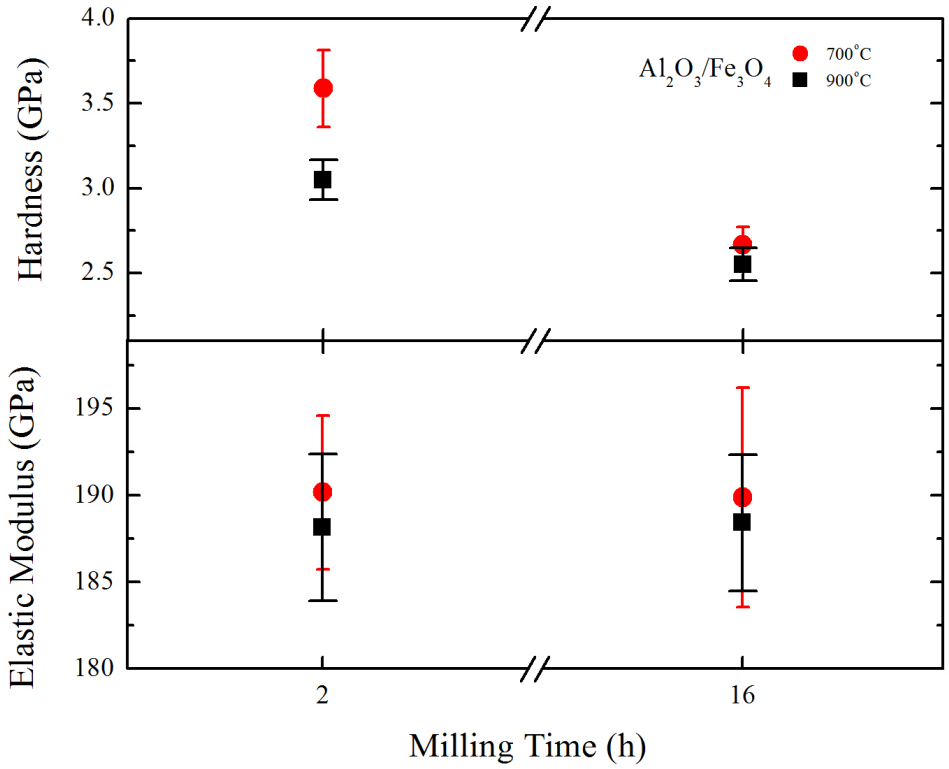


**Figure 4.20:** Nanoindentation results comparing elastic modulus and hardness for $Al_2O_3$–$Fe_3O_4$ dual coated Fe powder.

and C coating is necessary to improve magnetic properties, and that a non-favorable addition of carbon impurity drastically lowers magnetic performance. Lower magnetization results are found for powder milled for longer periods of time, which produces more internal defects and allows for more alumina and carbon coating, therefore less magnetic volume. All powder compacts in this study have relatively low coercivities of 40 Oe or below. VSM measurements are not entirely accurate for determining absolute coercivity, therefore specific coercivity values are not presented. Elastic modulus and hardness ratings are explored using nanoindentation at a depth of 200 nm. Results for powder compacts with $Al_2O_3$–$Fe_3O_4$ coated iron are presented in Figure 4.20. As to be expected, elastic modulus remains constant; however, unexpectedly hardness decreases with increasing amounts of milling. Higher curing temperatures result in lower hardness ratings, indication of proper stress

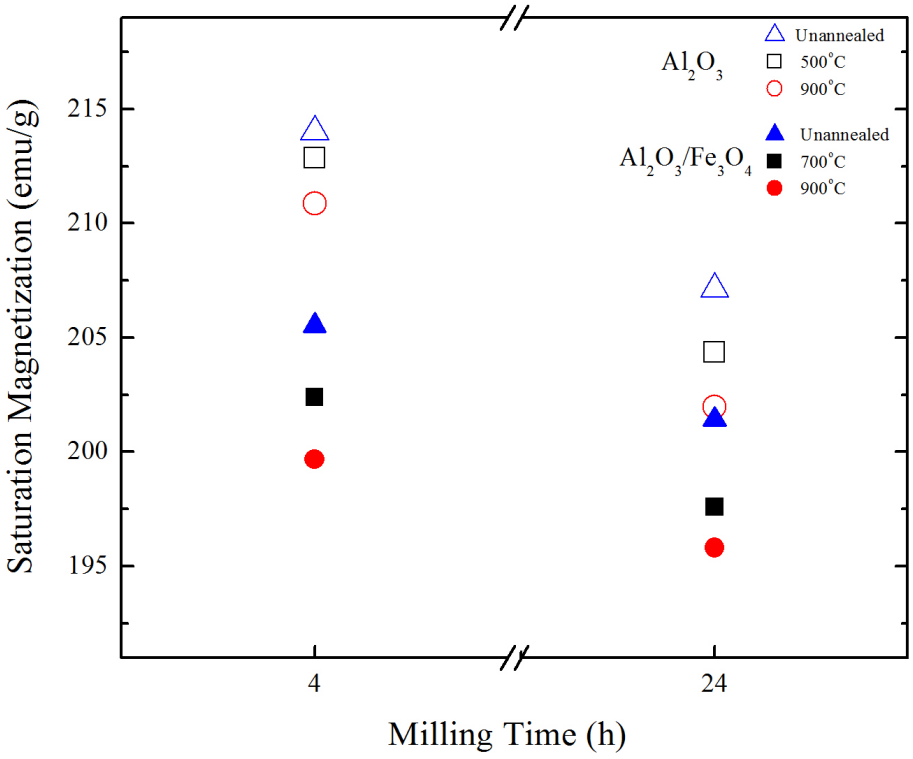


**Figure 4.21:** Saturation magnetization of $Al_2O_3$–$Fe_3O_4$ dual coated Fe powder.

relief and recovery of iron. Mechanical properties of alumina coated iron powder compacts follow expected trends of increasing hardness as more deformation is introduced [48].

## 4.5 Conclusions

Soft magnetic composites comprised of electrically insulated magnetic powder are ideal for more efficient, high frequency applications. Ferrous powder coated with nonmagnetic ceramic material will reduce metal–on–metal contacts to minimize eddy current losses and improve overall electrical efficiency. Ball milling methods allow for highly dense, "self–coated" powder to be synthesized directly through the use of a preferred media. The experimental technique used in this work successfully coat Fe powder with $Al_2O_3$ and allow for improved magnetic and mechanical properties compared to literature. Low BPRs allow for more contact points to emerge between powder thus decreasing

collision velocities of media balls and minimizing particle size reduction. Small media balls ($\leq$3 mm), permit uniform coatings and stressed regions that result in high magnetic saturation ($\sim$210 emu·g$^{-1}$) and good mechanical hardness ($\sim$3.0 GPa) even after curing temperatures of 900 °C. Alumina coating allows for proper isolation of individual iron particles to reduce eddy current losses and be used for high frequency applications.

We present studies on $Al_2O_3$ and $Al_2O_3$–$Fe_3O_4$ coated iron powder by means of mechanical milling with relatively small media ball sizes. The measured magnetic and mechanical properties show promising features for use as SMCs in high frequency applications. Alumina coated powder produced from low-energy ball milling methods allow for complete isolation of iron particles, eliminating metal–on–metal contact points. Although alumina is nonmagnetic, powder compacts still possess relatively high saturation magnetization and low coercivities, as well as good elastic moduli and hardness ratings. Combining alumina and magnetite coatings may be useful, however, our work resulted in an undesirable carbon contamination, which even 0.1% impurity will greatly reduce magnetic performance. VSM results are seen in Figure 4.21 for powder compacts of $Al_2O_3$ coatings [48] and $Al_2O_3$–$Fe_3O_4$ [102] dual coating layers. Ball–to–powder ratios are critical in determining deformation and size reduction outcomes using high-energy ball milling. Low BPRs allow for minimal amounts of particle size reduction while continuing to deform powder to obtain the desired mechanical strength.

Various media types such as zirconia, readably available and with an even higher melting point than alumina, are predicted to have similar trends in structural and coating layer dependence of milled powder. Our "self–coating" technique has little potential of being utilized in industrial manufacturing because of the costly medium necessary for coating powder and high compaction pressures required to form parts. Alumina as a coating material does have great potential for SMC applications due to proven magnetic saturation and hardness results shown here, however, higher–than–normal compaction pressures are required in order to obtain high density compacts. Overall, alumina "self–coated" iron powder are synthesized and studied for their improved magnetic and mechanical properties. In the following two sections, we outline our results of using solely ferrimagnetic coatings

and how they compare to $Al_2O_3$ related studies with varying parameter space in milling times and particle sizes.

# Chapter 5: $Fe_3O_4$ Coatings

## 5.1 Introduction

Soft magnetic composites (SMCs) comprised of ferromagnetic powder insulated with electrically resistive coatings that are also magnetic can be used in electromagnetic devices to improve efficiency and increase frequency. Insulating coating layers isolate eddy currents within each ferromagnetic particle to reduce eddy current losses, while magnetic coating layers allow for reduction of hysteresis loss by reducing nonmagnetic regions as pinning sites for domain walls. In SMC materials, the coating layers play critical roles in reducing the conductivity between ferrous particles and allowing for in-particle (microscopic) eddy currents as opposed to inter-particle (macroscopic) eddy currents that cause overheating (Fig. 2.3. However, without particle–to–particle sintering, mechanical strength and often density suffer. The ideal coating material can undergo higher compaction pressures and heat treatments, while remaining electrically insulative, magnetic, and mechanically durable. Increasing compaction capabilities will allow for maximum density and much improved magnetization. Elevated temperature treatments will allow for not only recovery, but also grain growth and potential sintering of the coating material. Inorganic coating layers can withstand higher cure temperatures as shown previously for $Al_2O_3$ coatings, but if they are nonmagnetic they will greatly increase the hysteresis loss component of core loss and reduce magnetization [23, 40, 48, 54, 78]. Soft ferrites have very high electrical resistivity and good magnetization allowing for reduction of eddy current and hysteresis losses, respectively [7, 18, 27, 51]. Magnetite ($Fe_3O_4$) is a semiconductor material with resistivity of $\rho \sim 10^{-2}$ $\Omega$·cm, while crystalline Fe is highly conductive ($\rho \sim 10^{-6}$ $\Omega$·cm), both of which are limited to low frequencies because of their conductive nature. Combining the two types of magnetic materials by utilizing a ferromagnetic Fe powder core with ferrimagnetic ferrite coating allows for higher frequency applications (>400 Hz) while maintaining high soft magnetic properties after curing temperatures above 600°C. Here we study $Fe_3O_4$–coated Fe powder composites via mechanical milling and discuss their magnetic properties including core loss, magnetic permeability,

and coercivity as well as their physical and microstructural properties including density, transverse rupture strength, and chemical composition.

We begin this chapter with a thin film representation of the coating–core interface using $Fe_3O_4$–Fe bilayers, as outlined previously in Figure 3.1. The study of an ideal crystalline state from thin films is used to compare to a highly strained state from powder composites, for magnetic property correlation to microstructure.

## 5.2 Thin Film Studies

Magnetic thin film heterostructures play an important role in the performance of many devices, including magnetic tunnel junctions, multiferroic memories, and magnetic random access memories (MRAMs) [124–126]. Many of the fundamental properties that make these systems so attractive are dictated by film layer thickness and interactions arising near interfaces, where surface termination and symmetry breaking induce exotic behavior [127]. Iron and iron oxides in particular offer considerable versatility for these electronic and magnetic systems [128, 129]. For instance, $Fe_3O_4$ has proven to be a promising candidate for these systems because of its high Curie temperature, weak magnetocrystalline anisotropy, and structural compatibility [130–132]. Microstructural effects, such as strain and roughness, as well as crystallinity can also significantly affect the performance of these devices [128, 133, 134]. Interfacial roughness results in greater area of interfacial contact and can enhance demagnetizing effects, while strain can introduce magnetoelastic effects [135]. In addition, texture and crystallinity of film layers plays a key role in magnetocrystalline anisotropy, requiring more applied field to obtain similar magnetic responses [108].

Many questions remain about how interface structure affects the evolution of uniaxial anisotropy in ferrite composites, nominally Fe–$Fe_3O_4$ heterostructures. Abrupt changes in magnetic anisotropy are known to occur at $Fe_3O_4$ interfaces in spin valves [136]. The origin of this effect is debated, but it has been found that $Fe_3O_4$ can induce magnetic proximity effects in adjacent layers. Furthermore, the connection between interfacial misfit dislocations and coercivity is poorly understood. Previous studies have focused extensively on antiphase boundaries in $Fe_3O_4$, but the presence of misfit dislocations in Fe–$Fe_3O_4$ composites has only received cursory attention [137]. Such defects can act to

pin magnetic domain walls and can greatly affect tunneling magnetoresistance as found in MgO–based tunnel junctions [138]. This necessitates a more predictive understanding of the relationship between coercivity, anisotropy, epitaxial strain, surface morphology, and dislocation density. For these reasons, we study $Fe_3O_4$–Fe single crystal thin film systems to correlate the effect of layer thickness and epitaxial strain on magnetization and dislocation density.

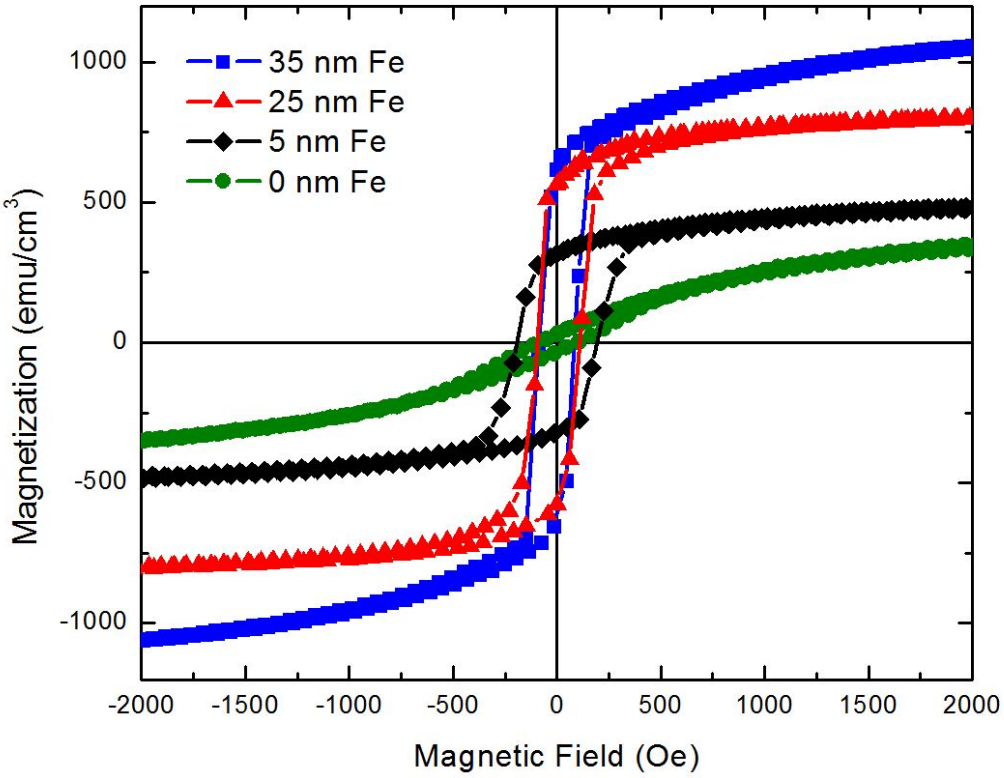


**Figure 5.1:** B–H loops measured from VSM for capped $Fe_3O_4$–Fe bilayers.

The density of interfacial dislocations depends on the Fe layer thickness and acts with epitaxial strain to determine magnetic properties, nominally coercivity, of the thin film system. In thin film heterostructures, electronic structure and magnetic properties are tunable via film growth conditions, microstructure, and layer thicknesses [139, 140]. Magnetization in $Fe_3O_4$–Fe films depends on layer thicknesses; potentially allowing for increased magnetic properties with decreased layer thickness for magnetite coated powder [141]. Matsubara et al. studied Fe–alloy films, prepared on MgO (100) with large lattice mismatches, to have dislocations around 10∼20 nm from the interface, proving that dislocations help relieve strain at the interface [142]. Thin film multilayers in this thesis allow

for a good representation of the structural properties present at the coating shell and powder core interface in a model system. In addition, epitaxial, iron alloy and iron oxide thin films have a variety of applications such as microwave devices, read/write heads, sensors, MRAMs, and spin filter junctions [143–145]. Therefore, $Fe_3O_4$ and Fe bilayers will be studied to analyze the dependence of layer thickness, microstrain, and interfacial defects on magnetic saturation and coercivity, to be correlated to bulk powder studies (Fig. 3.1), described below.

### 5.2.1 Experimental Methods

Commercial 1x1 $cm^2$ MgO (001) substrates (MTI International) are cleaned using acetone and isopropyl alcohol. $Fe_3O_4$ layers are deposited at an oxygen pressure of $\sim$2x$10^{-6}$ Torr and a substrate temperature of 250°C using molecular beam epitaxy (MBE). $Fe_3O_4$ layers are controlled throughout the studies to be 35 and 45 nm with and without capping layers, respectively. Fe layers are then deposited on top of $Fe_3O_4$ layers without substrate heating. Fe thicknesses are 20, 25, and 30 nm with no capping layer and 5, 25, and 35 nm with a La capping layer. The comparison of non–capped to capped thin films are used to isolate the effect of surface oxide on magnetic properties and dislocation density. Cross–sectional transmission electron microscopy (TEM) samples were prepared using Focused Ion Beam (FIB) method. Bright field and diffraction images are taken using a JEOL 2100 $LaB_6$ TEM operating at 200 keV. High–resolution transmission electron microscopy (HRTEM) is used to determine the quality of interfaces and surface morphology and orientation imaging to determine texture and crystallinity (Nanomegas ASTAR$^{TM}$) [146]. We combine TEM measurements with ferromagnetic resonance (FMR) to correlate local microstructure to magnetization and crystalline anisotropy. FMR studies are performed at room temperature at 9.55 GHz. The sample is placed on the sidewall of the cavity and subjected to a varying magnetic field to measure the out–of–plane variation of the resonance field. Bulk in-plane hysteresis loops are measured using a Quantum Design PPMS with VSM attachment at room temperature with the field applied along the MgO (100) direction.

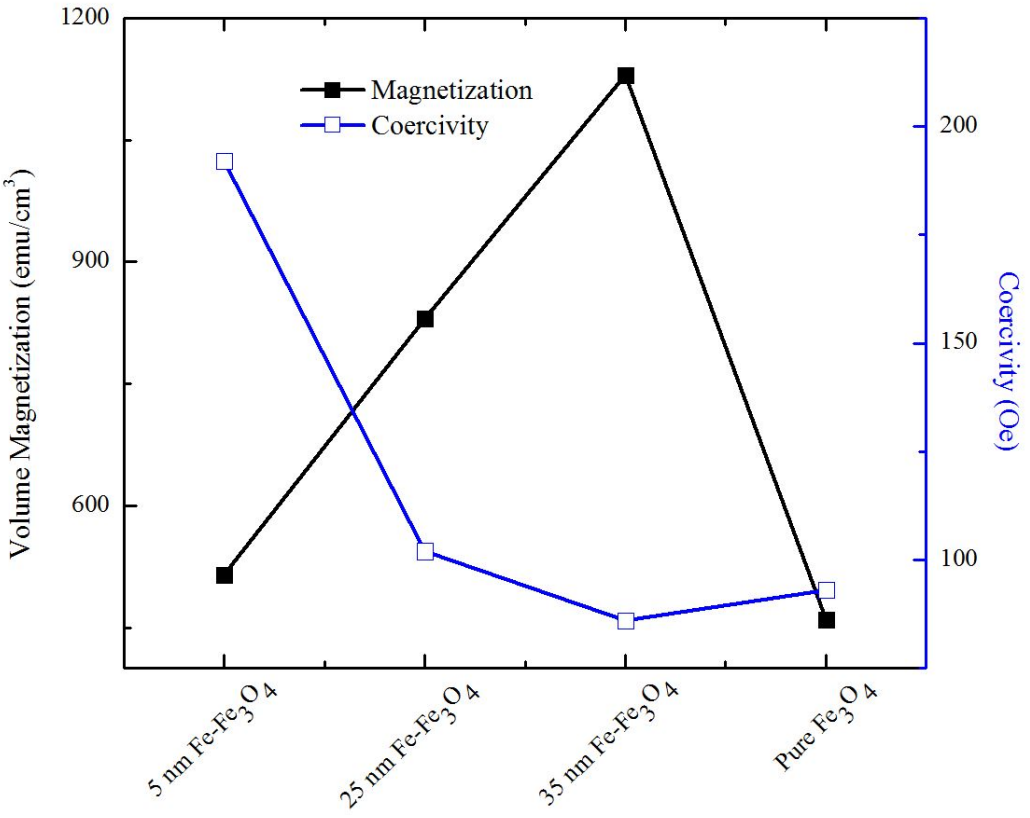


**Figure 5.2:** $M_s$ and $H_c$ values for capped $Fe_3O_4$–Fe bilayers.

### 5.2.2 Results and Discussion

We present $Fe_3O_4$–Fe bilayers deposited on MgO (100) substrates with La capping layers to control surface oxidation. Previous results of uncapped $Fe_3O_4$–Fe bilayers deposited on MgO (100) substrates without capping layers was presented by McDonald [11]. This thesis compares the effect of adding a capping layer to magnetization dependence on Fe layer thickness and microstructure defects at coating–core interface. Figure 5.1 illustrates VSM measurements for capped films. There is clearly an increase in magnetization as Fe layer thickness increases, nominally an increase in ferromagnetic volume is present. Likewise, the coercivity from 5 nm Fe layer to 25 nm Fe layer decreases for similar reasons. A comparison of $M_s$ and $H_c$ is seen in Figure 5.2. Comparing magnetization curves to uncapped films (Fig. 5.3), we see similar trends for 0 nm Fe layers, nominally $Fe_3O_4$–MgO films. The magnetization of uncapped films is clearly affected by both dislocation density and surface roughness, both of which are known greatly to influence the magnetic properties of these

materials [147]. Specifically, the effect of surface oxidation and misfit dislocations play key roles in coercivity, both elaborated on by Spurgeon [50].

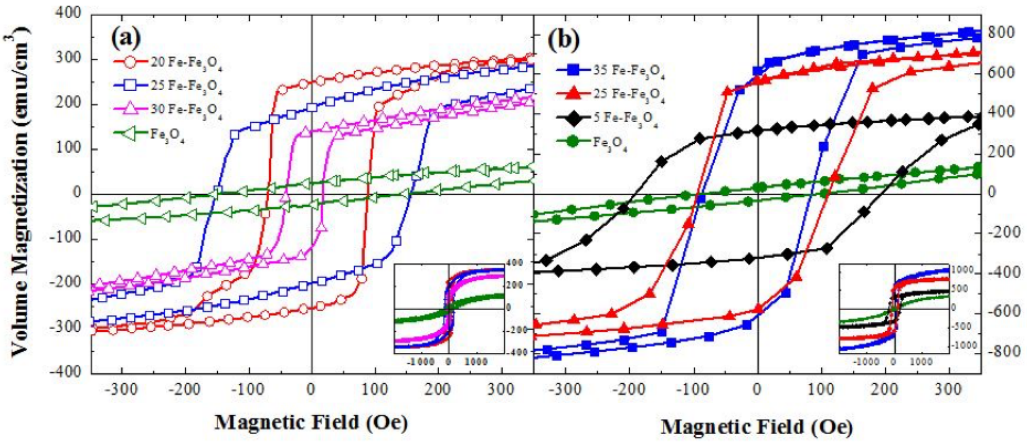


**Figure 5.3:** B–H loops of (a) uncapped films [11] and (b) capped films.

The presence of surface oxide greatly reduces the overall $M_s$ as seen in the inset of Figure 5.3a, which is result from two $Fe_3O_4$–Fe interfaces and thus more regions for dislocations to affect magnetic properties. The reduced $M_s$ is not attributed to the formation of antiphase boundaries (APBs) because the films are saturated at relatively low fields ($H_{sat}$ below 5 T) [148, 149]. We use a capping layer to overcome surface oxidation and potentially roughness, using the same deposition parameters previously used by McDonald [11] and Spurgeon [50], however, with the addition of a 3–5 nm La top layer. This layer is used to avoid misrepresentation of magnetic responses from additional ferrite material formed when the film is exposed to air after deposition. In–plane magnetic hysteresis measured by VSM (Fig. 5.3b) of films with La capping layers indicate magnetization is dependent on ferromagnetic volume and hence Fe layer thickness. Coercivity is found to be correlated with Fe layer thickness for capped films, but not for uncapped films, suggesting that in the uncapped films, the surface roughness and oxidation play a larger role than the dislocation density in the capped films. When surface oxidation is minimized a clear trend of decreasing coercivity with increasing iron thickness (Fig. 5.2) is seen. This is a promising result for tunable applications in need of fast switching or hard magnetic properties.

However, regulated magnetic properties must also be balanced with magnetocrystalline anisotropy

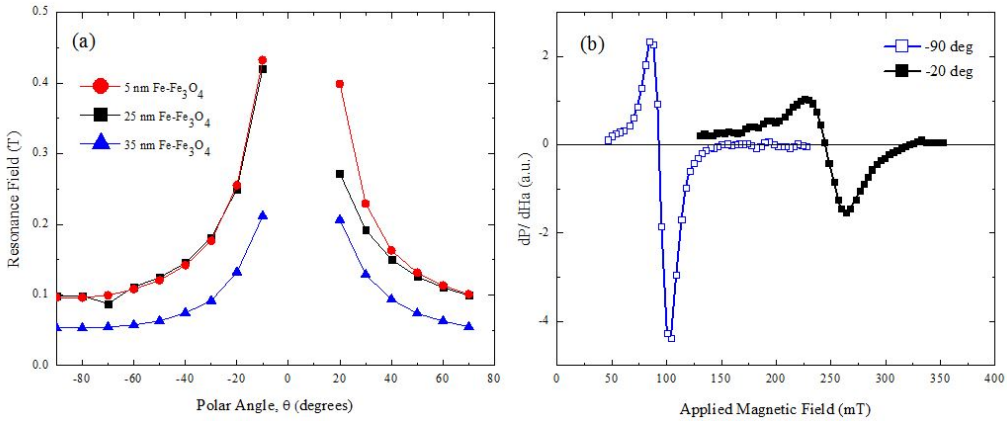


**Figure 5.4:** (a) Polar angular dependence of the resonance field and (b) typical FMR spectra for the 25 nm Fe–$Fe_3O_4$ capped film of a perpendicular (-90°) and approaching parallel (-20°) geometries.

for true tunability of these heterostructures. Moreover, the inhomogeneous stress distribution around the dislocations can pin domain walls, leading to a linear increase in magnetocrystalline anisotropy with lattice deformation [150]. XRD showed that there is nearly half of the out–of–plane strain between the 20 and 30 nm Fe uncapped samples, which is likely due to the difference in interfacial dislocation density in these two film thicknesses [11, 50]. Dislocations and misfit strain can introduce a magnetoelastic contribution to the in-plane uniaxial anisotropy of the Fe layer. FMR measurements at 9.55 GHz indicate good angular dependence of all capped films, shown in Figure 5.4a. The large resonance field difference between parallel (–90°) and perpendicular (0°) geometries (Fig. 5.4a) demonstrate large anisotropies for the 5 and 25 nm capped films. However, it is critical to note that anisotropy calculations to fit these curves are beyond the scope of this paper, but have previously been reported by Zakeri et al. [151]. The maximum resonance is approached along the film normal for all samples, indicating in-plane magnetization alignment is favored. The 25 nm Fe–$Fe_3O_4$ film however shows interesting, asymmetrical resonance curves approaching the perpendicular geometry. Typical FMR spectra are presented in Figure 5.4b for the 25 nm Fe–$Fe_3O_4$ film, which illustrates a large resonance response and a small linewidth $\Delta B$=20 mT at -90°. These results are evidence of randomly oriented grains and thus a large magnetocrystalline anisotropy. To confirm this, TEM images are obtained and coupled with automated crystal orientation mapping (Fig. 5.5)

using the Nanomegas ASTAR$^{TM}$ system [146]. All capped films show clean $Fe_3O_4$–MgO interfaces in TEM as comparable to uncapped films shown by McDonald [11]. In addition, TEM images confirm the elimination of surface oxidation. However, surface roughness is still an issue for the 25 nm Fe–$Fe_3O_4$ capped film. Single phase maps are obtained for all films, but uniform orientation maps are only obtained for the 5 and 35 nm Fe–$Fe_3O_4$ films (Fig. 5.5a and c). The orientation map for the 25 nm Fe–$Fe_3O_4$ sample reveals a polycrystalline film. While the randomly oriented grains do not play a pronounced role in the coercivity and saturation magnetization, they do have an effect on the magnetocrystalline anisotropy as shown in the FMR results. These findings are consistent with previous results that highlight polycrystalline ferrites, which have randomly oriented grains, showing wider absorption lines from FMR due to crystalline anisotropy [152]. Therefore, we conclude that coercivity is dependent on thickness (including surface oxide and dislocation effects), but magnetocrystalline anisotropy is largely dependent on crystallinity and grain orientation.

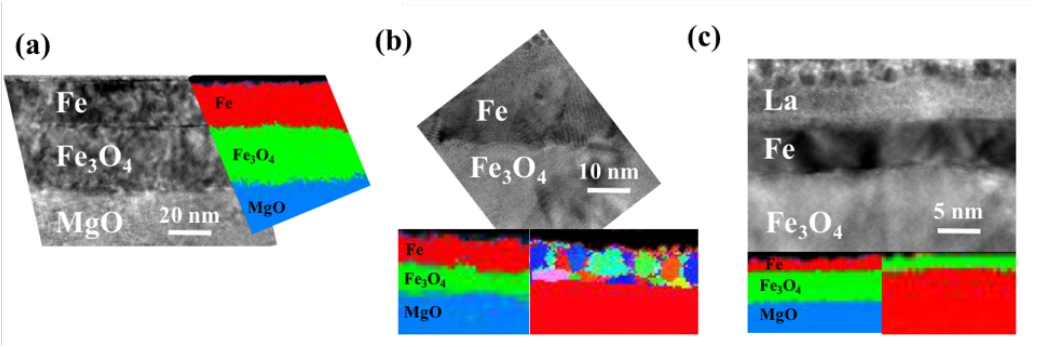


**Figure 5.5:** Cross-sectional TEM images of Fe–$Fe_3O_4$ interfaces in the (a) 35, (b) 25, and (c) 5 nm Fe layer thicknesses capped films. Colored phase maps for each film indicate single phase layers with Fe (red), $Fe_3O_4$ (green) and MgO (blue) as labeled. Orientation maps seen on the bottom right of (b) and (c) illustrate the polycrystallinity of the 25 nm film and crystallinity of the 5 nm film.

We investigate the microstructure and magnetic properties of Fe–$Fe_3O_4$ thin film systems using TEM, VSM, and FMR. We find that magnetic saturation and coercivity are dependent on Fe layer thickness, with thicker films scaling toward improved "soft" magnetic responses. This is associated with a similar trend in dislocation density, as confirmed by TEM [11, 50]. We show that such strain acts to impose an in–plane uniaxial anisotropy on the composite that depends on thickness. The comparison between films with and without a capping layer provides valuable information that reveal

a cooperative effect of surface roughness, dislocation density, and overall crystallinity on magnetization. These findings highlight the importance of crystallinity and reduction of surface oxidation on magnetocyrstalline anisotropy and magnetization. Our results suggest that the precise engineering of interfacial roughness, strain, and film crystallinity may be used to tune magnetic properties in a predictive manner. Knowing that thicker Fe layers allow for higher magnetic saturations and lower coercivities can be used in the following sections of powder studies. Likewise, knowing that polycrystalline Fe layers increase coercivity in films can be used to reduce grain size and increase crystallinity in powder studies.

## 5.3 Powder Studies

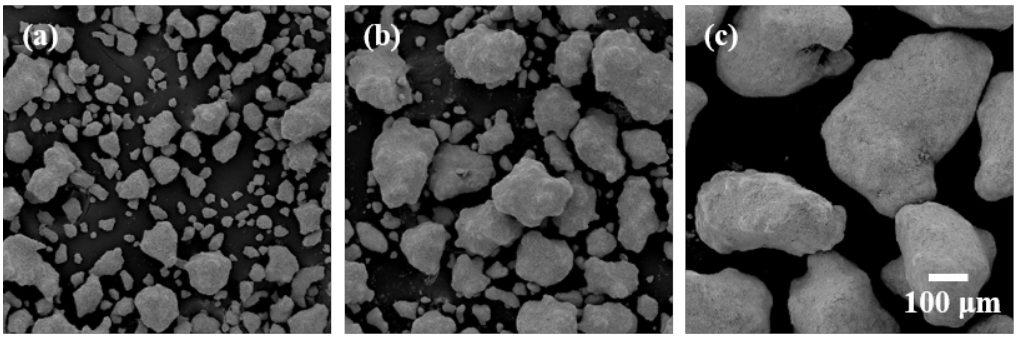


**Figure 5.6:** SEM images of $Fe_3O_4$–coated Fe powder with three particle size classifications: (a) fine, (b) medium, and (c) coarse.

The second part of this chapter utilizes magnetite, $Fe_3O_4$, as a coating material on pure Fe powder for bulk comparison to thin film studies. $Fe_3O_4$ is used for its high magnetization ($M_s$= 92 emu·g$^{-1}$) and not its resistivity ($\rho\sim10^{-2}$ Ω·cm). We note that $Fe_3O_4$ undergoes a phase transition to FeO at 570°C [96]; however, this structure is unstable at room temperature and the compound will return to $Fe_3O_4$ or $Fe_2O_3$ depending on the atmosphere and rate of cooling [153]. Our research discusses the microstructural evolution of the coating layers and Fe powder with respect to temperature because of the lack of discussion in prior literature. The primary focus has been on magnetic characterization of SMCs, which results in microstructural features of coating layers to be overlooked. Agglomerations of ferrite coating before and after pressing, along with non-uniform layers have been presented, but not discussed in terms of coating microstructure and its effect on magnetic core

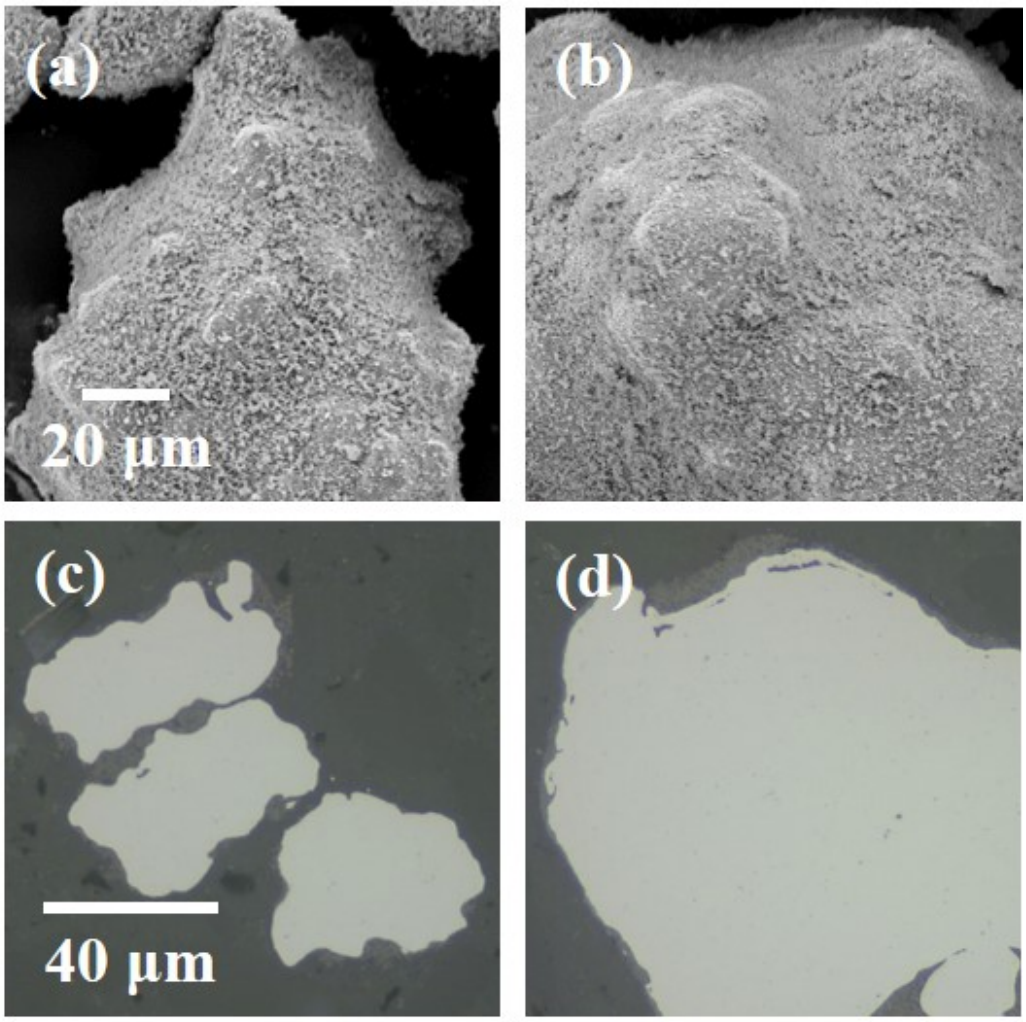


**Figure 5.7:** SEM images of $Fe_3O_4$–coated (a) fine and (b) medium Fe powder surfaces, and cross-sectional images of (c) fine and (d) medium coated Fe particles.

loss [27, 154, 155]. We first present the effect of particle size and cure temperature on magnetic permeability and core loss for the $Fe_3O_4$–coated Fe material system. Studies show that $Fe_3O_4$–coated Fe SMCs using Fe powder of average particle size 250 $\mu$m cured at 700°C, have the best overall results for low coercivity, high density, and low eddy current losses [156]. We then present the evolution of coating densification and the resulting magnetic effects of powder composites heat treated to elevated temperatures above the 570–775°C standard for SMC materials. Our research allows for direct correlation of hysteresis loss to coercivity under direct current (DC) conditions compared to coercivity at alternating current (AC), when eddy currents become prevalent. This chapter incorporates both ferri– and ferromagnetic materials for an ideal SMC design consisting of inner ferrous powder insulated with uniform layers of iron–oxide ($Fe_3O_4$) particles to allow for high soft magnetic properties after curing temperatures above 600°C. Here we present microstructural, mechanical, and magnetic characterization of $Fe_3O_4$–coated Fe powder composites via mechanical milling, and stress the importance of coating microstructure on magnetic properties as it pertains to temperature.

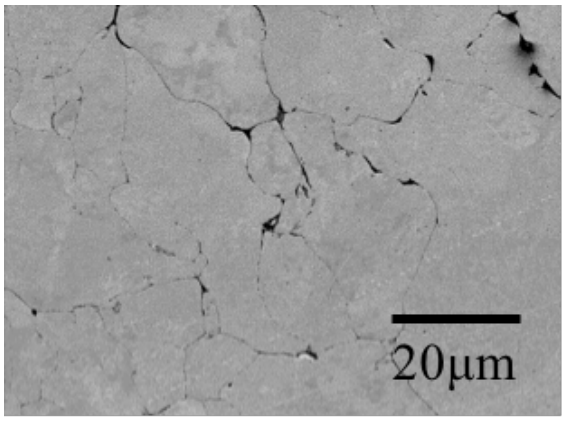


**Figure 5.8:** SEM image of uncoated Fe particles compacted and cured at 700°C.

## 5.4 Experimental Methods

Traditional powder metallurgy techniques are employed, which include ball milling to coat Fe powder with $Fe_3O_4$ and subsequently compact and cure the composites. We investigate the effect of mechanical milling to coat ferrous powder with ferrimagnetic, iron–oxide particles with particle size

**Table 5.1:** Physical, mechanical, and magnetic properties of uncoated and $Fe_3O_4$–coated Fe powder composites cured at 700°C. Density and TRS presented for mechanical testing bars, $\mu_{max}$ and DC coercivity ($H_c$) presented for magnetic toroid composites.

| **Sample** | **Density** ($g \cdot cm^{-3}$) | **TRS** (MPa) | $\mu_{max}$ | **DC** $H_c$ ($A \cdot m^{-1}$) |
|---|---|---|---|---|
| Fine Uncoated | 7.49 | 400 | 1990 | 155 |
| Medium Uncoated | 7.54 | 324 | 1720 | 159 |
| Fine Coated | 6.89 | 69 | 100 | 500 |
| Medium Coated | 6.92 | 41 | 75 | 502 |

ratios of about 40:1 (fine) and 100:1 (medium). High purity Ancorsteel 1000C Fe powder is provided by GKN–Hoeganaes Corporation. The initial particle size study sieves the as-received powder to three particle size classifications, fine (<105 $\mu$m), medium (105–250 $\mu$m), and coarse (250–425 $\mu$m). The second part of the $Fe_3O_4$–coated Fe study uses the as-received Fe Ancorsteel 1000C sieved to >75 $\mu$m. A high energy ball mill (SPEX 8000M) with a hardened steel vial is used to coat Fe powder with 10 wt% $Fe_3O_4$ particles of nominal particle sizes (1 to 5 $\mu$m) with no added media balls. This technique, traditionally used for pulverizing or size reduction of powder, is being modified to coat powder similar to low energy blending, however, without the use of a slurry material. Dry coating methods based on static forces and Van der Waals interactions between host (Fe) particles and guest (coating) material allow for complete isolation of ferrous particles based on kinetic energy [117]. No media balls are used during milling to reduce deformation and contamination, previously shown. Samples are milled for 30 minutes, then warm compacted (100°C) at 800 MPa, and cured in pure $N_2$ for 1 h at temperatures between 500°C and 1000°C.

Microstructural characterization includes the use of X-ray diffraction (XRD) analysis for determination of phases and and crystallite size of ferrite coating and scanning electron microscopy (SEM) with energy dispersive spectroscopy (EDS) for grain size, coating uniformity, and porosity of iron and coating layers. XRD patterns are obtained with a Rigaku SmartLab diffractometer at room temperature utilizing Cu–K$\alpha$ radiation ($\lambda$=1.541 Å) with a graphite monochromator to identify phase and structure of coated powder. We conduct $\theta$–$2\theta$ scans from 30°–85° with a step size of 0.02° and speed of 7.5 steps/min with a tube voltage of 40 kV and tube current of 30 mA. JADE software is used to analyze Fe, $Fe_3O_4$, and FeO peaks using a pseudo–Voigt fitting function, which is

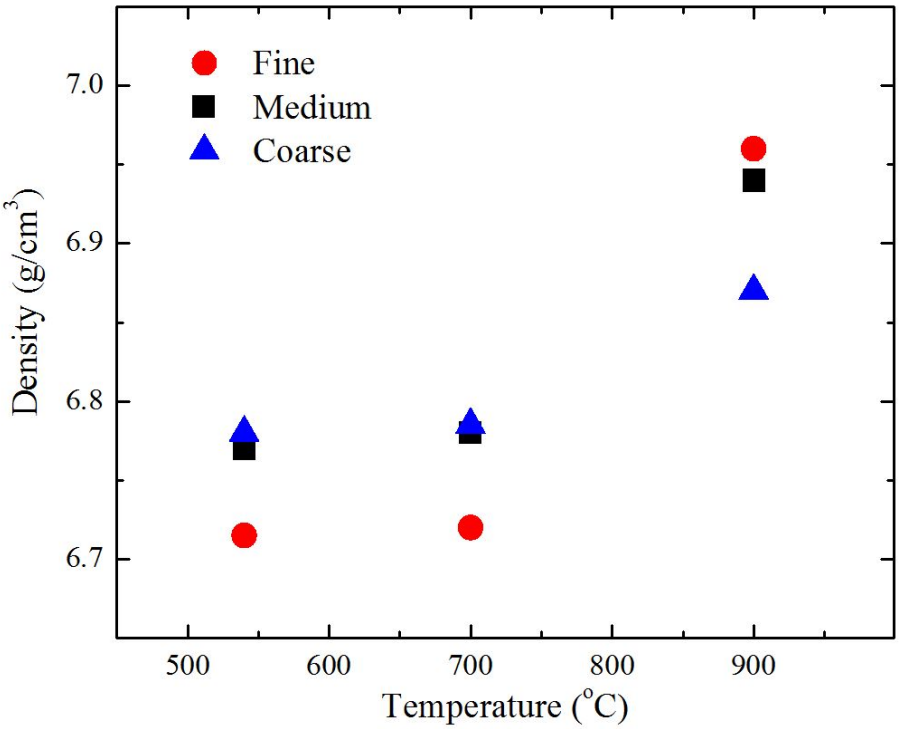


**Figure 5.9:** Density presented for $Fe_3O_4$–coated Fe toroid composites of three particle size classifications, fine (<105 $\mu$m), medium (105 $\mu$m to 250 $\mu$m), and coarse (250 $\mu$m to 425 $\mu$m), cured at 540°C, 700°C, and 900°C.

a linear combination of Gaussian and Lorentzian components [157]. Rough estimates of crystallite size and microstrain are determined from Williamson Hall plots using the integral breadth [104]. In addition, estimates of grain size for the iron–oxide particle coating are found in similar manners. Cross-sectional SEM with EDS images are obtained to determine coating uniformity and thickness as well as Fe coating microstructure. In the second part of this chapter, electron backscatter diffraction (EBSD) patterns are collected from cross-sectioned toroid samples using a FEI XL30 SEM to study the microstructure and crystal orientation. TSL OIM (Orientation imaging microscopy) Analysis$^{TM}$ software by EDAX, Inc. is used to color images and determine grain size, texture, and orientation from OIM scans. Selected area diffraction (SAD) is performed in a JEOL2100 Schottky-assisted FEG transmission electron microscope (TEM) of focused ion beam (FIB) liftouts of the coating–core interface. SAD is used to determine the coating material stoichiometry near the interface of Fe and $Fe_3O_4$ to establish diffusion gradients if present. In addition, EDS maps are obtained to

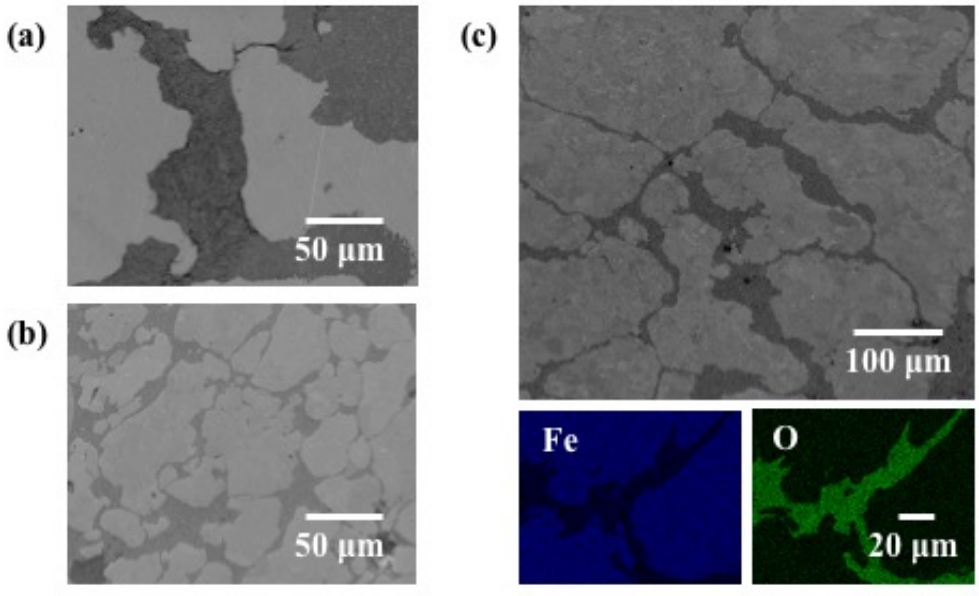


**Figure 5.10:** Cross–section SEM images of $Fe_3O_4$–coated Fe powder of (a) coarse, (b) fine, and (c) medium particle sizes, compacted and cured at 700°C for 1h. Subsequent EDS scans of the medium particle size show Fe (blue) and O (green) elemental content.

illustrate coating regions with higher oxygen concentrations.

**Table 5.2:** XRD peaks for $\alpha$–iron (Fe–BCC), magnetite ($Fe_3O_4$), and wüstite (FeO) with respective crystallographic directions.

| **Compound** | **2$\theta$** | **h k l** | **d** (Å) | **$\Delta$ at 540°C** | **$\Delta$ at 700°C** | **$\Delta$ at 900°C** |
|---|---|---|---|---|---|---|
| Fe | 44.67° | (1 1 0) | 2.027 | 0.001 | 0.033 | 0.032 |
| | 65.02° | (2 0 0) | 1.433 | 0.022 | 0.023 | 0.040 |
| | 82.33° | (2 1 1) | 1.170 | 0.022 | 0.006 | 0.030 |
| $Fe_3O_4$ | 35.42° | (3 1 1) | 2.532 | 0.054 | – | – |
| | 56.94° | (5 1 1) | 1.616 | 0.001 | – | – |
| | 62.52° | (4 0 0) | 1.485 | 0.053 | – | – |
| FeO | 36.04° | (1 1 1) | 2.490 | – | 0.041 | 0.062 |
| | 41.93° | (2 0 0) | 2.153 | – | 0.074 | 0.036 |
| | 60.76° | (2 2 0) | 1.523 | – | 0.196 | 0.270 |

Magnetic B–H loops are measured on toroid samples using a Model SMT 700 Soft Magnetic Hysteresigraph (KJS Associates, IN) following ASTM A773 (DC component) [109] and ASTM A927 (AC component) [110]. AC magnetization curves are performed at a magnetic flux of $B$=1 T from 50 Hz to 5000 Hz. Core loss, magnetic permeability, coercivity, and remanent induction are compared for different particle sizes and curing temperatures in the first part of the this section and for the different grain sizes measured in the second part of this section. Hysteresis loss and eddy current loss

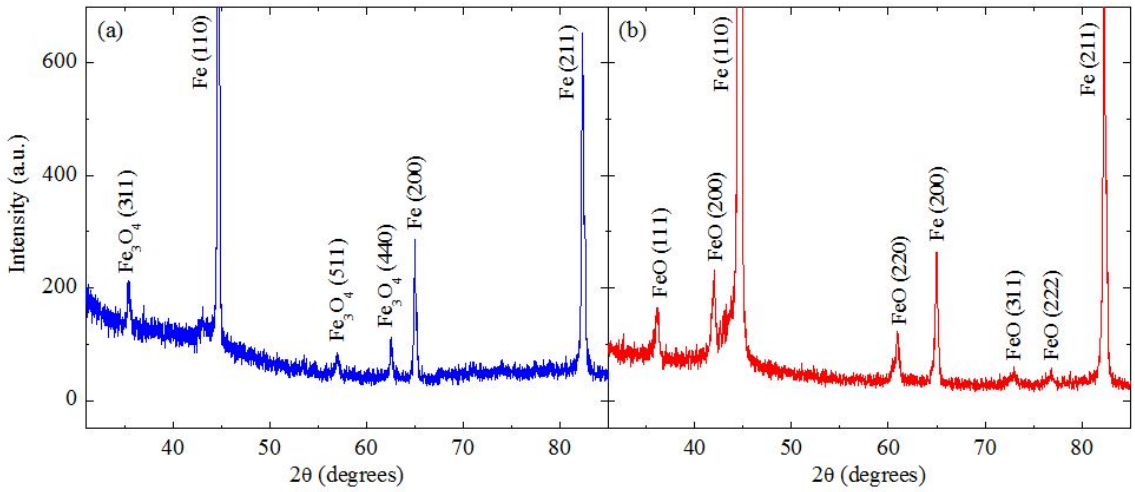


**Figure 5.11:** X-ray diffraction patterns measured on cross-sections of mechanical testing bars, for composites of medium particle sizes cured at (a) 540°C and (b) 700°C. XRD patterns are analyzed with JADE software and found to be BCC–Fe for all samples. The coating material transitions from $Fe_3O_4$ to FeO between 540°C and 700°C as seen from the pattern in (a) to (b), respectively.

contributions are calculated for each section. Saturation magnetization is measured using a vibrating sample magnetometer (VSM) with a maximum field of 5 T at room temperature. Mechanical properties obtained include sintered density and sintered strength, also known as transverse rupture strength (TRS). Nanoindentation measurements are obtained at a depth of 200 nm using a Poisson's ratio of 0.3 to analyze the elastic modulus and hardness of coating and iron regions.

**Table 5.3:** XRD data for $Fe_3O_4$–coated medium size Fe particles after milling, before compacting and curing.

| **2$\theta$** | **Compound** | **h k l** | **d (Å)** | **$\Delta$** |
|---|---|---|---|---|
| 35.37° | $Fe_3O_4$ | (3 1 1) | 2.5356 | 0.052 |
| 43.08° | $Fe_3O_4$ | (4 0 0) | 2.0981 | -0.027 |
| 44.65° | Fe | (1 1 0) | 2.0277 | 0.02 |
| 57.03° | $Fe_3O_4$ | (5 1 1) | 1.6136 | -0.085 |
| 62.61° | $Fe_3O_4$ | (4 4 0) | 1.4825 | -0.095 |
| 65.03° | Fe | (2 0 0) | 1.4331 | -0.004 |
| 82.349° | Fe | (2 1 1) | 1.17 | -0.016 |

## 5.5 Correlation of Particle Size and Cure Temperature on Magnetic Properties

SEM images seen in Figure 5.6 show the three particle size classifications we use in this study. Particles are clearly coated after minimal amounts of milling (<1 h) and show little to no signs of surface cracking. SEM images of coated powder (Fig. 5.7) show the uniformity and coverage of the $Fe_3O_4$ coating on each iron particle for fine and medium Fe particle sizes. Two key features of note are the texture and irregularity of the Fe powder themselves, and the agglomerations of the $Fe_3O_4$ material. The initial irregular particle shape of the Fe powder allows for higher green densities because of mechanical interlocking and reduction of pores. However, when the hard coating material agglomerates into very large regions (>50 $\mu$m), the soft iron particles cannot deform to fill air gaps. Therefore, the density of coated samples (6.9 g·cm$^{-3}$) are much lower than uncoated composites (7.5 g·cm$^{-3}$) for both fine and medium particle sizes (Table 5.1).

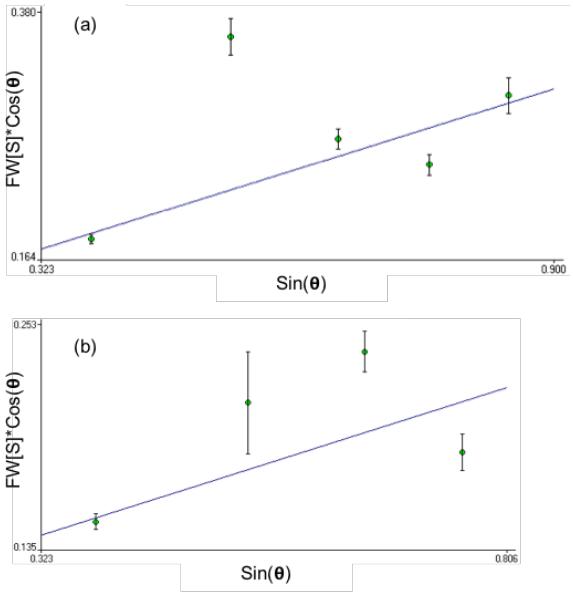


**Figure 5.12:** Williamson–Hall Plots generated for toroid samples cured at (a) 700°C and (b) 900°C.

Our structural characterization of coated and uncoated Fe powder composites pressed at 800 MPa and cured at 700°C indicate density is highly correlated to TRS, maximum magnetic permeability ($\mu_{max}$), and DC coercivity ($H_c$), shown in Table 5.1. Irregularly shaped, uncoated particles allow for improved mechanical interlocking during compaction and more contact points between Fe to improve

strength seen in Figure 5.8. Compaction of soft powder leads to elastic deformation, ultimately reducing porosity and improving density [6]. Curing temperatures of 570–775°C allow for proper stress relief of Fe to improve strength and soft magnetic properties, seen for the high $\mu_{max}$ and low $H_c$ of uncoated samples cured at 700°C. Temperatures above 900°C are used for annealing to increase grain size and subsequently decrease the amount of magnetic domains for improvement of magnetic permeability and saturation. However, the addition of a coating material, especially a hard material such as $Fe_3O_4$, greatly reduces the density and subsequently reduces the mechanical strength and magnetic permeability (Table 5.1). This is attributed to the reduction of metal–on–metal contacts and thus a lack of particle interlocking at the particle boundaries because no plastic deformation occurs during compaction. The brittle $Fe_3O_4$ leads to shearing at the interfaces and thus lower TRS for coated composites. A reduction in TRS is found for larger particle sizes; explained by the inability of particles to plastically deform and thus causing large agglomerated regions of ferrite particles, which easily shear during mechanical testing.

We also compare densities of $Fe_3O_4$–coated Fe toroid samples and observe slightly higher densities for larger particle sizes at temperatures below 900°C, as shown in Figure 5.9. The presented densities are much improved from similar samples compacted at 800 MPa, cured at 165° for 1 h of 90 vol% iron and 10 vol% phenolformaldehyde resin SMCs with a sintered density of ∼6.27 g·cm$^{-3}$ by Kollár et al. [36]. These improved densities are attributed to better particle interlocking achieved during compaction. However, there is a sudden increase in density for finer particles cured at 900°C. This is explained by the reduced coating layer thickness because of finer particles having larger surface to volume ratios, explained previously in Eq. 2.3. Since the coarser Fe particles have lower surface areas to be coated, there are more regions of thick coating material which effectively lowers eddy currents, seen in a cross-sectional SEM image (Figure 5.10a). Therefore, the coating layers are much thinner for finer particles seen in Figure 5.10b, and thus allow for reduced porosity at higher temperatures when the coating material begins to densify. The thinner coating layers are result of more surface area present in smaller particle sizes. The cross-sectional images for all three particle size composites show clear isolation of individual Fe (light grey regions) particles with the $Fe_3O_4$

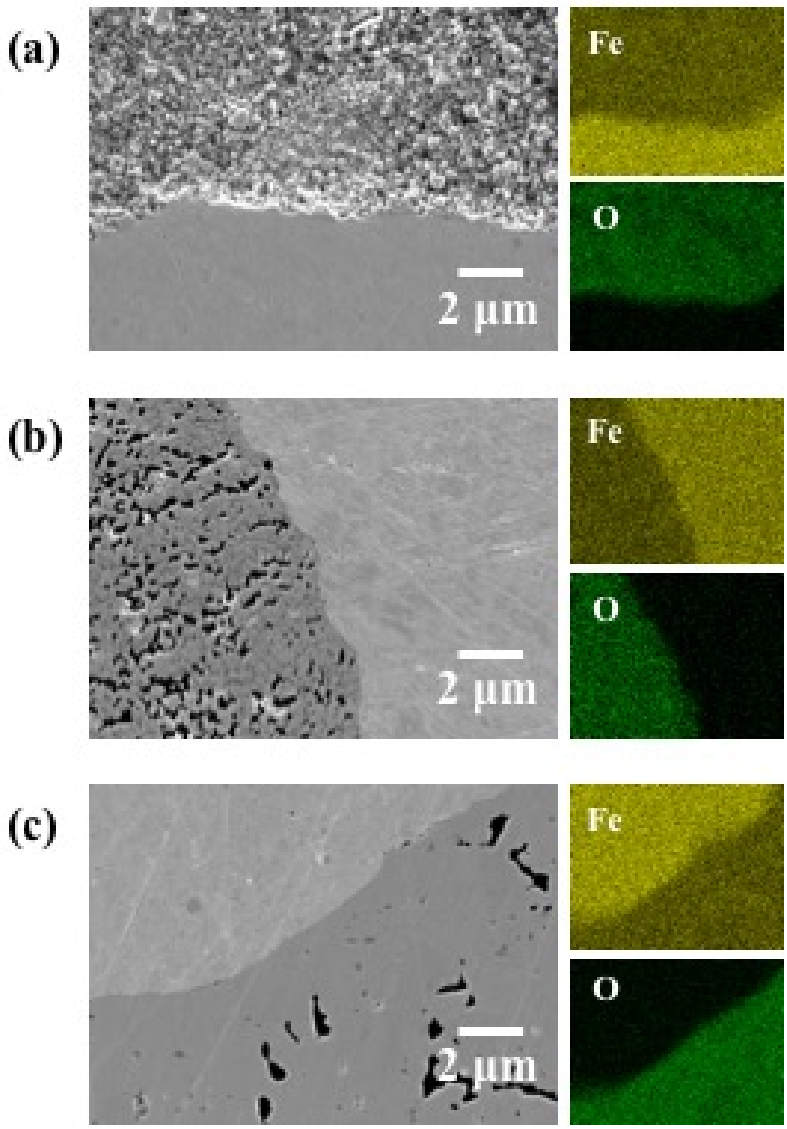


**Figure 5.13:** Cross–section SEM image and EDS scans of $Fe_3O_4$ coating and Fe core interface after (a) 540°C, (b) 700°C, and (c) 900°C cure. EDS scans indicate coating layer is of iron (yellow) and oxygen (green) elements.

(dark grey regions) coating material. However, large agglomerated regions of iron-oxide particles (up to 50 $\mu$m) in coarser Fe composites result in lower density and magnetic permeability, which directly increases hysteresis losses, but also decreases eddy current losses, discussed later on.

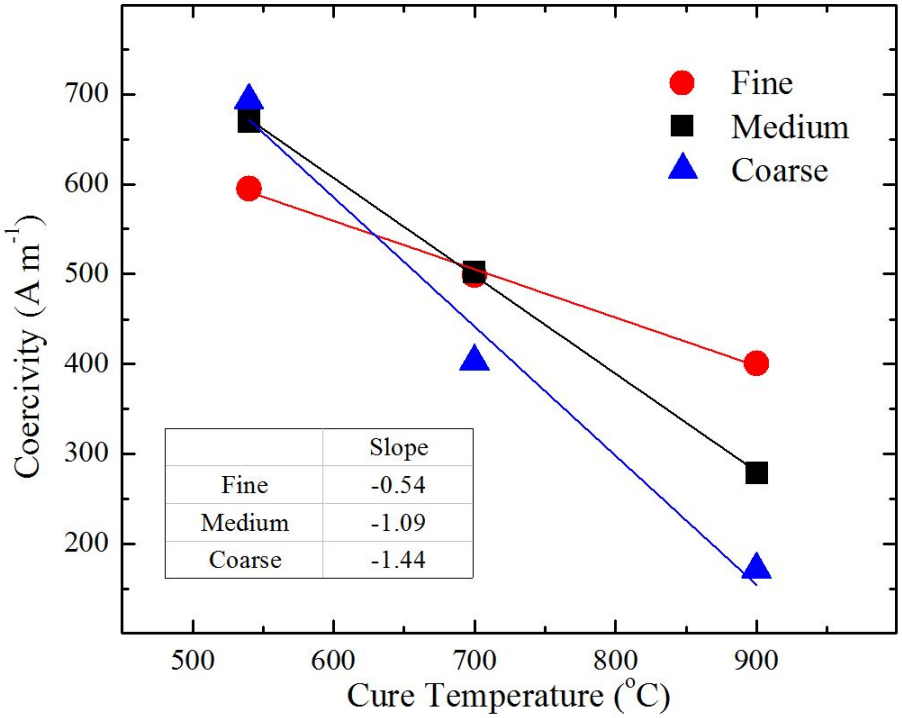


**Figure 5.14:** Coercivity is found to improve (decrease) with increasing curing temperature.

X-ray diffraction patterns indicate all samples have strong $\alpha$–Fe (BCC) phases as seen in Figure 5.11 for medium particle sizes. We observe sharp $Fe_3O_4$ reflections at $2\theta$= 35.42° (311), 56.94° (511), and 62.52° (440) for samples cured at 540°C, seen in Figure 5.11a. Samples cured below 570°C are consistent with iron and magnetite from JADE software analysis using standards (JCPDS Card No: 06-0696 and JCPDS Card No: 019-0629), respectively. XRD patterns of samples cured at or above 700°C show peaks corresponding to FeO (JCPDS Card No: 06-0615) at $2\theta$= 36.04° (111), 41.93° (200), and 60.76° (220), as seen in Figure 5.11b. This is to be expected since the transition temperature of $Fe_3O_4$ to FeO (wüstite) occurs at about 570°C [158]. This phase transition suggests a decrease in resistivity for the semiconductor coating material, wüstite.

Fe peaks are analyzed for crystallite size and microstrain using JADE software and a pseudo–Voigt fitting function to produce Williamson–Hall plots. We find strain decreases with increasing

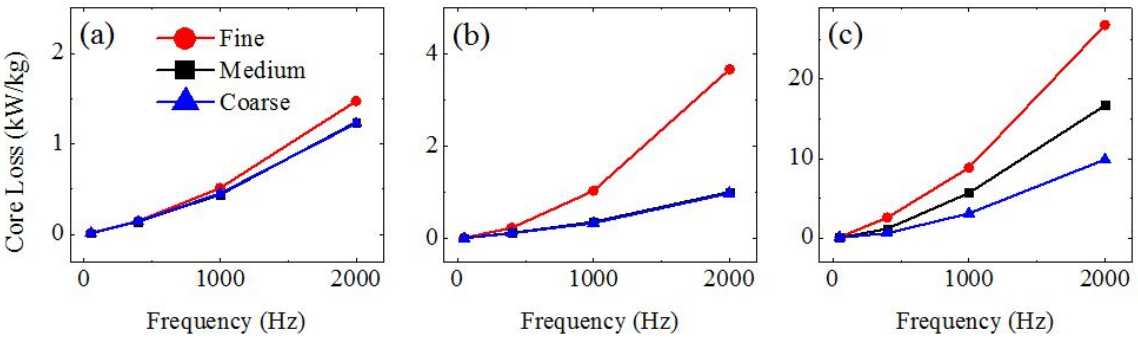


**Figure 5.15:** Core loss comparison for samples cured at (a) 540°C, (b) 700°C, and (c) 900°C at 1T magnetic induction level. Core loss increases as temperature increases, indication of reduced electrical resistivity, which is dissimilar to previous findings of FeO at higher temperatures which would lead to increased resistivity.

temperature as seen in the Williamson–Hall plots for 700°C and 900°C (Fig. 5.12). Strain is reduced from ∼0.105% to ∼0.070%, found by the slope with the increase in temperature. Likewise, crystallite size is found to increase slightly from 825 Åto 873 Å. Unfortunately, the XRD system we use for these measurements is not best suited for samples of such large particle size and crystallite size. In addition to estimating the size and microstrain of Fe through the use of peak broadening analysis, the iron-oxide peaks can also be analyzed for grain size of the coating material. XRD measurements presented in Table 5.3 for the medium particle sizes, confirm the magnetite coating before compaction and heat treatment. Grain size ($D$) analysis of the $Fe_3O_4$ coating using Scherrer's equation [18] for the (311) peak at $2\theta$= 35.42° indicate $D_{fine}$= 24.7 nm and $D_{medium}$= 19.0 nm. These results are attributed to a larger surface to volume ratio causing more agglomerations to occur during milling. Also of importance, our powder does not show a color change to dark reddish brown after being coated with black ferrite, dissimilar to Nakahara et al. [159], where a reddish brown color indicates $Fe_2O_3$ phase. This allows us to compare grain size to electrical resistivity, and in our case eddy current losses.

SEM images and EDS scans seen in Figure 5.13 represent the $Fe_3O_4$ coating and Fe powder interface after compaction and curing at three different temperatures. We observe the coating material to remain in particulate form after a curing temperature of 540°C, before the transition to FeO occurs. These particulates begin to bond together between 540°C and 700°C and create

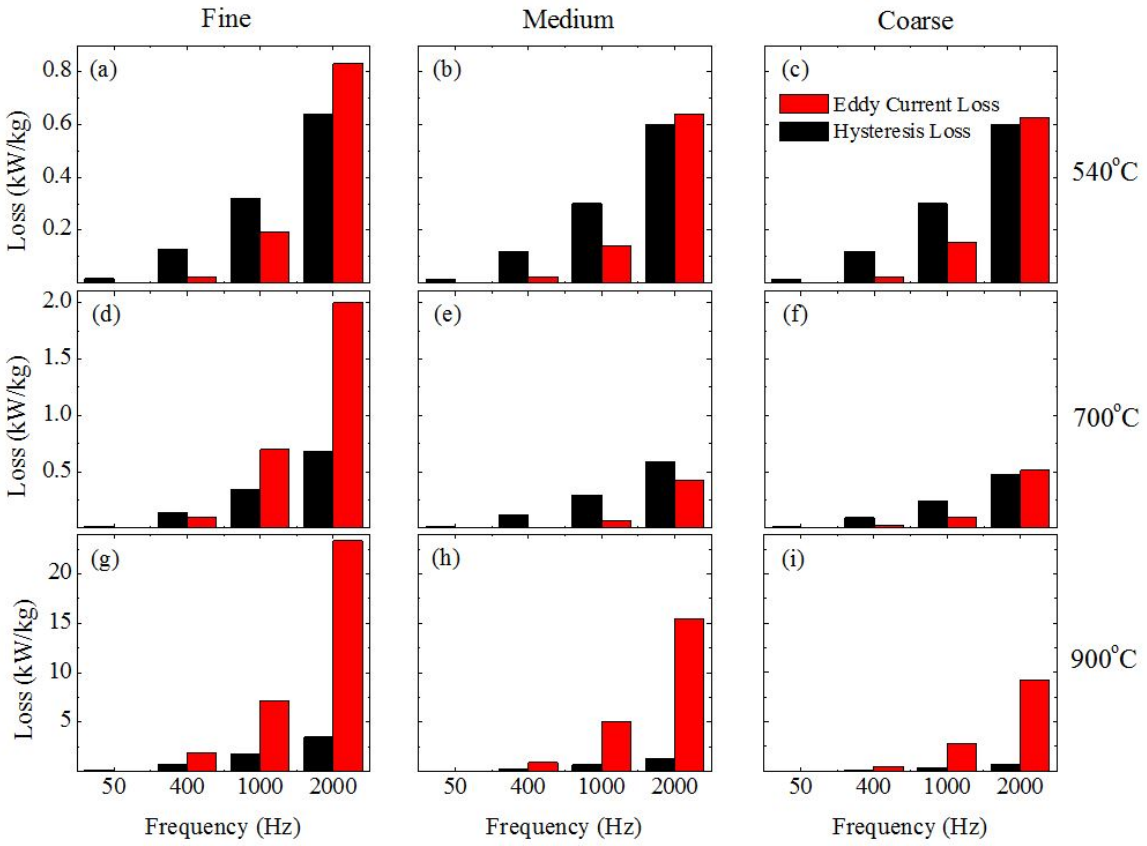


**Figure 5.16:** Hysteresis loss and eddy current loss components of core loss measurements for fine particles (a), (d), and (g), medium particles (b), (e), and (h), and coarse particles (c), (f), and (i), for curing temperatures of 540°C (a), (b), and (c), 700°C (d), (e), and (f), and 900°C (g), (h), and (i) at 1T magnetic induction level. Eddy current loss becomes greater than hysteresis losses at higher frequencies as well as for higher temperature cures. The latter is explained by the formation of more conductive FeO.

**Table 5.4:** Density, DC coercivity ($H_c$), maximum magnetic permeability ($\mu_{max}$), remanent magnetic induction ($B_r$), and hysteresis loss estimation, and AC (at 50 Hz) coercivity ($H_c$), eddy current component percentage, and core loss ($P_{total}$) shown for toroidal samples at increasing temperatures.

| | | **700°C** | **800°C** | **900°C** | **1000°C** |
|---|---|---|---|---|---|
| | Density (g·cm$^{-3}$) | 7.09 | 7.09 | 7.14 | 7.14 |
| DC | $H_c$ (A·m$^{-1}$) | 184 | 220 | 220 | 176 |
| | $\mu_{max}$ | 99 | 119 | 146 | 138 |
| | $B_r$ (G) | 315 | 420 | 782 | 815 |
| | Hysteresis Loss | 58 | 92 | 172 | 143 |
| AC | $H_c$ (A·m$^{-1}$) | 277 | 646 | 1447 | 1650 |
| | Eddy Current Loss (%) | 9.9 | 24 | 54 | 63 |
| | $P_{total}$ (W·kg$^{-1}$) | 6.5 | 15 | 32 | 40.5 |

a well-bonded coating–core interface as seen in Figure 5.13b. A denser coating is observed for curing temperatures exceeding 700°C, as would be expected because of the initial stages of particle sintering creating necking regions and closed pores. EDS scans indicate coating layers are of iron–oxide material for all temperatures. EDS analysis is inconclusive for the dependence of coating layer thickness and amount of $Fe_3O_4$ reduced to Fe with respect to temperature. Further investigation presented in the following section will address these concerns.

The coercivity for all particle sizes is found to decrease with increasing temperature as seen in Figure 5.14. The slopes of the linear fits scale with particle size as seen in the inset of Figure 5.14. The smallest slope corresponds to the least amount of Fe stress relief during curing. We observe a more pronounced decrease in coercivity for larger particle sizes as temperature increases, which is strong indication of proper stress relief of Fe, leading to less regions of nonmagnetic inclusions. However, this greatly affects the overall resistivity of the bulk Fe related to core loss and more specifically eddy current loss.

Core loss measurements, seen in Figure 5.15 illustrate relatively low core loss (<20 W·kg$^{-1}$) at low frequencies. The best core loss results of 12 W·kg$^{-1}$ at 50 Hz, 118 W·kg$^{-1}$ at 400 Hz, and 337 W·kg$^{-1}$ at 1000 Hz were found for $Fe_3O_4$–coated coarse Fe particles compacted at 800 MPa and cured at 700°C for 1 h in 100% $N_2$. Similar values were obtained for medium sized particles, which indicates some particle size overlap that does not greatly affect electrical resistivity in these particular samples. Laxminarayana et al. reported comparable values of 91 W·kg$^{-1}$ at 400 Hz and

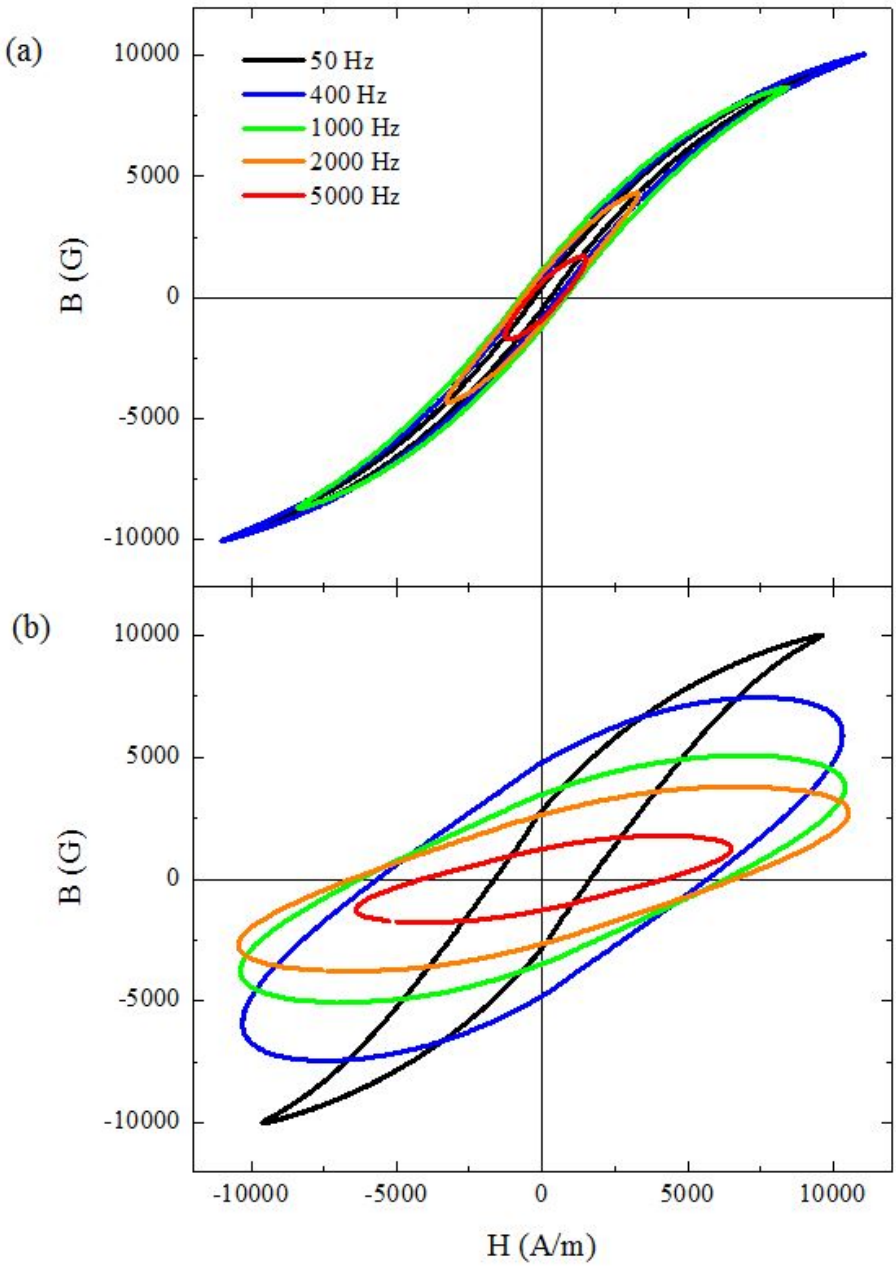


**Figure 5.17:** AC magnetization for (a) 700°C and (b) 1000°C for frequencies of 50 Hz to 5000 Hz.

206 W·kg$^{-1}$ at 1000 Hz for Fe powder composites coated with $Fe_3O_4$ nanoparticles and epoxy resin, compacted at 1050 MPa and cured at 600°C for 2 h [18]. Our research does not use any polymer filler and utilizes a lower compaction pressure of 800 MPa and higher curing temperature of 700°C. We find that less processing steps and higher temperatures are capable of obtaining low core losses for coarser iron particle sizes, ideal for high magnetic permeability requirements. Significant increases in core loss are seen for increasing curing temperature. This implies that the sample becomes less insulative with higher temperatures, explained by the reduction of stress in the Fe and the formation of more conductive ferrous ions ($Fe^{2+}$) in FeO at 570°C, also found via XRD analysis. Density is found to increase with temperature, suggesting higher magnetic saturation and permeability, as well as lower core losses if the coating layers remain intact [46]. The improved density of the large particle sizes suggests higher permeability with lower coercivity and lower overall losses seen in Figure 5.15b. The increase in core loss at 900°C is most notably because of formation of ferrous ions that no longer allow for seclusion of eddy currents within Fe particles.

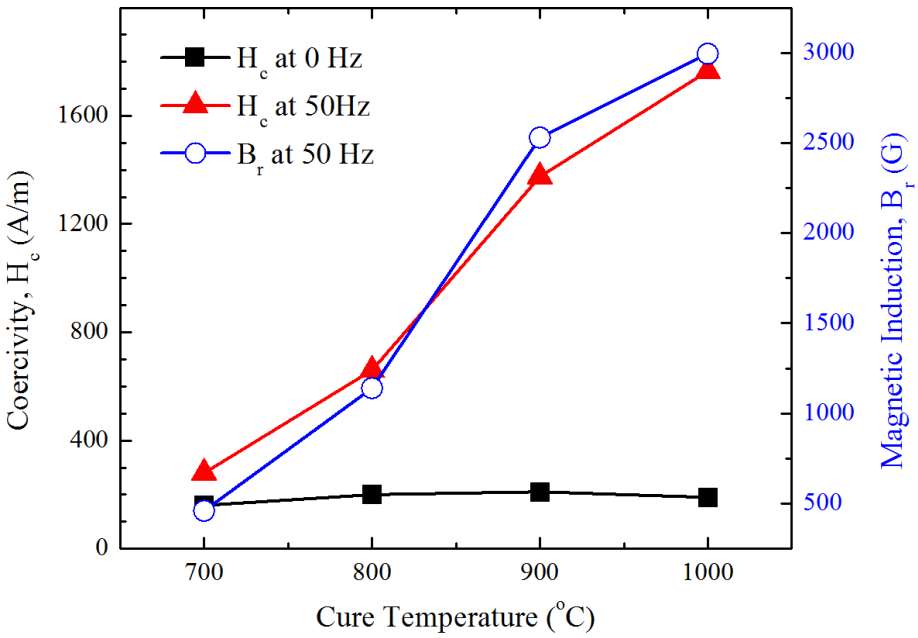


**Figure 5.18:** Coercivity values for DC (0 Hz) and AC (50 Hz) fields (left) and remanent induction (right, blue) with respect to temperature.

To better understand the core loss trends with respect to temperature and particle size, the contributions of eddy current and hysteresis loss are separated, as determined by expanding on Eq.

2.4,

$$P = P_h + P_e = hf + ef^2 \tag{5.1}$$

described previously in Chapter 2. We understand that the following equation is too simplistic for this research study, because of the use of a coating material with low electrical resistivity, however, it is useful for overall component contribution estimations. Since hysteresis losses dominate in the low frequency regime, we assume the contribution of eddy current losses to be negligible for these samples. Therefore, at a frequency of 50 Hz, the total core loss found is estimated to be the base line for hysteresis loss. This is only done for simplicity reasons and will be elaborated on further in the following part of this section. The hysteresis loss and eddy current loss components are then separated via the discussed parameters as shown in Figure 5.16 for the different particle sizes and curing temperatures. Hysteresis loss is assumed to scale linearly with the applied frequency since the material geometry does not change, while the eddy current loss will be highly dependent on resistivity, nominally a higher resistivity will result in lower eddy current losses. We observe that eddy current loss is more dominant than hysteresis losses at lower frequencies for samples cured at 900°C. This is explained by the reduction of impurities and stress in the iron particles leading to a more conductive material, as well as the transition of the coating material from $Fe_3O_4$ to semiconductor FeO. The separation of hysteresis and eddy current losses allows us to confirm that thicker regions of coating found in the coarse particle size classification samples allows for reduced eddy current losses, seen in Figure 5.16i. Therefore, we conclude that larger particles sizes allow for improved densities and reduced eddy current losses because of the particle interlocking during compaction and larger regions of coating based on surface to volume ratios.

The amount of coating (10 wt%) material we use in these samples results in several negative effects on magnetic and mechanical properties. Although a thick insulation layer lowers eddy current losses as seen for coarser particle sizes, the magnetic permeability and density greatly suffers in proportion to the volume fraction of the coating material [159]. In addition, the large amount of coating negatively affects hysteresis loss at low frequencies, therefore already increasing the overall core loss

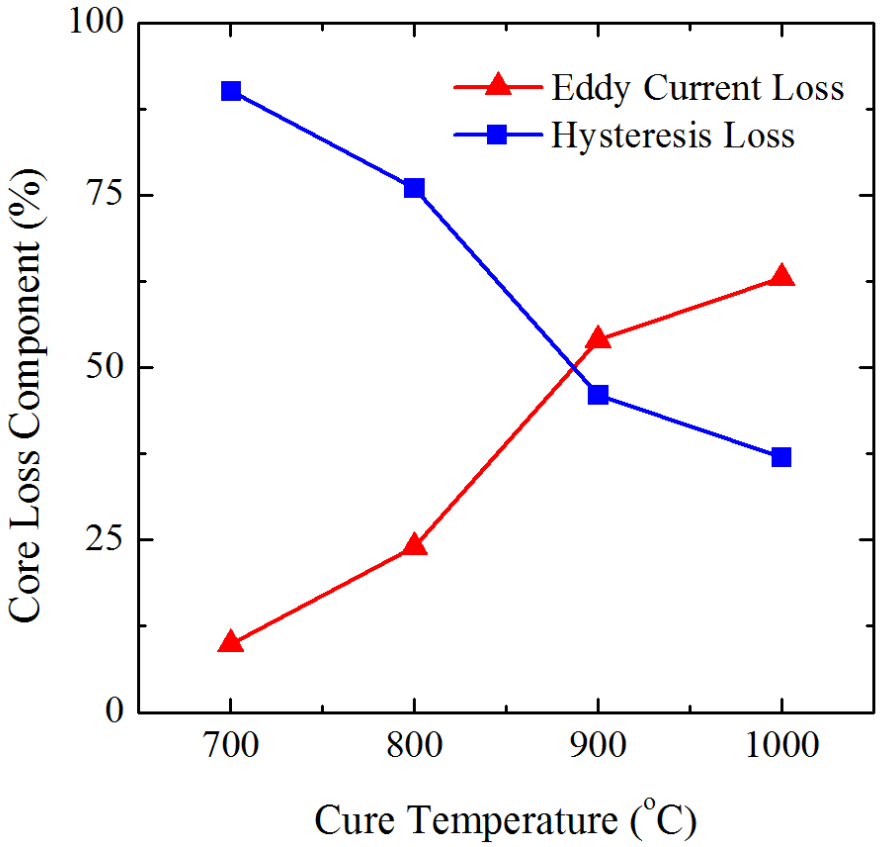


**Figure 5.19:** Separation of eddy current loss and hysteresis loss corresponding to the four temperature studies.

and setting the material up for failure at higher applied frequencies. Comparing our lowest core loss of 118 W·kg$^{-1}$at 400 Hz found for coarse/medium particle sizes cured at 700°C, to that of AncorLam (59 W·kg$^{-1}$ at 400 Hz) [160] and 1P Somaloy 130i (54 W·kg$^{-1}$ at 400 Hz) [57], two commercially available SMC materials, we find that our materials are not a viable solution for improved SMCs. All samples show relatively large regions of brittle iron oxide, which leads to poor TRS and lower densities, which make these materials impossible to be used in an industrial application. The $Fe_3O_4$–Fe material system allows for control of chemical composition and classification of the effect of particle size and cure temperature on magnetic properties. By using the best magnetic properties measured, we can further study the medium/coarse particle sizes to correlate the effect of microstructure to magnetic properties.

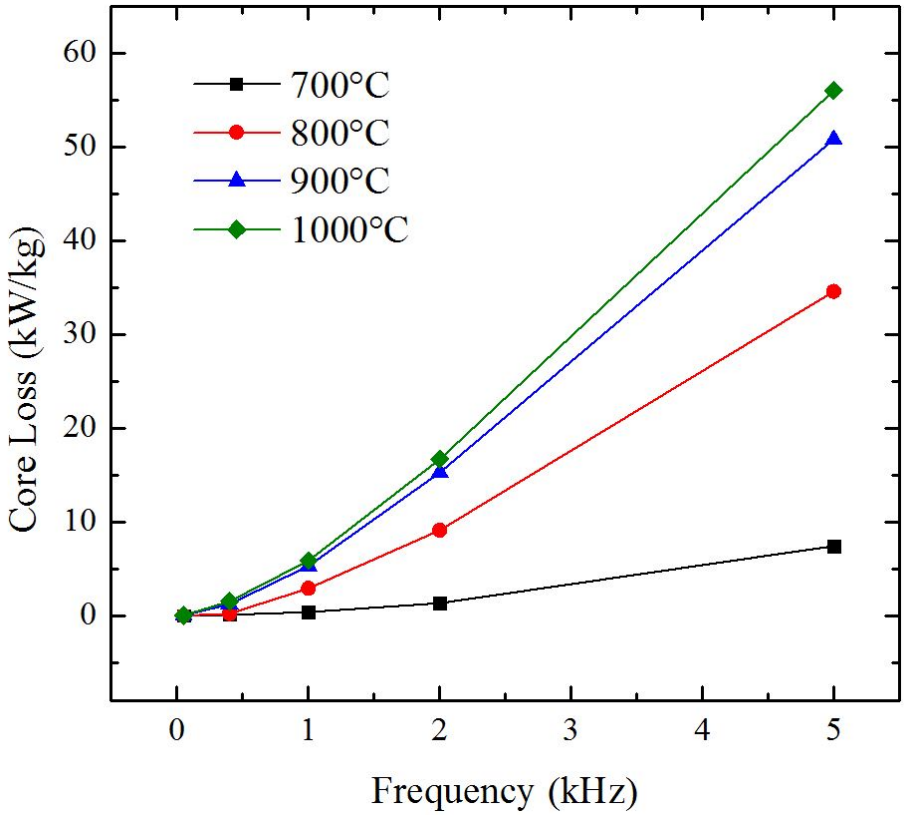


**Figure 5.20:** Core loss dependence on frequency and temperature.

## 5.6 Correlation of Microstructure to Magnetic Properties

### 5.6.1 Magnetic Characterization

Fe powder is coated with 10 wt% $Fe_3O_4$ particles, compacted, cured, and the magnetic properties analyzed to be correlated with microstructural characterization techniques for differing cure temperatures. Density presented in Table 5.4 is found to increase slightly with heat treatment temperature, which is indicative of reduced porosity and shrinkage from particle sintering within the coating. Results for $\mu_{max}$, remanent induction ($B_r$), and $H_c$ using direct current (DC) testing are presented in Table 5.4. DC $\mu_{max}$, $H_c$, and $B_r$ are found to be slightly lower at 1000°C than 700°C. Hysteresis loss contribution is estimated by multiplying $H_c$ and $B_r$ together to semi-quantify the area of the B–H loop. Hysteresis losses are lowered at 1000°C compared to 900°C as to be expected, where Fe should be completely stress relieved and substantial grain growth may occur. Our materials cured at 1000°C have lower coercivity than surface–oxidized Fe powder cured at 600°C reported by Zhao

et al. [96]. Coercivity is related to internal stress and nonmagnetic regions, indicating that all samples have relatively low stress amounts. The 700°C and 1000°C samples have very low coercivities (<185A·m$^{-1}$), however, $\mu$ and $B_r$ are higher at 1000°C. Higher permeability indicates faster magnetizing and demagnetizing and therefore less nonmagnetic inclusions to pin magnetic domain walls. This will be further discussed later as the need for microstructural analysis is evident. Although, assuming more recovery and recrystallization occurs as temperature increases, a reduction in $B_r$ and $H_c$ would result, from less dislocations and stress impeding magnetic structure [161]. However, the effect of a microstructural change in the coating material cannot be ignored. Coating particles will begin to sinter at higher temperatures leading to further densification as well as undesired cracks along Fe particle boundaries from delamination of the brittle coating layers, discussed further later.

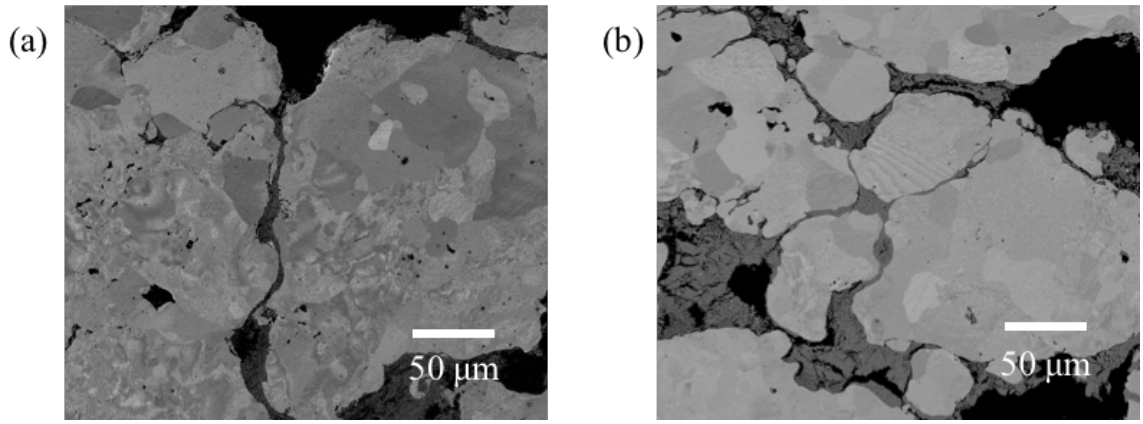


**Figure 5.21:** Backscattered SEM images for 700°C (a) and 900°C (b) cured samples

B–H loops measured with alternating current (AC) conditions are presented in Figure 5.17 and indicate good "soft" magnetic properties for samples cured at 700°C up to a frequency of 1000 Hz, unlike that of the elliptical curves seen for 1000°C at 400 Hz. Lower temperatures will have higher resistivity, which is an intrinsic property and therefore reliant on material crystal structure and porosity. These lower eddy current losses from proper in-particle eddy current seclusions create the well-known "soft" magnetic B-H loop seen in Figure 5.17a. We note the elliptical-shaped loops reduce in area as frequency increases. This is because of instrumental limits set to a maximum current of 10 A. In order to obtain better hysteresis loops at higher frequencies, more current would be needed to drive the magnetic response of the material further. The limitation of the equipment

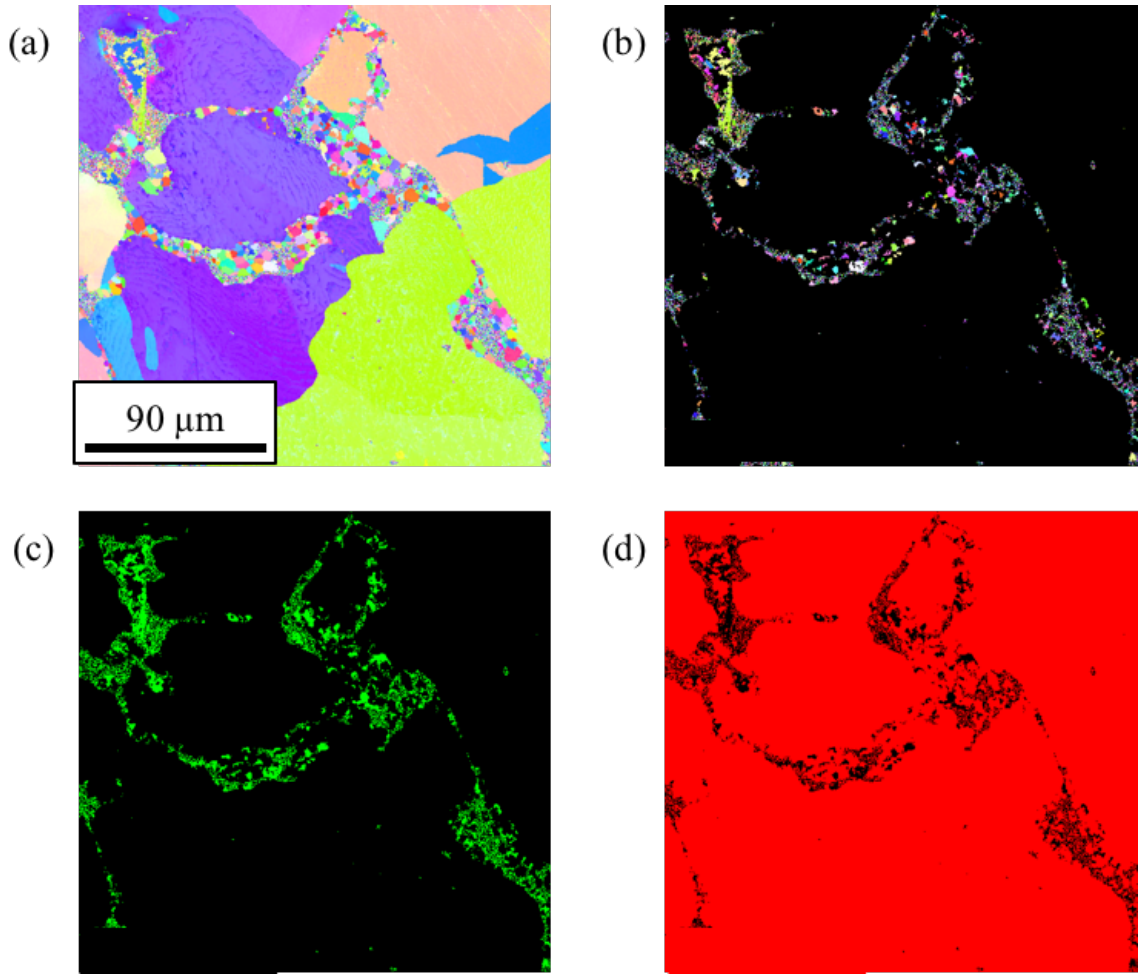


**Figure 5.22:** EBSD inverse pole figure map (a) and subsequent separation of the coating (b) and elemental contributions of O (c) and Fe (d) for 1000°C cured sample.

stops this from occurring, which illustrates the need for a proper study of both eddy current and hysteresis loss with respect to microstructure at lower frequencies, when good loops are acquired.

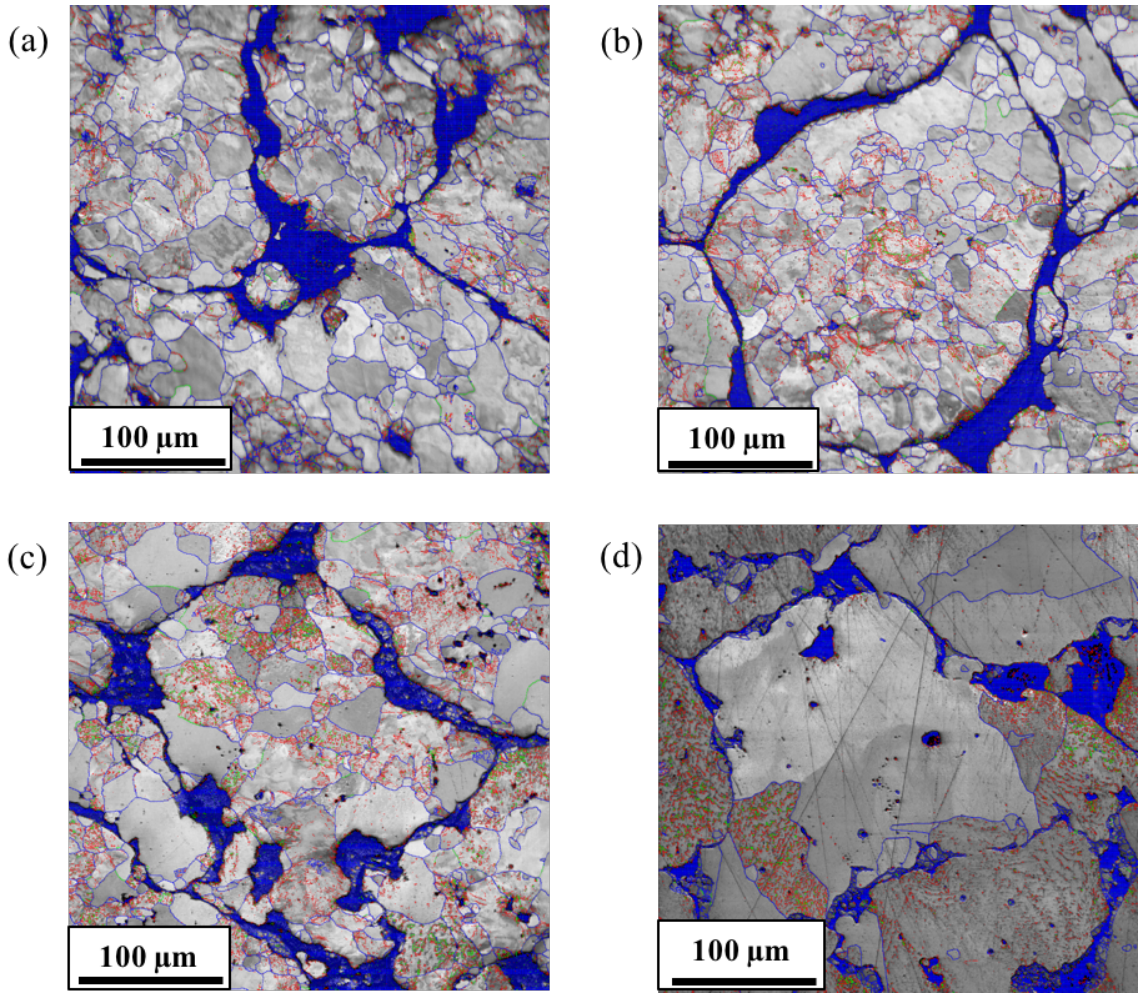


**Figure 5.23:** EBSD images illustrating rotation angles of 2° to 5° (red), 5° to 15° (green), and >15° (blue), for 700°C (a), 800°C (b), 900°C (c), and 1000°C (d).

The relatively low DC coercivity found for all temperatures indicate low hysteresis loss shown in Figure 5.18, even though temperature should drastically increase grain size and thus decrease coercivity. We find magnetic core loss increases with temperature (Table 5.4) and frequency (Fig. 5.20). Although the increase in core loss with respect to frequency was expected, it was not attributed to Eq. 5.1. Eddy current loss, which is dependent on electrical resistivity, dominates core loss at higher frequencies. However, since Fe and $Fe_3O_4$ have very low resistivity, $\rho \sim 10^{-6}$ Ω·cm and $\rho \sim 10^{-2}$ Ω·cm, respectively, these material systems alone or combined will not minimize eddy current

losses and therefore this loss contribution cannot be neglected even at a low frequency of 50 Hz. As shown previously the coating material at 900°C transitioned to FeO, which is nonmagnetic compared to $Fe_3O_4$. This transition from a ferrimagnetic material to a nonmagnetic material, will increase coercivity, hence the reason we see a constant coercivity for all temperatures. Grain growth reduces coercivity, but the coating material composition subsequently increases coercivity, causing a stalemate. We further study and compare coercivity when an alternating current (AC) is applied (Fig. 5.18). Remnant induction and coercivity increase with temperature, indicating an eddy current loss effect. To clarify these findings, we separate the effects of hysteresis and eddy current loss with respect to temperature based on the assumption that DC $H_c$ and $B_r$ are reasonable estimates for hysteresis loss and measurement of the area within the B–H loop. Subsequently, the eddy current loss component can be estimated by the difference between the hysteresis loss component calculated and AC (50 Hz) coercivity presented in Figure 5.19 and Table 5.4. This difference would be neglected if the coating material was more resistive and AC coercivity was minimized or more similar to DC $H_c$. This technique is different and more accurate than the previously used Eq. 5.1 for the particle size study neglecting eddy current loss at low frequencies. The lower eddy current losses of 9.9% at 700°C are result of a higher electrical resistivity from the coating materials porosity and microstructure. At higher temperatures, eddy current loss clearly becomes a dominant factor in core loss, which needs more exploration into the microstructural features of these materials systems for explanation.

Alloying additions of Si or using more resistive coatings would allow for isolation of eddy currents by increasing overall resistivity; however, the magnetic flux density will be greatly reduced with any nonmagnetic inclusions. Often the formation of precipitate phases at higher heat treatment temperatures will deteriorate magnetic properties, such as B or Si additions [90]. In order to maintain high magnetic performance in our SMCs, nonmagnetic contributions were minimized by using high purity Fe powder and ferrimagnetic coating layers. As previously shown, a semiconductor material should not be used for insulative coating layers to confine eddy currents and improve electrical resistivity. However, with this being said, learning from the microstructural components of these material systems are extremely important for soft magnetic composite development as a field. For

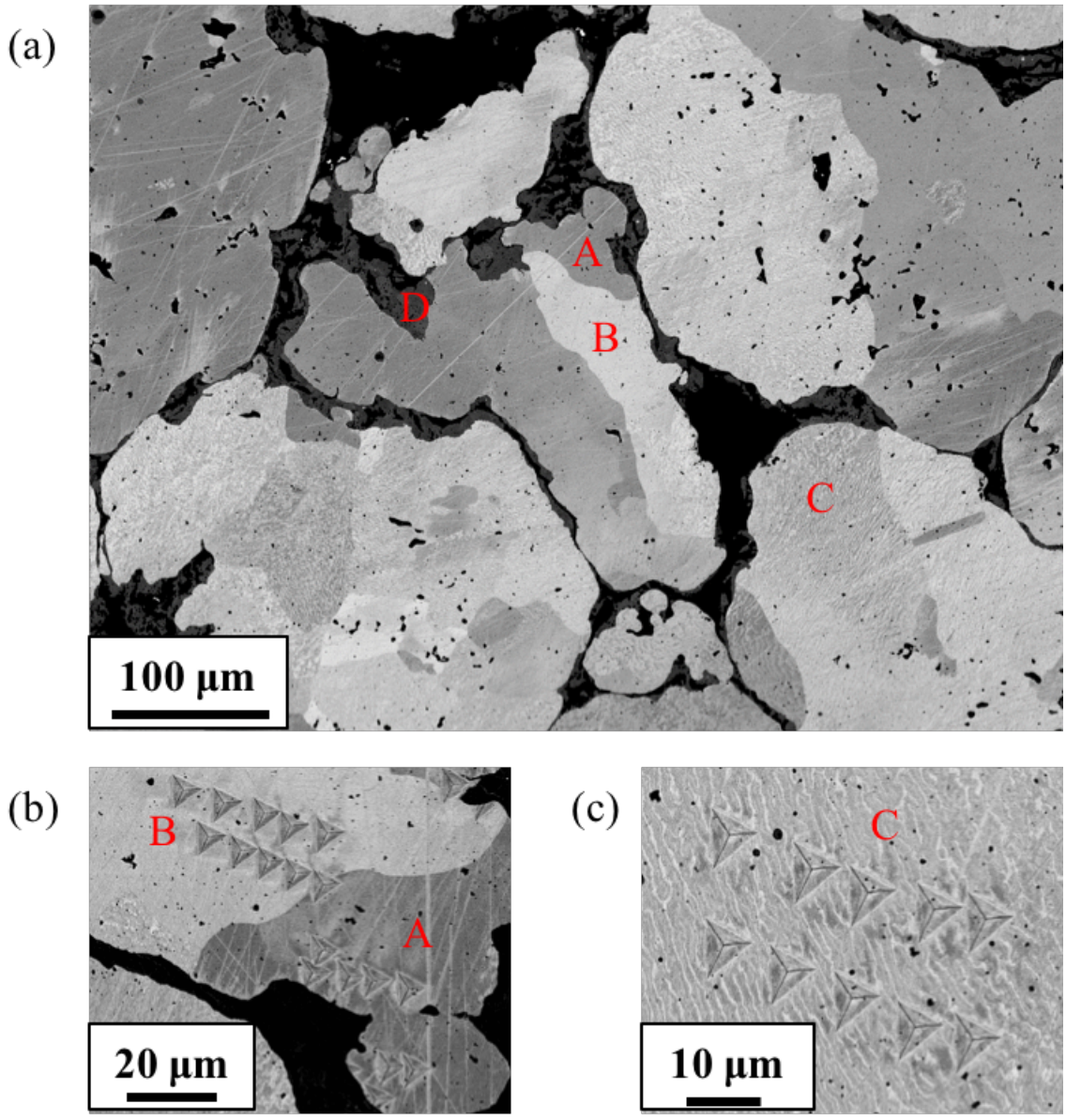


**Figure 5.24:** SEM image (a) corresponding to nanoindentation results in Table 5.5 for 1000°C cured sample, with zoomed in view of region A and B (b) and region C (c).

this research, further microstructural investigation into these SMCs is required to confirm that an increase in eddy current loss is due to crystal structure, porosity, or inter-particle eddy current paths and will now be discussed. Lastly, VSM measurements were obtained, but will be discussed in the following part of this section, to relate to microstructural analysis.

**Table 5.5:** Elastic modulus and hardness values corresponding to regions illustrated in Figure 5.24 for 1000°C cured sample.

| **Material** | **Region** | **Modulus** (GPa) | **Hardness** |
|---|---|---|---|
| Fe | A | 214 | 2.12 |
| | B | 223 | 2.18 |
| | C | 222 | 2.25 |
| $Fe_3O_4$ | D | 123 | 6.55 |

### 5.6.2 Microstructural Characterization

Proper iron stress relief, which occurs between 570–775°C is necessary to improve magnetic permeability and minimize hysteresis losses by reducing nonmagnetic boundaries in SMCs [156]. Pushing the limit of this temperature range will further improve SMC developments. For this material system, the coating material may become more conductive at higher temperatures, because grain growth leads to reduced defects. We see in Figure 5.21 that samples cured at 700°C have much more remanent deformation and stress from compaction as compared to samples cured at 900°C. BSE images not only allow us to determine location of different materials, nominally the coating and core via different shades of gray, but also grain structure and size. Using EBSD we can determine the exact grain size for each sample to be used for understanding of magnetic characterization. A clear separation of oxygen and iron content for a sample cured at 1000°C is seen in Figure 5.22c–d. By allowing the TSL OIM software to pinpoint solely $Fe_3O_4$ crystals, we can illustrate the formation of grains in the coating material, indication of sintering of particles at the highest temperature of 1000°C. We previously showed the benefit of a higher curing temperature of 1000°C to have decreased coercivity and minimally affected permeability. We now discuss how these magnetic properties correlate to the materials microstructural features.

EBSD images showing high angle grain boundaries (blue) with rotation angles of >15° and low angle grain boundaries in green (5° to 15°) and red (2° to 5°) are seen in Figure 5.23. High

**Table 5.6:** Elastic modulus and hardness values corresponding to the four temperatures studied for Fe and $Fe_3O_4$ regions.

| **Temperature** | **Material** | **Modulus** (GPa) | **Hardness** |
|---|---|---|---|
| 700°C | Fe | 217 | 2.38 |
| 800°C | Fe | 209 | 2.78 |
| 800°C | $Fe_3O_4$ | 65 | 3.05 |
| 900°C | Fe | 220 | 2.31 |
| 1000°C | Fe | 220 | 2.20 |
| 1000°C | $Fe_3O_4$ | 123 | 6.55 |

concentrations of low angle grain boundaries are seen in several grains. These regions of high stress in Fe cores lead to higher hardness values measured from nanoindentation, as expected. Elastic modulus and hardness values for four regions illustrated in Figure 5.24a are presented in Table 5.5. There is a slight increase in hardness for region C of Fe, which clearly has large amounts of low angle grain boundaries as similarly shown in Figure 5.23d. Moduli does not change significantly for Fe regions, which allows us to determine a significant change for the coating region D. Nanoindentation results confirm that $Fe_3O_4$ is a hard, brittle material, and at elevated temperatures the coating begins to densify and grain growth occurs. We compare nanoindentation results for all four temperature studies in Table 5.6. Once again, elastic moduli and hardness values for Fe regions are relatively constant for all temperatures. The more important parameters to note are the elastic moduli and hardness for the coating material regions. Both properties nearly double from 800°C to 1000°C for $Fe_3O_4$ regions. This is attributed to the densification of the coating particles creating less particle boundaries and the reduction of a porous network within the coating layers.

**Table 5.7:** Average grain size, magnetization, and grain orientation spread (GOS) values for each heat treatment.

| | **700°C** | **800°C** | **900°C** | **1000°C** |
|---|---|---|---|---|
| Average grain size ($\mu$m) | 30 | 30 | 40 | 100 |
| Magnetization (emu·g$^{-1}$) | 217 | 207 | 201 | 204 |
| Average GOS values | 3.44 | 2.87 | 3.32 | 1.30 |

EBSD maps using grain orientation spread (GOS) analysis illustrate the grain size, grain orientation, and in-grain strain, which is a measure of the stress relief of the Fe core powder, of cross–sectioned toroid samples for all four temperature treatments (Fig. 5.25). GOS analysis method measures the deviation in orientation between each point within a single grain and averages the

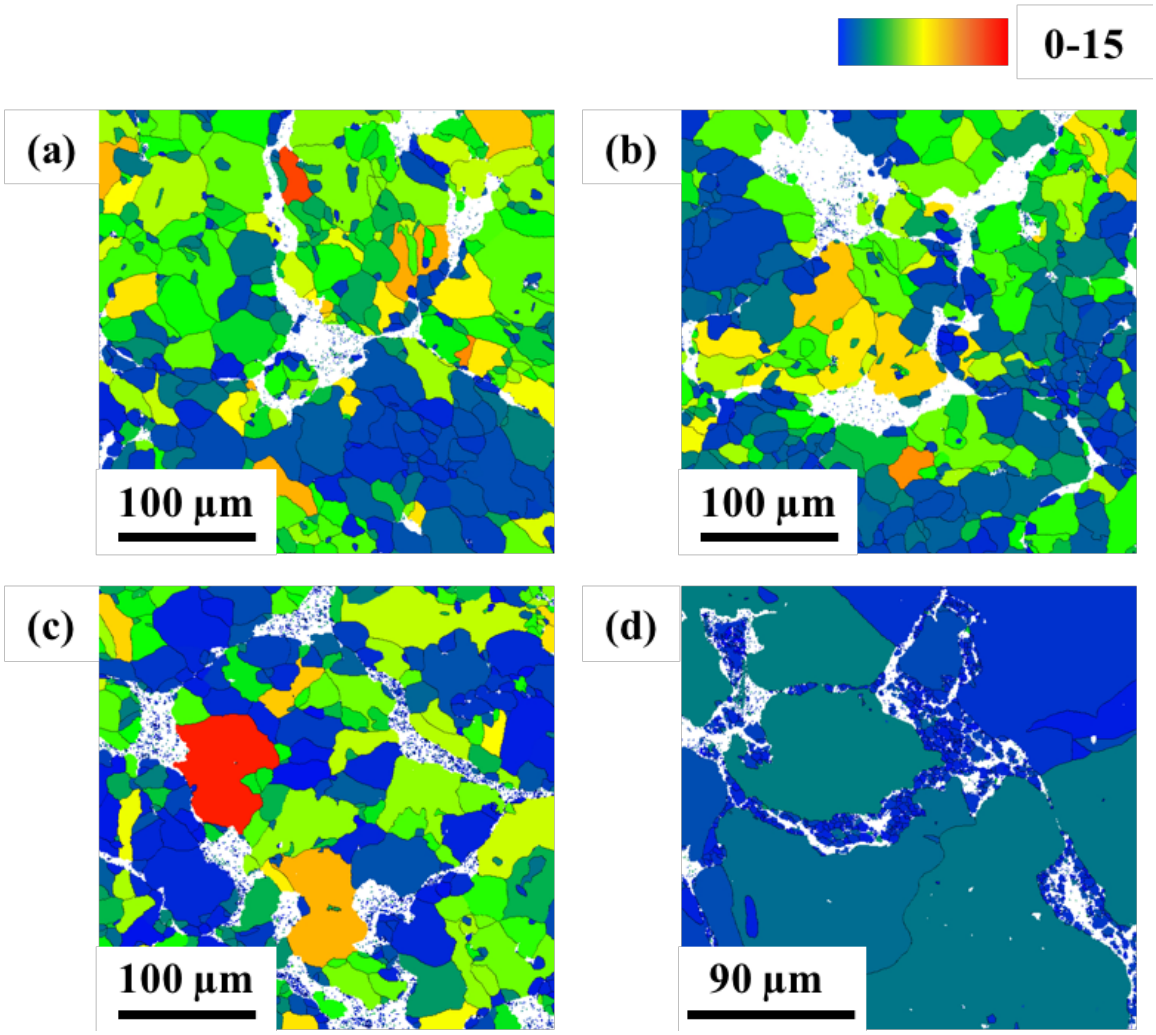


**Figure 5.25:** EBSD maps using OIM analysis and grain orientation spread (GOS) of (a) 700°C, (b) 800°C, (c) 900°C, and (d) 1000°C, where white represents the coating or pores.

overall orientation per grain. The GOS values presented are the average of all grains present in the image. We relate the local misorientation in each grain to the materials plastic strain brought on by compaction and reduced by heat treatment. The initial GOS value at 700°C is 3.44, indicating higher misorientation within grains throughout the specimen. Stress relieving temperatures should reduce the grain orientation spread by recrystallizing the grains and reducing internal strain or misorientation. An increase in GOS is seen at 900°C compared to 800°C, but is explained by the two grains colored in red and orange. These two grains have high misorientation averages and therefore high plastic strain, which skews the overall GOS value. These grains have more strain because of the built-up energy associated with them and their inability to recrystallize at the designated temperature. We then present a large decrease in GOS at 1000°C of 1.30, indicating proper recrystallization and grain growth. The least amount of misorientation is desired for better magnetic properties, making it easier for magnetic domains to move and magnetic spins to rotate to realign with the applied field.

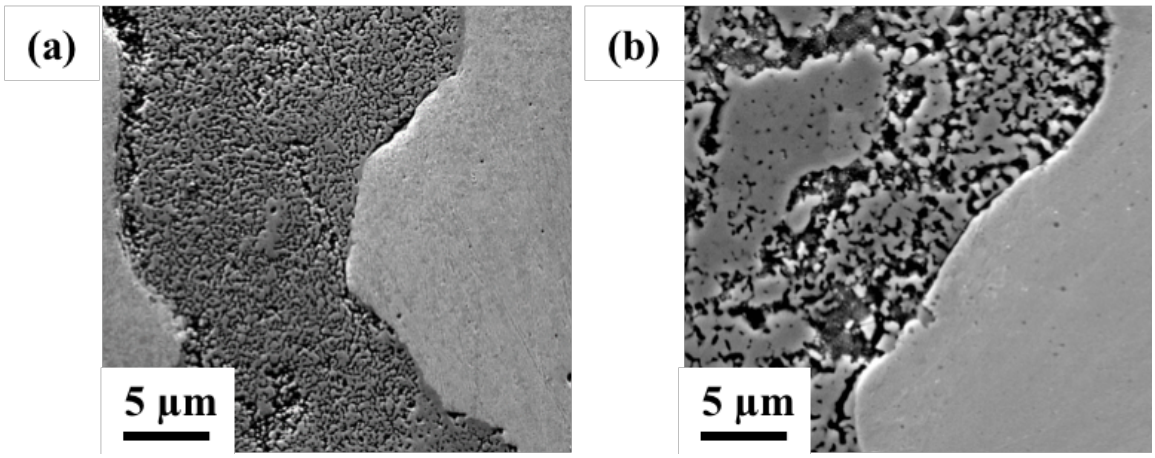


**Figure 5.26:** SEM image of coating material (dark) and Fe core (light) for (a) 700°C and (b) 900°C.

The average grain size more than triples from ∼30 $\mu$m to ∼100 $\mu$m from 700°C to 1000°C with the first signs of grain growth occurring at 900°C shown in Table 5.7. Lower temperatures are within the stress relieving range of Fe and therefore should not allow for grain growth, but rather recovery and recrystallization. Minimizing dislocations and nonmagnetic regions in SMCs will help to insure high magnetic permeability as compared to green parts, with further increases

in permeability being obtained via higher compaction pressures or longer times and higher heat treatment temperatures [7, 89]. For example, increasing temperature from 700°C to 900°C increased $\mu$ from 99 to 146, respectively. However, as shown in this work the effect of the coating is also a large factor on magnetic properties. Grain growth occurs in the core powder and coating regions, however, the grain growth in the coating material shown in Figure 5.26, increases pore size, but not necessarily total porosity (Table 5.8). Relative density is calculated assuming the theoretical density of 10 wt% $Fe_3O_4$–Fe is 7.53 g·cm$^{-3}$, and the remaining volume is porosity, neglecting additional contamination from processing. All samples have high relative density and therefore fairly low porosity levels, indicating warm compaction with minimal lubricant additions is feasible for these material systems. We see minimal reduction in magnetization (Table 5.7) indicating good overall magnetic performance for this material system, as to be expected since magnetite as a very good magnetization (∼92 emu·g$^{-1}$). Following a rule of mixtures, for 10 wt% $Fe_3O_4$–Fe the theoretical magnetization should be 207 emu·g$^{-1}$, where the experimental results are fairly close. PM techniques allowing for low porosity levels are ideal compared to expensive, less conventional processes.

**Table 5.8:** Density, relative density, and porosity content for four temperature treatments.

| | **Density** (g·cm$^{-3}$) | **Relative Density**$^*$ (%) | **Porosity** (%) |
|---|---|---|---|
| 700°C | 7.09 | 94.2% | 5.8% |
| 800°C | 7.09 | 94.2% | 5.8% |
| 900°C | 7.14 | 94.8% | 5.2% |
| 1000°C | 7.14 | 94.8% | 5.2% |

$^*$ Relative density calculated based on the theoretical density of 10 wt% $Fe_3O_4$–Fe composite = 7.53 g·cm$^{-3}$.

**Table 5.9:** Volume percentages from image analysis for four temperature treatments.

| | **Fe** | **$Fe_3O_4$** | **Porosity** |
|---|---|---|---|
| 700°C | 81.8% | 11.2% | 3.8% |
| 800°C | 86.4% | 5.2% | 8.1% |
| 900°C | 82.4% | 11.8% | 5.6% |
| 1000°C | 83.4% | 4.7% | 10.5% |

The large grain size, as a result of grain growth, seen at 1000°C explains the large decrease in hysteresis loss related to the reduction of grain boundary density, which will result in a lower coercivity. The large change in AC coercivity for minimal grain growth between 800°C and 900°C is credited to recovery and recrystallization, minimizing internal stress of grains. We see a small

change in AC $H_c$ for substantial grain growth between 900°C and 1000°C, not easily explainable by microstructural characterization of Fe powder. Therefore the importance of the oxide coating layer microstructure becomes more pronounced to determine affect on eddy current losses.

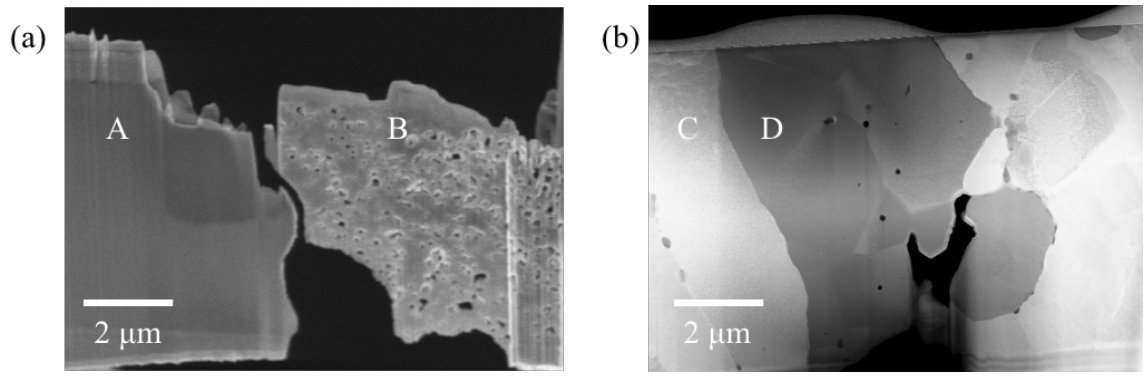


**Figure 5.27:** TEM images of FIB liftouts for (a) 700°C and (b) 1000°C. Regions A and C are the core powder, and regions B and D are the coating material.

Our initial coating material is in particulate form, seen in Figure 5.26a, after milling, compacting, and curing at 700°C. The coating particles begin to sinter together at this low temperature and form a network of pores, with a multi-domain magnetic structure, leading to low coercivity. Further increasing temperature allows for additional sintering to occur between coating particles seen in Figure 5.26b, and minimizes the large internal pore network by creating more localized pockets of air. Figure 5.22 showed the 1000°C sample where the coating material begins to sinter and develop grains by eliminating the particle boundaries. In addition, we see sintering between Fe particles leading to inter-particle eddy current paths that increase core loss. Likewise, results in Table 5.8 show the amount of porosity in all samples is low and remains constant, based on density calculations. Similarly using image analysis for coating volume percentage as the previous chapter showed, the contributions of pores and coating are separated and presented in Table 5.9. We find a large range of values for porosity and coating, indicating image analysis for determining exact porosity is not completely accurate. PM techniques of mounting and polishing leads to particles being removed when more than half of the largest diameter region is polished away, therefore leaving regions of pores where a particle once occupied leading to inaccurate measurements. For this reason, porosity values based on density are more accurate and the minimal change in pore volume illustrates the

need for dense parts before heat treatment, since further significant densification will not occur in the heating stage. Our porosity values 10 wt% $Fe_3O_4$ coating layers are much lower than those presented for Fe–Si powder coated in $MnZnFe_2O_4$ with similar ferrite amounts, >15% porosity for 11 vol% MnZn–ferrite [27].

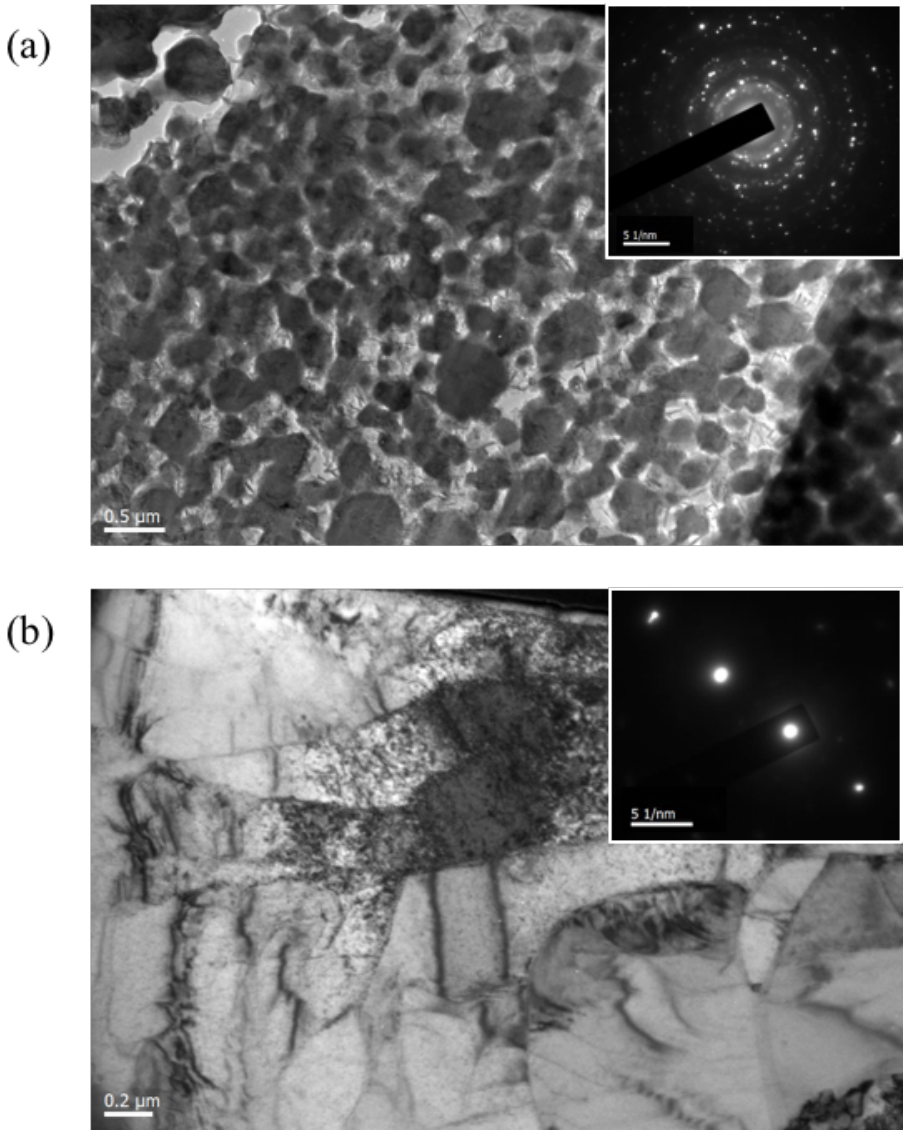


**Figure 5.28:** TEM images of 700°C sample for (a) coating and (b) core powder. The inset images correspond to the selected area diffraction pattern.

Our coating material will have lower coercivity when fewer boundaries are present, nominally at 1000°C, but higher remanent induction. The higher $B_r$ can be explained by a higher thermal expansion coefficient of $Fe_3O_4$ than Fe, causing ferrite coating layers to expand at higher temper-

atures and cause more stress to Fe powder, therefore increasing hysteresis losses. The increase in remanence will lead to more area enclosed by the B–H loop and therefore higher hysteresis losses. The previously mentioned current limitation of the magnetic testing equipment will create more elliptical-shaped loops, where the maximum magnetic response in the test is not the materials true maximum magnetic response. We relate eddy current effects to the coating material and its microstructure. The electrical conductivity of magnetite will also increase with temperature because of grain growth allowing for recovery of structural defects like vacancies. This explains the drastic increase in eddy current loss at higher temperatures. The coating composition would also effect the differences in resistivity greatly. Previous research confirmed FeO coating formation after 570°C [96]. This indicates all samples for this study have FeO coating composition, which is more conductive than $Fe_3O_4$. We perform TEM analysis to further investigate the coating material at a smaller length scale.

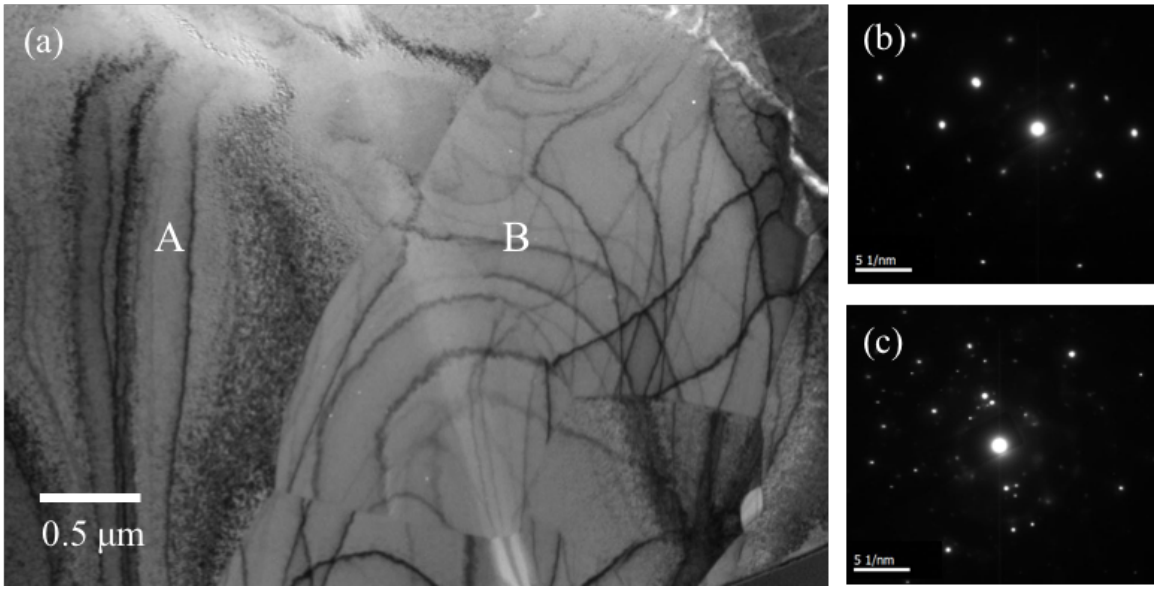


**Figure 5.29:** TEM image of 1000°C (a) with SAD pattern of region A (b) as core powder and region B (c) as coating material.

TEM images of a FIB liftout for 700°C and 1000°C are shown in Figure 5.27, illustrating the difference in pore networks discussed previously at a higher magnification. Selected area diffraction (SAD) patterns are collected using TEM to account for the crystallographic differences between the coating material compared to the core powder. Figure 5.28 and 5.29 show TEM images with

**Table 5.10:** Diffraction analysis of core and coating materials using DiffTools on SAD patterns from TEM on 1000°C sample.

| Region | d-spacing (Å) | Composition | h k l | Error (%) |
|---|---|---|---|---|
| Core | 2.018 | Fe | 110 | 0.4 |
| | 1.429 | Fe | 200 | 0.3 |
| | 1.011 | Fe | 220 | 0.2 |
| Coating | 2.979 | $Fe_3O_4$ | 220 | 0.5 |
| | 2.550 | $Fe_3O_4$ | 311 | 0.9 |
| | 2.076 | $Fe_3O_4$ | 400 | 0.9 |
| | 1.496 | $Fe_3O_4$ | 440 | 1.0 |

respective SAD patterns for the coating and core powder regions, for 700°C and 100°C, respectively. We see an amorphous and polycrystalline coating structure at 700°C from SAD and a more recrystallized and less amorphous coating material at 1000°C. The diffraction patterns are analyzed using DiffTools described by D.R.G. Mitchell [162] and the results are presented in Table 5.10 for the 1000°C sample. Analyzing the 700°C sample is difficult because of amorphous rings not being completely clear. We confirm $\alpha$-Fe to be the sole element in the core regions illustrating minimal oxidation to the Fe powder, shown in Figure 5.30 for EDS maps. We see a clean grain boundary in the coating material in Figure 5.30c, indicating no additional oxygen concentration present. The coating material is determined to be polycrystalline $Fe_3O_4$ for all samples. Previously, we discussed the coating material at temperatures above 570°C to be FeO [96]. The discrepancy in the coating composition lies in the methods of characterization. XRD probes well below the surface of a material, to at least 20 $\mu$m, allowing for more of the coating region to be analyzed that has not interacted directly with air and therefore has not had the opportunity to oxidize. TEM requires a very thin (less than 100 nm) sample, which allows for the coating to oxidize rather quickly for this material system, and since FeO is unstable at room temperature, it will transition back to $Fe_3O_4$ [153]. For this reason, we conclude that the coating material is in fact FeO at elevated temperatures, and is still consistent throughout the studies, therefore not affecting core loss values. We determine that coating materials that have interconnected pores and structural defects allow for lower eddy current losses. Likewise, significant grain growth at 1000°C reduces DC $H_c$, but stress from expansion of ferrite layers increases DC $B_r$. Therefore, hysteresis losses are not completely minimized at higher

temperatures for these material systems. Coating layers that are maintained and more insulative at higher temperatures are promising for the future of SMCs and lead into research of more resistive ferrite materials.

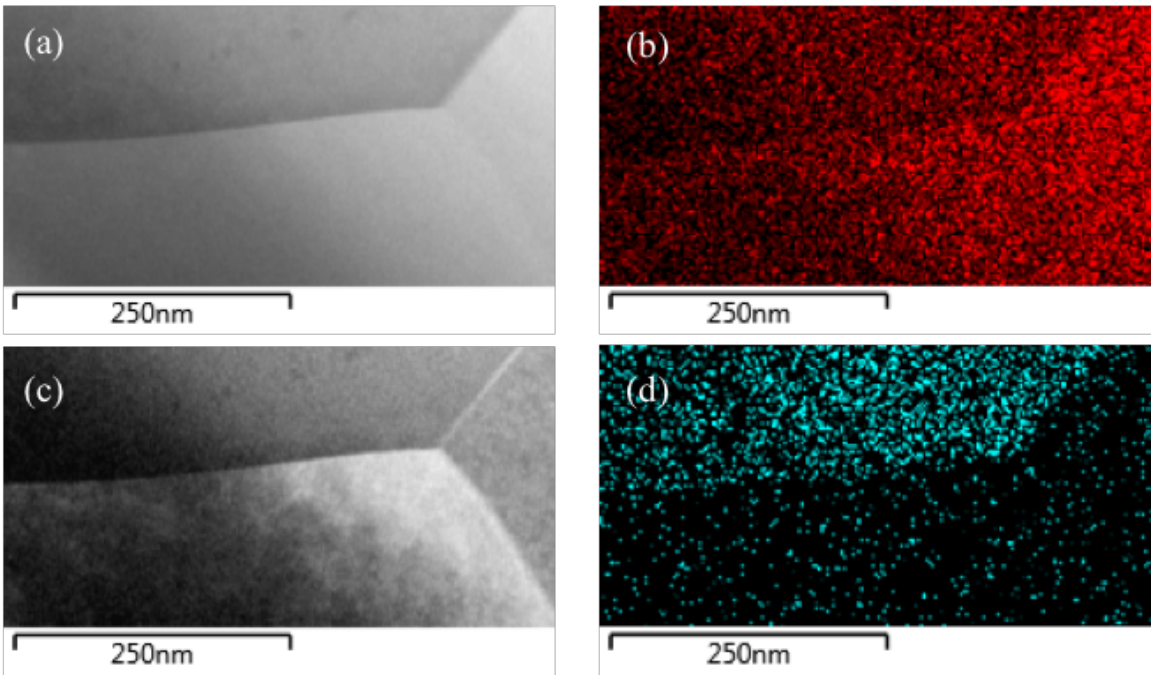


**Figure 5.30:** TEM image of 1000°C using (a) bright field and (c) dark field, with respective EDS maps of (b) Fe and (d) O.

## 5.7 Conclusions

SMCs are comprised of many material systems, all of which require a balance of microstructure and composition to reduce core loss and improve efficiency while maintaining magnetic performance. Although $Fe_3O_4$–coated Fe SMCs do not have high resistivity, we use this system to study the coating microstructure and shed light on optimal structural parameters, with certain restrictions and assumptions. Initially, we study the effect of $Fe_3O_4$–Fe bilayers in thin film form to compare an ideal crystalline state based on Fe layer thickness concentrations. We find that magnetization increases and coercivity decreases with thicker Fe layers, nominally higher ferromagnetic volumes. Likewise, we find crystallinity of thin films and dislocation densities at the coating–core interface to effect coercivity and magnetization the like. Although $Fe_3O_4$–coated Fe SMCs do not have high resistivity, we can use this system to study the coating microstructure and shed light on optimal

structural parameters, with certain restrictions and assumptions.

Ideally grain growth is beneficial for reducing hysteresis losses, however, the coating microstructure and thermal expansion may negate the increase in temperature. Reduction of structural defects will drastically increase eddy current loss in Fe powder SMCs, and will require a more resistive coating in order to minimize eddy current paths. We investigate the microstructural dependence of $Fe_3O_4$–coated Fe powder composites on soft magnetic properties such as hysteresis and eddy current loss. We find that the chemical composition of the coating layer is highly dependent on the transition temperature of $Fe_3O_4$ to FeO. There is a notable change in core loss from 700°C to 900°C, attributed to the stress relief of Fe and inter-particle eddy current paths developed from coating evolution. Our results suggest that coarser Fe particle sizes result in lower coercivity, higher densities, and lower eddy current losses and that curing temperatures above 700°C are viable for ferrite–based SMCs. The lowest hysteresis and eddy current losses were found at 700°C for the temperatures studied in this work, similarly compared to work by Sunday et al. of temperatures between 540°C and 900°C [156]. In addition, the lowest remnanent induction was present from the least amount of thermal expansion to the ferrite, causing the least amount of stress to the Fe and having the most structural defects in the coating. A network of pores and large amount of particle boundaries in the coating was proved to be beneficial for magnetite coating layers. We stress the importance of coating microstructure on magnetic core loss by separating the effects of hysteresis and eddy current loss.

We stress the importance of coating microstructure on magnetic core loss by separating the effects of hysteresis and eddy current loss. The balancing of properties will only truly be successful when all aspects of these material systems are studied in detail. A constant coating composition, despite being highly conductive, is maintained so that core loss contributions can be isolated at various frequencies and microstructural dependence can be compared. More resistive ferrite coatings, such as NiZn–ferrite with a resistivity of $\rho \sim 10^6$ $\Omega$·cm, may find their place and make a significant leap forward in the SMC industry and overall through electrifying automobiles. For this reason, we now discuss utilizing a NiZnCu–ferrite coating on Fe powder for improved electrical resistivity to greatly

reduce eddy current losses, while maintaining “soft” magnetic properties.

# Chapter 6: NiZnCu-ferrite Coating

## 6.1 Introduction

More resistive coating materials are studied in conjunction with the previously gained knowledge of microstructural effects on magnetic properties of ferrite–coated Fe powder composites. Combining two types of magnetic materials, one with high magnetization and the other with high electrical resistivity will ultimately improve the core loss and overall performance. Ferromagnetic materials (iron–, nickel–, cobalt–alloys) are applicable at low frequencies (<2 kHz) because of their high electrical conductivity, while ferrimagnetic materials (ceramic oxides or soft ferrites) are applicable at much higher frequencies [97]. NiZn–ferrites can be employed at UHF (ultra high frequency) between 300 MHz–3 GHz because of a high electrical resistivity of $\rho \sim 10^6$ $\Omega$·cm at room temperature [163]. Likewise, MnZn–ferrites ($\rho \sim 10^2$ $\Omega$·cm) are limited to below VHF (very high frequency) between 30–300 MHz because of more ferrous ($Fe^{2+}$) ions present drastically increasing conductivity and eddy current paths. This chapter focuses on one specific ferrite that allows for high magnetic saturation, low sintering temperatures, and much higher resistivity as compared to magnetite. NiZnCu–ferrite is known to have high frequency properties and lower sintering temperatures than pure NiZn–ferrite [164]. In addition, by substituting in $Cu^{2+}$ for $Ni^{2+}$, the bulk density will increase and allow for higher magnetic saturation as shown by Dimri et al. for $Ni_{0.4}Zn_{0.4}Cu_{0.2}Fe_2O_4$ ($M_s$= 92 emu·g$^{-1}$) compared to $Ni_{0.6}Zn_{0.4}Fe_2O_4$ ($M_s$= 77 emu·g$^{-1}$) [164]. Cation disorder in NiZn–ferrites are known to increase coercivity by introducing localized strain fields potentially limiting grain growth as well as causing localized anisotropy fields, both of which will increase hysteresis losses [165].

Several processing methods have been employed to develop NiZn–ferrite coatings and apply them to Fe particles for use as SMCs. Peng et al. [154] coated Fe with NiZn–ferrite by a co-precipitation process using stoichiometric amounts of Fe, Ni, and Zn chlorates. This method did not allow for curing temperatures above 500°C after which the ferrite began to decompose into $Fe_2O_3$ and the magnetic saturation reduced from 178.8 emu·g$^{-1}$ (after coating) to 148 emu·g$^{-1}$

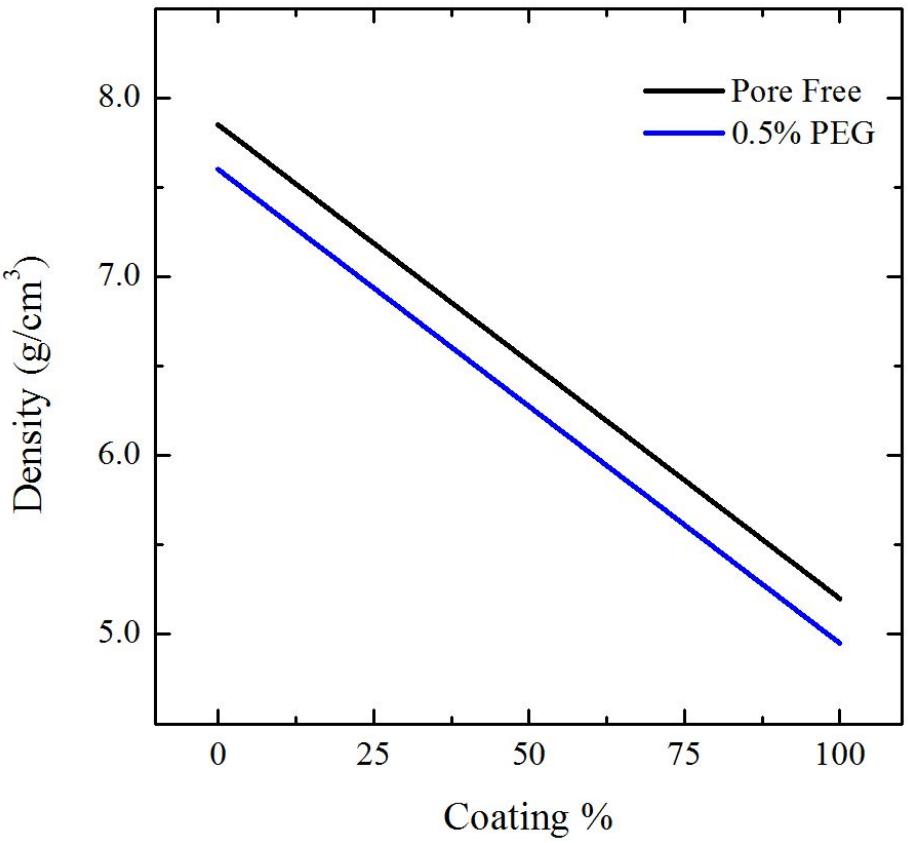


**Figure 6.1:** Effect of 0.5% PEG lubricant addition on the pore free density of Fe with NiZnCu–ferrite coating.

(after heating). There are numerous additional methods for preparing NiZn–ferrites, such as sol-gel synthesis [27, 42], chemical co-precipitation using hydroxides [155] or ceramic oxides [7, 26], and application of nanoparticles [4]. Our research does not focus on the methods to develop the ferrite material, but more importantly the techniques to apply the coating material to the Fe powder surfaces. We will continue the process of using traditional PM uniaxial compaction and curing in an inert atmosphere. Similarly, to coat the Fe particles we will also continue to use a simple mixing process. Wang et al. [4] used a 9:1 weight ratio of Fe to $Ni_{0.5}Zn_{0.5}Fe_2O_4$ nanopowder and mixed the components together to coat the Fe. However, spark plasma sintering (SPS) was used to sinter the coated Fe powder, which is an expensive technique and may not allow for proper stress relief of Fe. In addition, the study resulted in low magnetic saturation ($M_s$=1.65 T), which is not ideal for improving magnetic permeability and allowing for higher frequency applications.

Instead of using a high energy ball mill as previous chapters have, we now use a Resodyn$^{TM}$ acoustic mixer to reduce milling time and allow for more uniform mixing. This technique is capable of coating micron sized powder with nanopowder completely in less than 15 minutes as shown by Resodyn$^{TM}$ for Mg powder coated with MgO nanopowder [166]. We use an acoustic mixer to adequately coat Fe powder with ferrite particles. This research uses NiZnCu–ferrite particles of 5 wt%, 10 wt%, and 15 wt% with 0.5% PEG 6000 ($T_m$∼60°C) in order to melt the lubricant and provide and a sufficient pathway for ferrite particles to coat Fe powder.

## 6.2 Experimental Methods

As-received Ancorsteel 1000C Fe powder ($d_{ave}$>75 $\mu$m) (GKN–Hoeganaes Corp., NJ) is mixed with LSF50 NiZnCu–ferrite particles ($d_{ave}$∼0.4 to 0.6 $\mu$m) (Powder Processing & Technology, LLC, IN) using a Resodyn$^{TM}$ LabRAM II acoustic mixer (Resodyn$^{TM}$ Acoustic Mixers, Inc., MT) at 60 g for less than 10 minutes. The NiZnCu–ferrite particles are a low sintering (900°C) ferrite of proprietary stoichiometry with a flux density ($B_s$) of 3650 G and Curie temperature of 350°C. The NiZnCu–ferrite concentration varies from 5 wt% to 15 wt%, with a constant 0.5% lubricant addition of PEG (polyethylene glycol), for easy die stripping. A lubricant addition of 0.5% will reduce the overall density by an estimated 0.25 g·cm$^{-3}$ as shown in Figure 6.1. Temperatures are monitored in the powder blend after each trial, to confirm proper melting of lubricant addition. Toroid shapes and mechanical testing bars are warm compacted (100°C) at 800 MPa and cured for 1 h at 700°C in a pure nitrogen environment.

**Table 6.1:** Powder properties presented for each coating percentage, nominally apparent density and flow rate measured using Hall flow meter.

| **Coating %** | **Apparent Density** (g·cm$^{-3}$) | **Hall Flow Rate** (s) |
|---|---|---|
| 5 wt% | 3.06 | 26.41 |
| 10 wt% | 3.25 | 23.86 |
| 15 wt% | 3.16 | 25.09 |

Powder is first analyzed for apparent density [111] and hall flow rate [112] following ASTM standards B212 and B213, respectively, to determine effect of acoustic mixing and coating amount on powder properties. After compacting and curing, mechanical testing bars are measured for sintered

density, resistance using the four-point probe method, hardness using a Wilson Hardness tester with Rockwell HRA scale, and TRS using a Tinius Olsen H50KT following ASTM standard B312 [113]. Magnetic B–H loops are measured on toroid samples using a Model SMT 700 Soft Magnetic Hysteresigraph (KJS Associates, IN) following the same conditions as previous chapters. DC B–H loops are measured to a flux density of 25,000 G and applied field of 40 Oe. AC magnetization curves are performed at $B = 1$ T from 50 Hz to 5000 Hz. Measurements take into account averages of three samples per condition. Cross–sectioned toroid samples are imaged using optical microscopy to study the coating thickness and uniformity.

## 6.3 Results and Discussion

Acoustic mixing of iron, ferrite, and lubricant allows for quick coating procedures and control of powder temperature, to permit proper melting of the lubricant. We measure the temperature of the powder after each trial and find an average temperature of ∼77°C. At this temperature the PEG lubricant ($T_m$∼60°C) adequately melts, which facilitates a path for ferrite particles to coat Fe powder. Analyzing the powder after being coated for apparent density and flow rate confirm the positive use of a PEG lubricant for helping coat the core powder. As the particles surface roughness increases, nominally because of more coating material and agglomerations, the friction between particles during free flow will also increase. With this increased interparticle friction, the packing density during compaction will decrease, resulting in lower densities [6]. Apparent density is found by using a Hall flow meter and measuring the mass that occupies a specific volume, presented in Table 6.1. This test is performed three times for each sample set to obtain an accurate average. Likewise, the same instrument is used to determine the flow rate of the powder. A shorter flow rate represents a powder that has the ability to naturally flow with minimal interparticle friction contributions. On the contrary, higher flow rates indicate higher amounts of interparticle friction, which will cause some difficulty with handling, mixing, and packaging [6]. We find samples with 10 wt% coating to have the highest apparent density and lowest flow rate, presented in Table 6.1. These measurements indicate that 10 wt% is best for uniformly coating Fe particles and not creating higher amounts of agglomerations, which increase friction between particles. The lowest apparent density

and highest flow rate are found for 5 wt% coating. We attribute this to the large agglomerations of ferrite particles leading to insufficient coating of Fe powder and therefore more uneven surfaces.

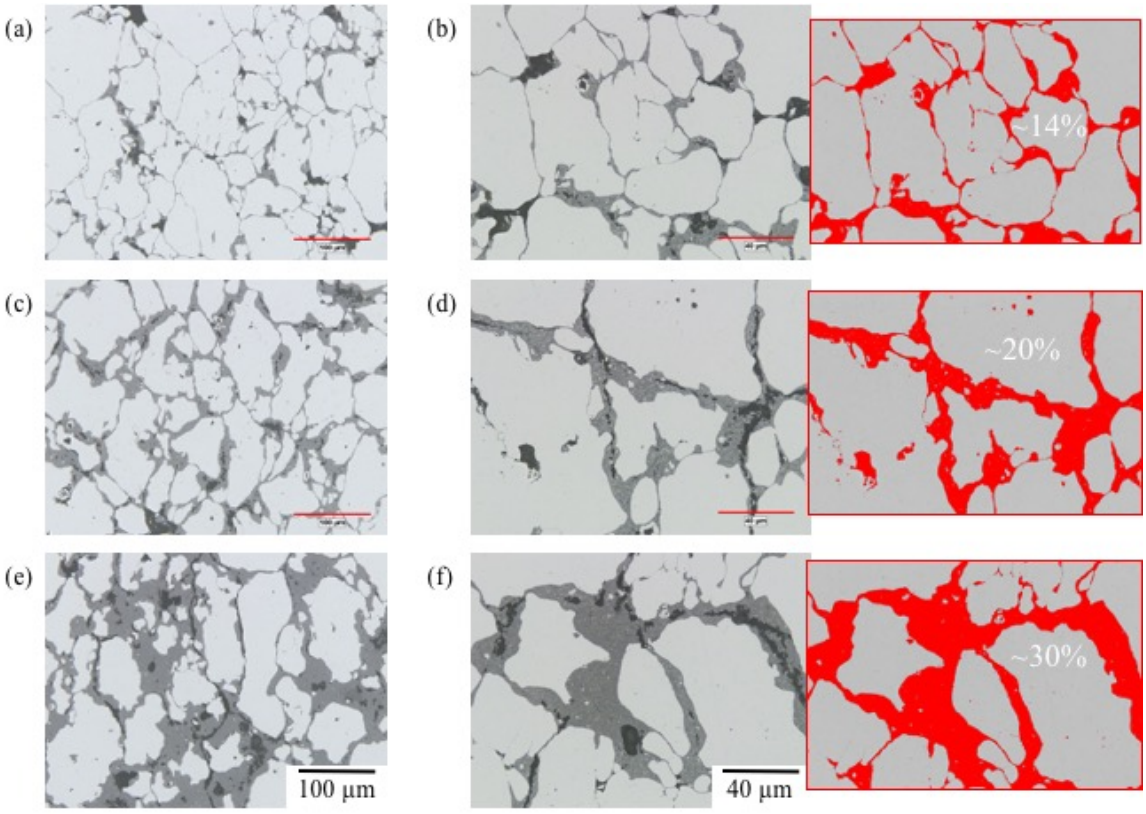


**Figure 6.2:** Optical micrographs of 5 wt% (a and b), 10 wt% (c and d), and 15 wt% (e and f) NiZnCu–ferrite coating on Fe cross-sectioned and polished.

**Table 6.2:** Density, relative density, and porosity content for three NiZnCu–ferrite coating amounts.

| | **Sintered Density** ($g \cdot cm^{-3}$) | **Theoretical Density** ($g \cdot cm^{-3}$) | **Relative Density** (%) | **Porosity** (%) |
|---|---|---|---|---|
| 5 wt% | 7.31 | 7.72 | 94.7% | 5.3% |
| 10 wt% | 6.99 | 7.59 | 92.2% | 7.8% |
| 15 wt% | 6.71 | 7.45 | 90.0% | 10.0% |

These insufficient coating layers with regions of large agglomerations are confirmed in optical micrographs seen in Figures 6.2a and 6.2b for 5 wt% NiZnCu–ferrite coating on Fe, compacted, and cured at 700°C. The optical micrographs indicate very thin coating layers that allow for higher densities, nominally 7.31 $g \cdot cm^{-3}$ for 5 wt% coating, which is 94.7% of theoretical density for this coating amount (Table 6.2). As discussed further later, this may not be enough to reduce eddy currents at high applied frequencies. As more ferrite material is added to the system, we see more

sufficient coating layers around all Fe particles, shown in Figures 6.2c and 6.2d for 10 wt% coating and Figures 6.2e and 6.2f for 15 wt% coating. From image analysis we see an increase in volume percentage of coating amount shown in red from ∼14% for 5 wt% NiZnCu–ferrite coating, ∼20% for 10 wt% coating, and ∼30% for 15 wt% coating. Regions of pores are not estimated with these images and therefore may skew the calculations slightly. However, the trend of increasing coating amount is determined based on volume percentage. With this increase in coating, we begin to see more interconnected pores that lead to the low densities and the formation of cracks, which propagate easily and reduce strength. The sintered density decreases accordingly with increasing coating amount (Table 6.2), and follows the rule of mixture trend shown in Figure 6.3. We attribute lower densities to higher amounts of pores where porosity increases from 5.3% to 10% for 5 wt% and 15 wt% coating material, respectively (Table 6.2). Theoretical densities greater than 90% are still relatively high compared to research by Lauda et al. with porosity levels >15% and permeability <40 for 5.9 wt% MnZn–ferrite coated Fe [27]. We credit lower densities can be attributed to less mechanical interlocking of Fe particles because the hard and brittle ferrite coating forms agglomerations impeding movement of Fe during compaction. Coating particles that cannot move further because of shearing or hardness of material will then rely on the softness of Fe to compact further, if at all. This can also be seen for the TRS values presented in Table 6.3, indicating higher amounts of coating material will reduce the mechanical strength of the component greatly. In addition, we see hardness increases for 10 wt% and 15 wt%, indicating that ferrite particles are pressing on the Fe powder during compaction, which induce more dislocations because the Fe material deforms more easily.

**Table 6.3:** Physical, mechanical, and electrical properties of NiZnCu–ferrite coated Fe composites.

| **Coating %** | **Sintered Density** ($g \cdot cm^{-3}$) | **TRS** (MPa) | **Hardness HRA** | **Resistance** (mΩ) |
|---|---|---|---|---|
| 5 wt% | 7.31 | 84.3 | 22.4 | 0.94 |
| 10 wt% | 6.99 | 62.3 | 31.7 | 4.32 |
| 15 wt% | 6.71 | 49.7 | 29.6 | 9.64 |

Electrical resistance measurements show a clear decrease in conductivity with increasing coating concentrations, as to be expected. The NiZnCu–ferrite used in this research has an estimated

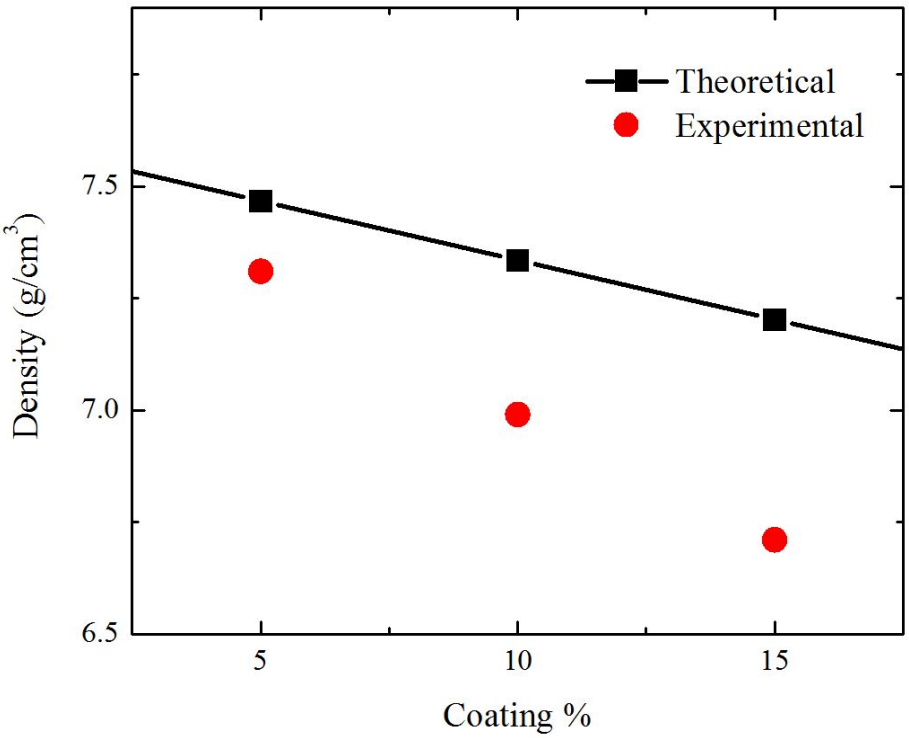


**Figure 6.3:** Effect of 5 wt%, 10 wt%, and 15 wt% NiZnCu-ferrite coating on density of Fe with PEG addition.

resistivity of $>10^5$ Ω·cm, which is much improved from Fe ($\sim 10^{-2}$ Ω·cm). As compared to the previous chapter using $Fe_3O_4$ as a coating material, this new ferrite material allows for higher resistance and better seclusion of eddy currents. Electrical resistivity is not presented because of polishing errors of sample surfaces, leading to inaccurate absolute resistivity measurements. With this being said, a trend in resistance is valid because all samples are of equal geometries and measured similarly. With the resistance values presented, we can anticipate lower eddy current losses for the 15 wt% coating samples. These values are extremely important when discussing eddy current losses, as they indicate more coating material will help decrease eddy current contributions in magnetic core loss, because the coating insulates individual Fe particles previously shown in Figure 6.2.

Chemical composition analysis of the NiZnCu–ferrite coating results are presented in Table 6.4 for the four indicated regions in Figure 6.4. We note a large difference for these semi-quantitative estimates of Ni–Zn–Cu stoichiometries. Points A and B are found to be inaccurate measurements because of the regions overlapping the Fe particles. The extra Fe contribution to the scans greatly

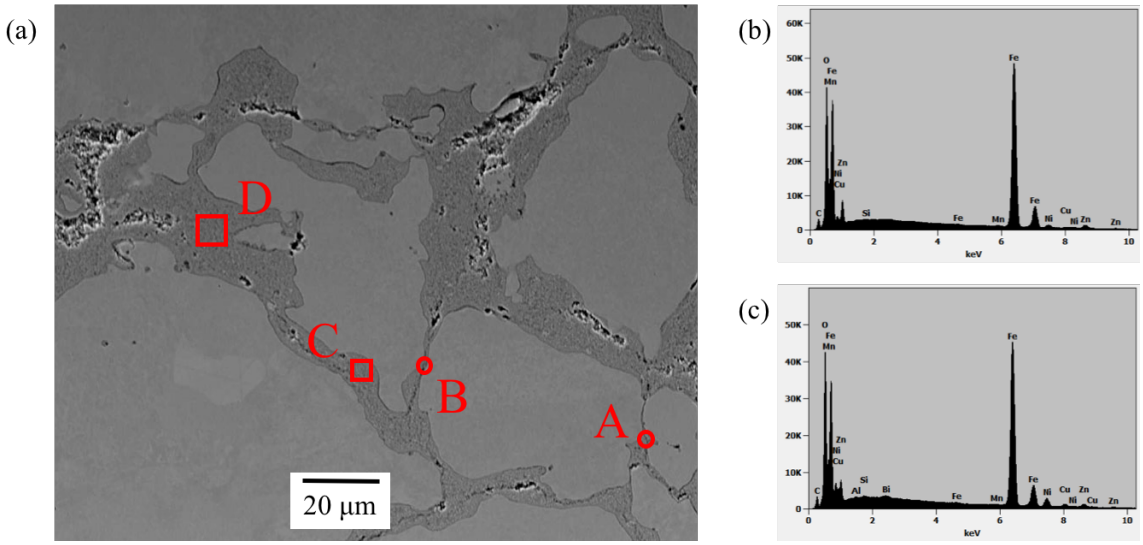


**Figure 6.4:** Optical micrograph (a) of 15 wt% NiZnCu–ferrite sample corresponding to chemical composition analysis of coating from point B (b) and point C (c).

**Table 6.4:** Chemical composition analysis corresponding to Figure 6.4 for points A, B, C, and D. Contributions of oxygen and miscellaneous elements are summed in the Element column labeled as Other.

| **Element** | **A (wt %)** | **B (wt %)** | **C (wt %)** | **D (wt %)** |
|---|---|---|---|---|
| Ni | 1.89 | 2.86 | 6.27 | 9.16 |
| Zn | 6.01 | 5.83 | 4.79 | 5.68 |
| Cu | 0.73 | 0.66 | 2.98 | 3.67 |
| Fe | 81.44 | 80.65 | 74.82 | 69.51 |
| Other | 9.93 | 10.00 | 11.14 | 11.98 |

affects the weight percentage of the other elements and are therefore not used for determining an accurate ferrite stoichiometry. We estimate our coating material to be $Ni_{0.5}Zn_{0.3}Cu_{0.2}Fe_2O_4$ after all processing steps have been completed. There is error in the method used for determining coating stoichiometry, however, this estimation is sufficient and allows us to compare magnetic results to past research. We note that this specific stoichiometry has not been presented for SMC applications previously.

**Table 6.5:** Magnetic permeability ($\mu_{max}$), remanent magnetization ($B_r$), coervcivity ($H_c$), and flux density reached ($B$) from DC magnetic toroid testing and magnetic saturation ($M_s$) from VSM measurements for samples cured at 700°C.

| Coating % | $\mu_{max}$ at 0 Hz | $B_r$ (G) | $H_c$ (A·m$^{-1}$) | $B$ (G) | $M_s$ (emu·g$^{-1}$) |
|---|---|---|---|---|---|
| 5 wt% | 190 | 535 | 196 | 10,000 | 209 |
| 10 wt% | 67 | 443 | 442 | ∼6,500 | 187 |
| 15 wt% | 41 | 420 | 212 | ∼4,700 | 170 |

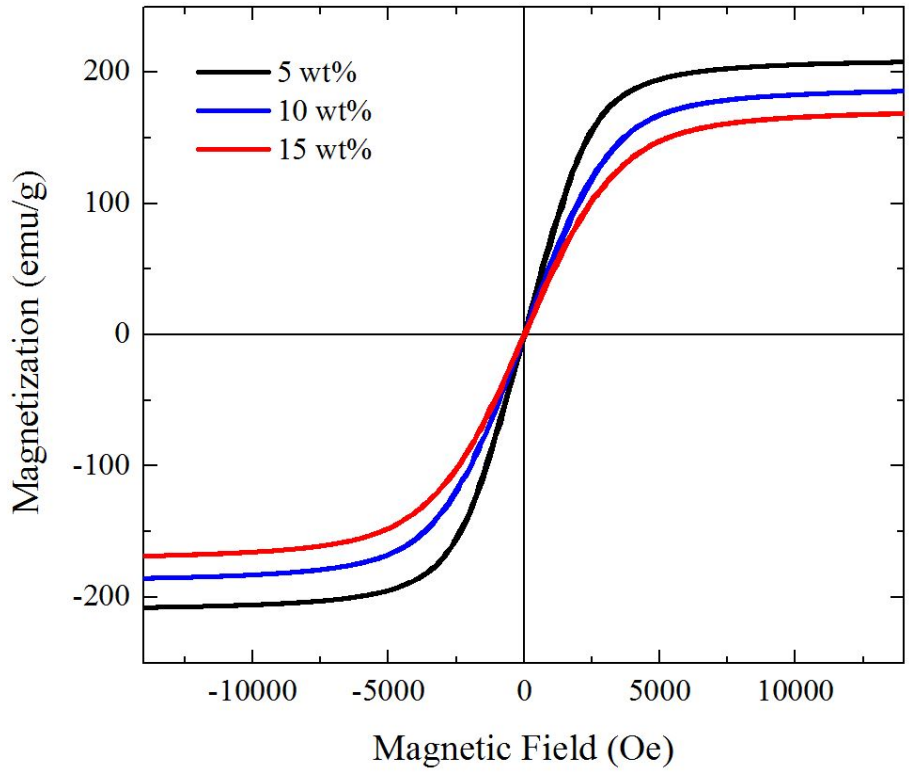


**Figure 6.5:** VSM B–H loops for 5 wt%, 10 wt%, and 15 wt% NiZnCu–ferrite coated Fe toroid cured at 700°C.

### 6.3.1 Magnetic Characterization

NiZnCu–ferrite coated Fe powder composites are magnetically tested for DC magnetic permeability, remanent induction, and coercivity using toroid shapes. The presented results (Table 6.5) indicate good "soft" DC magnetic properties for 5 wt% coating and decreasing performance as the coating amount increases. This trend is expected because increasing the coating amount decreases density and overall ferromagnetic volume. Permeability at 5 wt% is an enormous improvement from previous studies in this thesis as well as additional research in literature. Studies by Peng et al. indicate 4 wt% $Ni_{0.5}Zn_{0.5}Fe_2O_4$–coated Fe composites synthesized via microwave heat treatment and cured at 800°C have permeabilities less than 70 [7]. Our results using 5 wt% NiZnCu–ferrite and much simpler processing steps with a lower curing temperature allow for permeabilities of ∼190. We attribute an increase in permeability for our studies to coarser Fe particle sizes (>75 $\mu$m), while Peng et al. uses ∼31 $\mu$m Fe particles. The larger particle sizes allow for less nonmagnetic boundaries and more overall volume to allow for Fe stress relief.

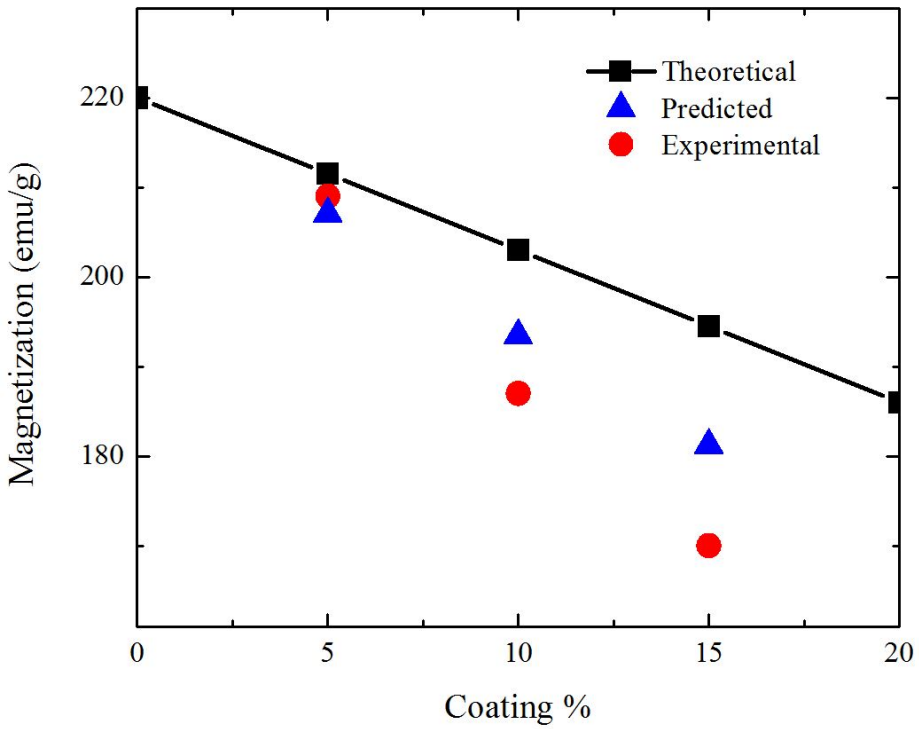


**Figure 6.6:** Comparison of magnetization for theoretical $M_s$, predicted $M_s$ based on density measurements, and experimental $M_s$ measured using VSM.

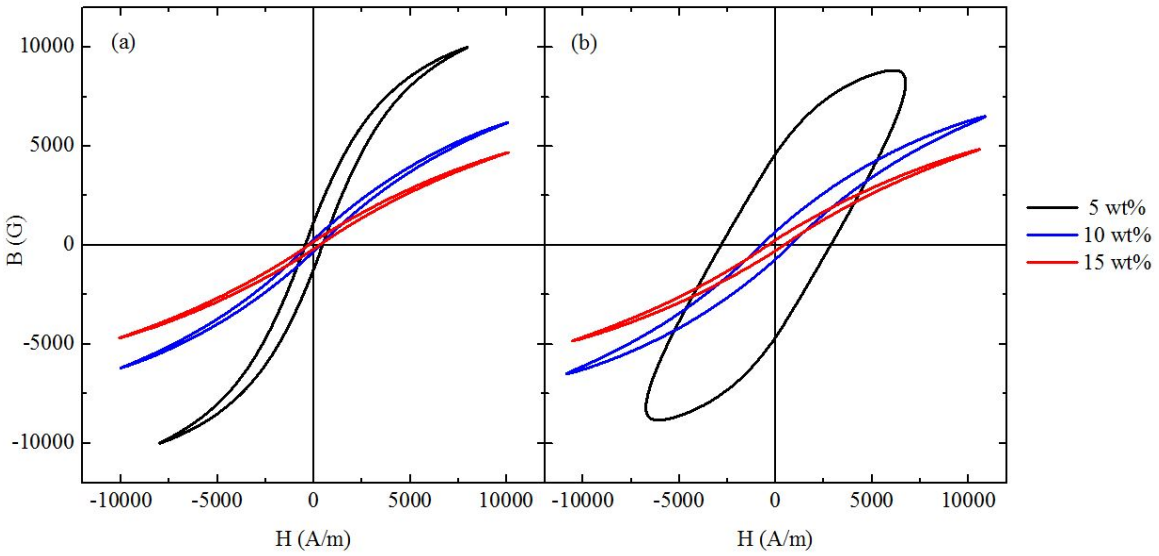


**Figure 6.7:** AC magnetic B–H loops tested at 50 Hz (a) and 1000 Hz (b) for 5 wt%, 10 wt%, and 15 wt% NiZnCu–ferrite coated Fe toroids cured at 700°C.

We perform VSM measurements to measure the magnetic saturation of each sample type shown in Figure 6.5. The corresponding values of magnetic saturation are presented in Table 6.5. As shown previously in Ch. 4 and 5, magnetic saturation decreases as coating amount increases, essentially from the decrease in ferromagnetic volume. The trend for magnetic saturation initially follows a rule of mixture scheme with 5 wt% coating (Fig. 6.6), but quickly diverts from this path at higher coating amounts. This can be attributed to the lower densities found for higher coating amounts, where compaction does not allow for Fe particle deformation because of the large amounts of ferrite material. We determine the predicted magnetization values based on previously discussed sintered density values. Knowing the difference between the theoretical and experimental densities, we can determine the predicted magnetization. The predicted and experimental values for saturation magnetization are much closer than the theoretical values, all attribute to the lower densities for higher coating amounts. We also note that a magnetic saturation of 209 emu·g$^{-1}$ is much improved from ∼148 emu·g$^{-1}$ presented by Peng et al. [154] and ∼169 emu·g$^{-1}$ presented by Lauda et al. [27]. In addition, our magnetization results of 10 wt% coating ($M_s$=187 emu·g$^{-1}$) is higher than values presented for 10 wt% NiZn–ferrite nanoparticles on Fe powder ($M_s$=165 emu·g$^{-1}$) by Wang et al. [4].

Larger particle sizes allow for higher densities and thus higher magnetic saturation for our studies. Acoustic mixing allows for low porosity levels because of the uniform coating layers present and the additional organic lubricant to allow for better compaction.

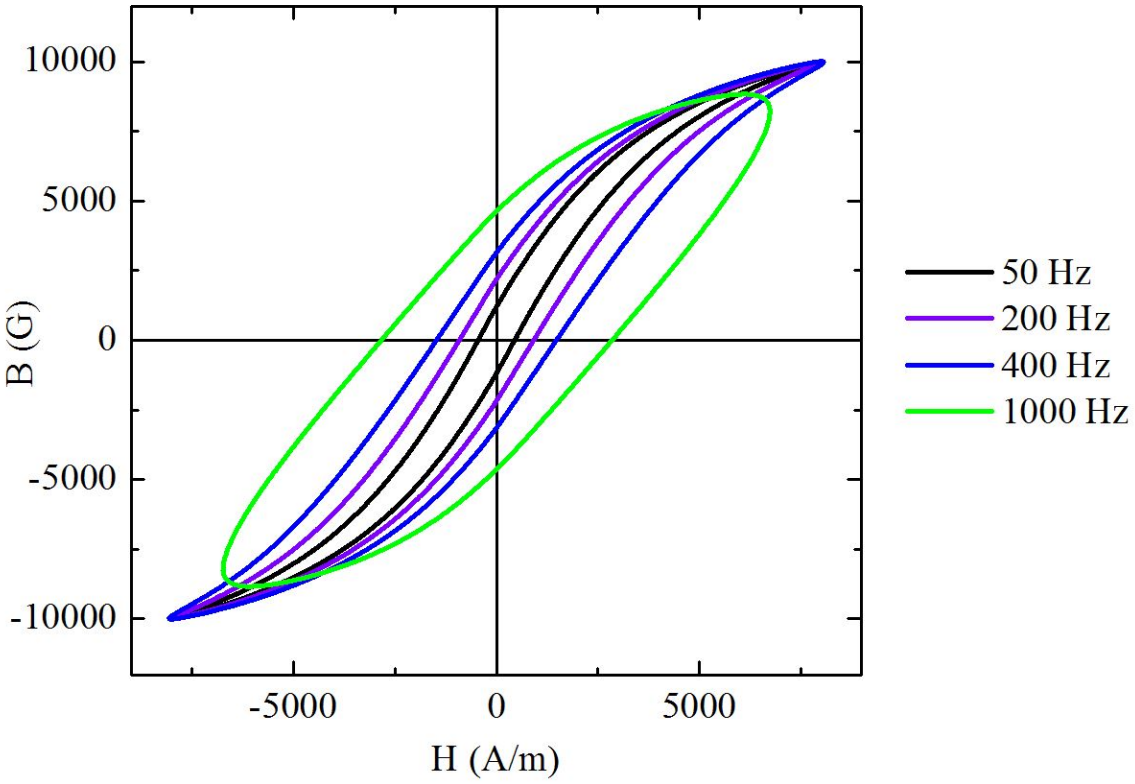


**Figure 6.8:** AC loops from 50 Hz to 1000 Hz for 5 wt% NiZnCu–ferrite coated Fe toroid cured at 700°C.

AC magnetic testing is equally important to determine acceptable frequency levels for NiZnCu–ferrite coatings. We present B–H loops for all three coating amounts, 5 wt%, 10 wt%, and 15 wt% at 50 Hz and 1000 Hz in Figure 6.7. The higher permeability presented previously for 5 wt% coating is clearly seen in Figure 6.7a at 50 Hz, where the slope of the loop is more aligned with the y-axis then the x-axis. However, we note that the area enclosed by the B–H loop for 5 wt% is much greater than the area for the 10 wt% or 15 wt% coating samples. This indicates a higher amount of hysteresis loss potentially from insufficient coating layers leading to large concentration of pores. Since we expect more Fe volume to improve hysteresis loss, we attribute the higher hysteresis losses to pore network and the B–H loop reaching the full 10,000 G limit. This material allows for a more accurate

hysteresis loop, and most likely may not have higher hysteresis losses then other coating amounts because of the higher fields reached. Likewise, as we increase frequency to 1000 Hz (Fig. 6.7b), an elliptical shaped loop is seen for 5 wt%, which clearly represents poor insulation between particles and eddy current contribution. Figure 6.8 illustrates the increase in coercivity and subsequently core losses as frequency increases from 50 Hz to 1000 Hz for 5 wt% coating cured at 700°C. At 400 Hz, the B–H loop still portrays a good magnetic hysteresis, which allows us to determine that the ferrimagnetic coating does not negatively affect magnetic properties significantly. The more crucial aspect for this material system is the overall resistivity, developed through the coating layers by the thickness and uniformity.

**Table 6.6:** Core loss values for each sample set at 50 Hz, 400 Hz, and 1000 Hz with the corresponding magnetic flux reached for each measurement. Samples are cured at 700°C.

| | **5 wt%** | | **10 wt%** | | **15 wt%** | |
|---|---|---|---|---|---|---|
| **Frequnecy** (Hz) | **Core Loss** ($W \cdot kg^{-1}$) | **B** (G) | **Core Loss** ($W \cdot kg^{-1}$) | **B** (G) | **Core Loss** ($W \cdot kg^{-1}$) | **B** (G) |
| 50 | 12 | 10,000 | 4 | 6,255 | 3 | 4,676 |
| 400 | 298 | 10,000 | 57 | 6,474 | 28 | 4,769 |
| 1000 | 1238 | 10,000 | 230 | 6,566 | 90 | 4,842 |

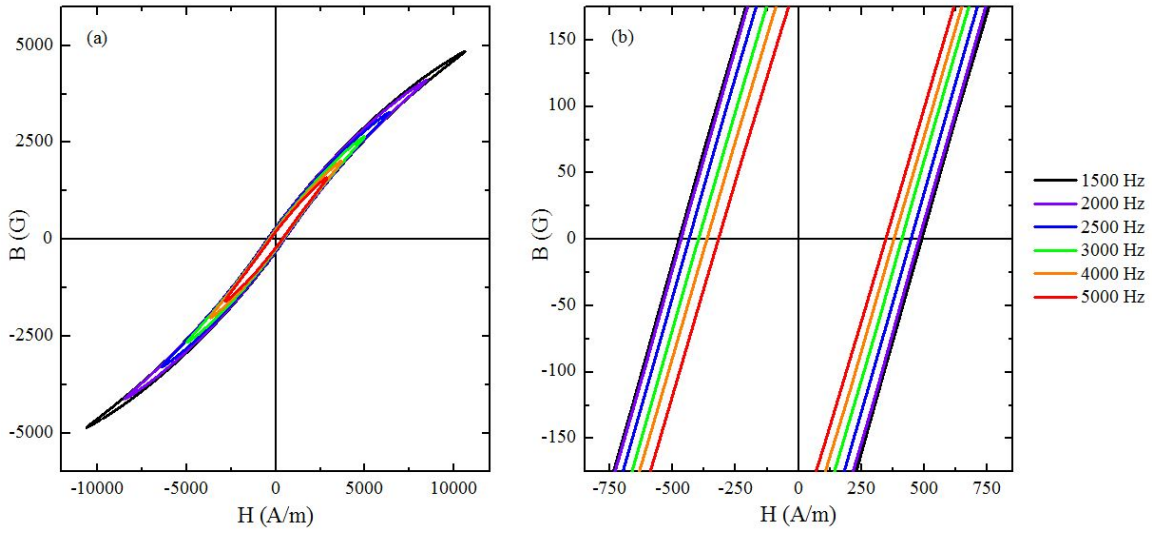


**Figure 6.9:** AC magnetic B–H loops (a) tested from 1500 Hz to 5000 Hz for 15 wt% NiZnCu–ferrite coated Fe toroids cured at 700°C. Zoomed in view (b) illustrating increase in coercivity as frequency increases.

We see coercivity increases for 10 wt% coating in Figure 6.7b, as compared to 15 wt% coating. This is explained by the higher resistivity of 15 wt% coating allowing for isolated eddy current losses

at 1000 Hz. However, the higher amount of coating material does reduce the magnetic permeability and magnetic flux density. This is seen in Figure 6.9a, for the 15 wt% coating system magnetically tested from 1500 Hz to 5000 Hz. As frequency increases the current needed to reach the materials magnetic flux capability also increases, however, for these measurements a standard maximum current of 10 mA is used. This allows for the illustration of magnetic capability with respect to coating amount. Although we see a slight decrease in coercivity (Fig. 6.9b) as frequency increases, we must consider that the overall magnetic flux density reached for each incremental measurement is decreasing. For example, at 1500 Hz the 15 wt% coating sample only reaches a magnetic flux of ∼5000 G, then the frequency is doubled to 3000 Hz, the magnetic flux drops in half to ∼2500 G. Therefore, the material does not fully saturate and the remanent induction decreases accordingly because there are less regions of magnetic spins aligned with the applied field, and reversing the magnetization is slightly easier. Summarized core loss values with the corresponding magnetic flux reached for each frequency level are shown in Table 6.6. As coating amount increases, a drop in magnetic flux is seen from 10,000 G at 5 wt% to ∼4700 G at 15 wt% coating.

To consider the 5 wt% coating material to be the best system for low frequency applications, we study the effect of increasing curing temperature to reduce hysteresis losses. However, B–H loops in Figure 6.10 for a curing temperature of 900°C clearly show a negative effect of increasing temperature as compared to Figure 6.8 for a curing temperature of 700°C. Since the resistivity of the 5 wt% coating at 700°C is already low, a higher curing temperature will only increase the number of metal–on–metal contact points and subsequently increase conductivity and eddy current losses. Therefore, we determine that a coating amount of 5 wt% cured at 700°C is a reasonable material system for low frequency (<400 Hz) applications. More coating material, nominally 10 wt%, will allow for higher frequencies, but magnetic permeability will suffer. The effect of increasing cure temperature from 700°C to 900°C to reduce hysteresis loss by allowing for Fe grain growth is shown for B–H loops in Figure 6.11. An increase in temperature drastically increases coercivity at 50 Hz and actually results in an elliptical loop at 400 Hz. For NiZnCu–ferrite coatings on Fe with no additional material present at the time of curing, the optimum temperature found in this study

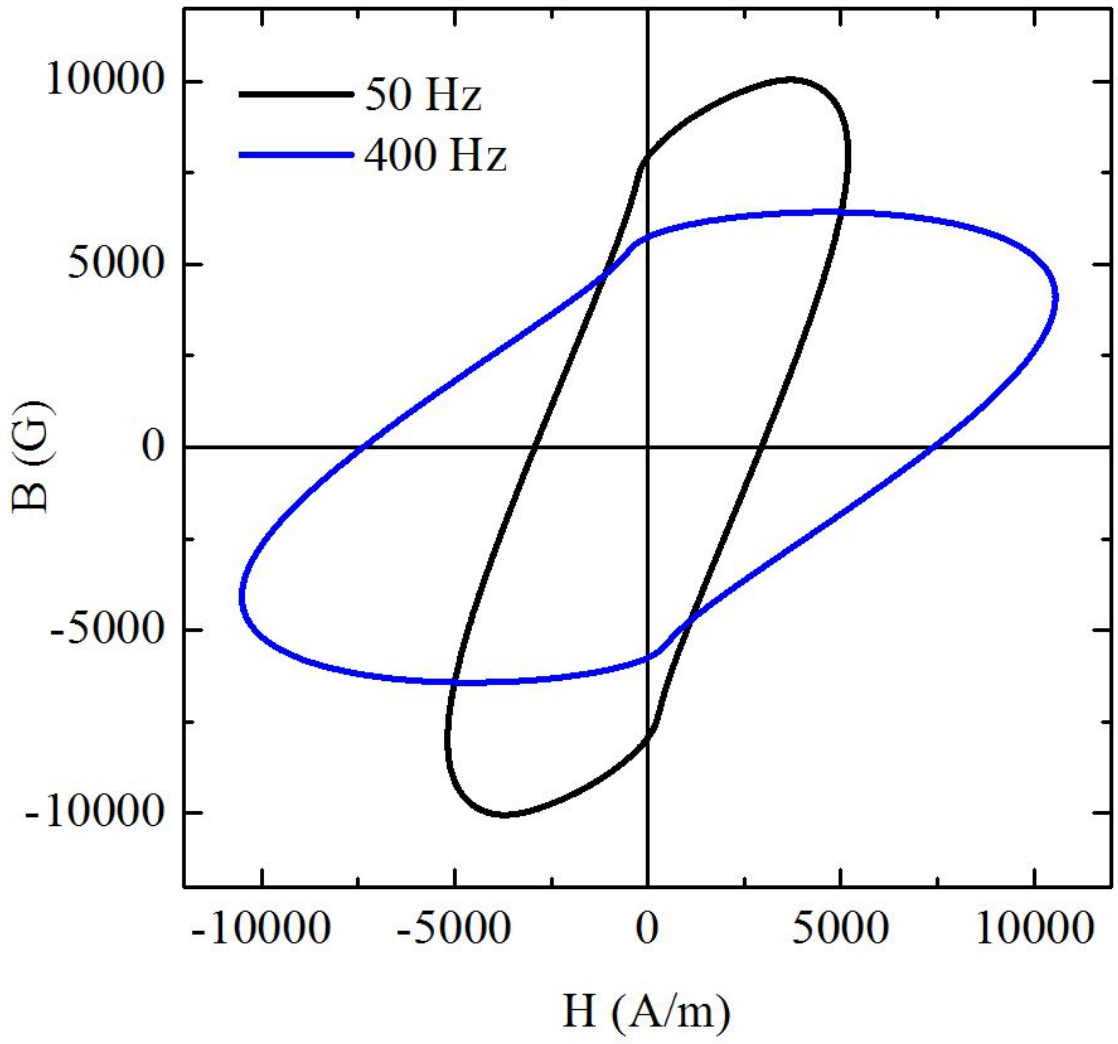


**Figure 6.10:** AC B–H loops for 50 Hz and 400 Hz for 5 wt% NiZnCu–ferrite coated Fe toroid cured at 900°C.

is around 700°C. Perhaps a more uniform coating method is needed to reduce possible regions of metal–on–metal contact points for the 5 wt% coating material to reduce inter–particle conductivity.

## 6.4 Conclusions

In this chapter, we describe the effect of using a more resistive coating material of NiZnCu–ferrite, to effectively reduce eddy current losses and minimally reduce magnetic performance. We find core loss is greatly reduced with coating amounts of 10 wt% and 15 wt%; however, magnetic induction is reduced as well. Higher coating amounts although beneficial for low $P_e$ require more current

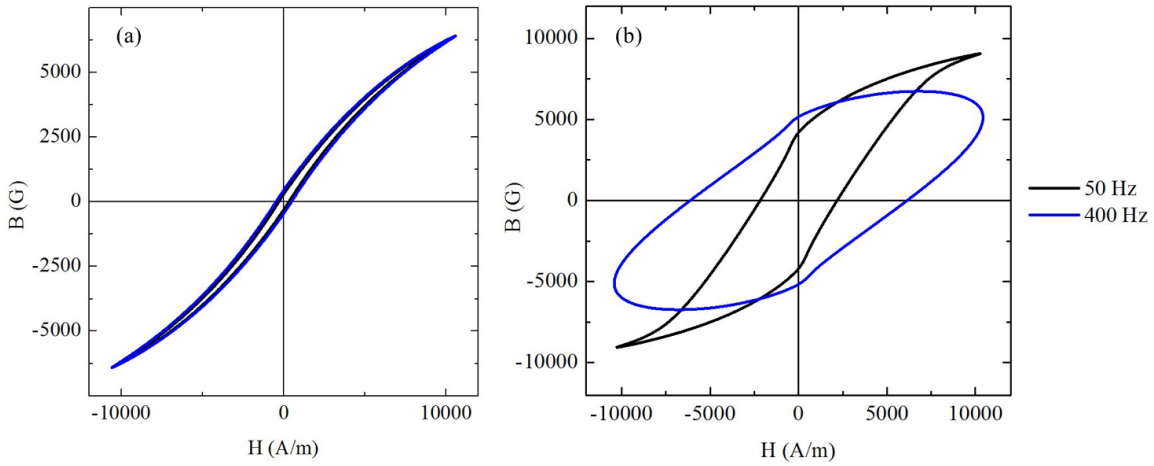


**Figure 6.11:** AC B–H loops for 50 Hz and 400 Hz for 10 wt% NiZnCu–ferrite coated Fe toroid cured at 700°C (a) and 900°C (b).

to obtain similar fields as smaller coatings amounts. Likewise, samples with 5 wt% have higher densities (7.31 g·cm$^{-3}$), higher TRS (84.3 MPa), and higher permeability (190). These samples also have the lowest resistance and therefore evidence of significant eddy current losses at 1000 Hz. The highest permeability found is most likely too low for practical use in SMCs, compared to available products on the market shown previously in Table 2.1, such as AncorLam [25] and Somaloy [57]. Additions of CuO or V will be used in future work to improve permeability of these material systems. Overall, this study exemplifies drastic improvements in core loss and magnetic performance at higher frequencies. There is clear evidence of the need for improved coating materials to properly balance magnetic performance with core loss and efficiency.

# Chapter 7: Conclusions

Soft magnetic composites (SMCs) consisting of ferrite–coated ferrous particles allow for improved electrical resistivity and good "soft" magnetic properties as compared to composites using organic or nonmagnetic inorganic coatings. Electrically insulating each ferrous particle with a ferrite coating material that allows for higher curing temperatures will reduce eddy current build-up and minimize hysteresis losses by allowing for proper stress relief. Utilizing both a ferrimagnetic coating and ferromagnetic core powder, SMCs can bridge the gap between traditional Si–Fe lamination steels and ferrite cores while maintaining high magnetic performance.

In this thesis, we describe the importance of coating material and structure on magnetic properties of Fe–based SMCs. An introductory study of $Al_2O_3$ and $Al_2O_3$–$Fe_3O_4$ coatings is used as proof of concept. We demonstrate the relationship between coating amount, varied via milling times and media ball sizes, and magnetization. A thorough comparison of $Fe_3O_4$–Fe thin film bilayers to previous studies by McDonald [11] and Spurgeon [50] is completed. We discuss the dependence of Fe layer thickness or ferromagnetic volume on magnetization and coercivity in an ideal crystalline state. Correlation of dislocation density and surface oxidation to magnetic properties are also elaborated on. We then transition to a highly strained state of $Fe_3O_4$–Fe material system using milled powder and pressed powder composites. Studies analyze the effect of particle size and cure temperature on magnetic properties such as coercivity and core loss. We further correlate microstructure of coating particles and iron powder to hysteresis and eddy current losses. Knowing that $Fe_3O_4$ is a poor insulator, we utilize a more resistive ferrimagnetic coating material, NiZnCu–ferrite, to reduce eddy current losses without drastically decreasing magnetic saturation and coercivity. We find an optimal balance of properties for samples of 10 wt% NiZnCu–ferrite coating on Fe powder, prepared using an acoustic mixer, compacted at 800 MPa and cured at 700°C for 1 h. This thesis correlates microstructure of ferrite–coated Fe SMCs to magnetic properties for a complete understanding of the effect of processing parameters employed.

## 7.1 Future Work

Ferrite–coated ferrous powder SMCs have the potential to impact the field of electromagnetic devices for electrification of automobiles. Avenues of future work may consist in developing additional ferrite coating materials, nominally substituting divalent cations in Ni–Zn ferrites [167]. Additions of CdO, CuO, CaO, CoO, and MgO have been shown to increase resistivity, permeability, and magnetization. Sintering temperature will also be effected, potentially allowing for better sintering of coating particles at lower temperatures. Future studies will incorporate various concentrations of such additions to the ferrite material studied previously, NiZnCu–ferrite, to investigate the effect of magnetic properties and sintering conditions. Without regarding cost, Co–Fe and Ni–Fe alloys will allow for improved flux density and magnetic permeability, respectively, as compared to pure Fe powder. The combination of more resistive coating materials with improved permeability with core powder of improved permeability or flux density will drastically improve core loss and magnetic performance.

In addition, higher packing densities will allow for higher densities to maximize magnetic properties and reduce overall porosity. This may be obtained by controlling the particle sizes of all materials to aid in the highest packing fraction. For example, with a size ratio of 7:1 (large to small particle sizes) and weight ratio of 73:27, a packing fraction of 0.86 can be obtained [6]. For this research, introducing fine particles to the medium or coarse particles may allow for voids and air gaps to be filled with more ferromagnetic material, potentially optimizing magnetic permeability. A further division of particle size ratio to include three sizes (49:7:1) will increase the packing fraction to 0.95, while another division using four particle sizes (343:49:7:1) will increase packing to 0.98 in theory. The later size ratio may be extremely difficult to produce, but even a packing fraction of 0.95 using 49:7:1 is much improved from 0.64 using a size ratio of 1. Lastly, increasing compaction pressure will drastically improve density and allow for lower amounts of pores and higher mechanical strength. Although this may not be practical in an industry setting, this will allow for higher magnetic permeability and lower core losses to illustrate the potential of ferrite coatings on Fe powder SMCs.

Ferrite coatings will allow for a new range of frequencies for SMCs to be incorporated into everyday use. $Fe_3O_4$ coatings may be utilized in a low frequency regime (∼1–5 kHz), while Ni–Zn ferrite coatings may push the limits to the medium frequency range of between 300–3000 kHz. Manipulating the core powder composition and microstructure to improve magnetic properties will ultimately allow for better magnetic performance at higher frequencies, at a higher cost depending on materials and processing. Electric motors will not be the only application to benefit drastically, but rather applications that have not even been developed yet will utilize SMC materials. Future work will test materials at higher frequencies to determine the proper application ranges for future developments. All of the proposed avenues for future work aim to optimize magnetic properties using previously gained knowledge of microstructure and composition for ferrite–coated Fe–based SMCs.

# Bibliography


[1] H. Shokrollahi and K. Janghorban. Soft magnetic composite materials (SMCs). *J. Mater. Process. Technol.*, 189:1–12, 2007.

[2] P. D. Barba, M. Bonislawski, R. Palka, P. Paplicki, and M. Wardach. Design of hybrid excited synchronous machine for electrical vehicles. *IEEE Trans. Magn.*, 51(8), 2015.

[3] GKN Sinter Metals develops motor using SMC materials. *Metal Powder Report*, July/August:45, 2013.

[4] M. Wang, Z. Zan, N. Deng, and Z. Zhao. Preparation of pure iron/Ni–Zn ferrite high strength soft magnetic composites by spark plasma sintering. *J. Magn. Magn. Mater.*, 361:166–169, 2014.

[5] GKN Sinter Metals. Sintered soft magnetic products, 2016.

[6] R. M. German. *Powder Metallurgy Science*. Metal Powder Industry, 2nd edition, 1994.

[7] Y. Peng, J. Nie, W. Zhange, C. Bao, J. Ma, and Y. Cao. Preparation of soft magnetic composites for Fe particles coated with (NiZn)$Fe_2O_4$ via microwave treatment. *J. Magn. Magn. Mater.*, 395:245–250, 2015.

[8] D. B. Williams and C. B. Carter. *Transmission Electron Microscopy: A Textbook for Materials Science*. Springer, 1996.

[9] S. I. Wright, M. M. Nowell, and D. P. Field. A review of strain analysis using electron backscatter diffraction. *Microsc. Microanal.*, 17:316–329, 2011.

[10] M. Bi, X. Wang, H. Lu, L. Deng, K. J. Sunday, M. L. Taheri, and V. G. Harris. Magnetic and microwave propertie of FeCoNbBCu thin films. *J. Appl. Phys.*, 119:023906, 2016.

[11] I. J. McDonald. Development of a Unique Surface Magneto-Optical Kerr Effect Magnetometer to Correlate Magnetism and Structure in Fe–$Fe_3O_4$ Thin Film Bilayers. Master's thesis, Drexel University, July 2012.

[12] L. P. Lefebvre, S. Pelletier, B. Champagne, and C. Gélinas. Effect of resin content and iron powder particle size on properties of dielectromagnetics. *Advances in Powder Metallurgy and Particulate Materials*, 6:47–61, 1996.

[13] H. A. Toliyat and G. B. Kliman, editors. *Handbook of Electric Motors*. CRC Press, 2nd edition, 2004.

[14] Y. G. Guo, J. G. Zhu, P. A. Watterson, and W. Wu. Comparitive study of 3D flux electrical machines with soft magnetic composite cores. *IEEE Trans. Ind. Applicat.*, 39(6):1696–1703, 2003.

[15] N. B. Dhokey, S. Patil, S. Dhandare, and V. S. Bandal. Role of ceramic coating on electrical and magnetic properties of iron powder. *Electron. Mater. Lett.*, 10(3):591–596, 2014.

[16] H. Shokrollahi, K. Janghorban, F. Mazaleyrat, M. Lo Bue, V. Ji, and A. Tcharktchi. Investigation of magnetic properties, residual stress and densification in compacted iron powder specimens coated with polyepoxy. *Mater. Chem. Phys.*, 114:588–594, 2009.

[17] P. B. G. Slusarek and M. Przybylski. New PM magnetic developments. *Metal Powder Report*, 64(6):18–24, 2009.

[18] T. A. Laxminarayana, S. K. Manna, Fernandes B. G., and Venkataramani N. Study of AC magnetic properties and core losses of $Fe/Fe_3O_4$-epoxy resin soft magnetic composite. *Physics Procedia: 20th International Conference on Magnetism*, 75:1396–1403, 2015.

[19] M. Strečková, J. Füzer, L'. Medvecký, R. Bureš, P. Kollár, M. Fáberová, and V. Girman. Characterization of composite materials based on Fe powder (core) and phenol-formaldehyde resin (shell) modified with nanometer-sizes $SiO_2$. *Bull. Mater. Sci.*, 37(2):167–177, 2014.

[20] Y.-W. Zhao, X. K. Zhang, and J. Q. Xiao. Submicrometer laminated $Fe/SiO_2$ soft magnetic composites - an effective route to materials for high-frequency applications. *Adv. Mater.*, 17(7), April 2005.

[21] B. Yang, Z. Wu, Z. Zou, and R. Yu. High-performance $Fe/SiO_2$ soft magnetic composites for low-loss and high-power applications. *Journal of Physics D: Applied Physics*, 43:365003, 2010.

[22] W. Xu, C. Wu, and M. Yan. Preparation of Fe-Si-Ni soft magnetic composites with excellent high-frequency properties. *J. Magn. Magn. Mater.*, 381:116–119, 2015.

[23] W. Ding, L. Jiang, Y. Liao, J. Song, B. Li, and G. Wu. Effect of iron particle size and volume fraction on magnetic properties of Fe/silicate glass soft magnetic composites. *J. Magn. Magn. Mater.*, 378:232–238, 2015.

[24] J. Doering, G. Steinborn, and W. Hofmann. Torque, power, losses, and heat calculation of a transverse flux reluctance machine with soft magnetic composite materials and disk-shaped rotor. *IEEE Trans. Ind. Appl.*, 51(2):1494–1504, 2015.

[25] L. Frayman, S. Quinn, R. Quinn, D. Green, and F. Hanejko. Advanced soft magnetic composite materials for AC applications with reduced iron losses. *Powder Metalurgy*, 58(5):335–338, 2015.

[26] K. Gheisari, S. Javadpour, H. Shokrollahi, and B. Hashemi. Magnetic losses of the soft magnetic composites consisting of iron and Ni–Zn ferrite. *J. Magn. Magn. Mater.*, 320:1544–1548, 2008.

[27] M. Lauda, J. Fuzer, P. Kollár, R. Bureš, J. Kovac, M. Batkova, and I. Batko. Magnetic properties and loss separation in $FeSi/MnZnFe_2O_4$ soft magnetic composites. *J. Magn. Magn. Mater.*, 411:12–17, 2016.

[28] A. H. Taghvaei, H. Shokrollahi, K. Janghorban, and H. Abiri. Eddy current and total power loss separation in the Iron-phosphate-polyepoxy soft magnetic composites. *Mater. Design*, 30:3989–3995, 2009.

[29] Y. Guo, J. Zhu, and D. G. Dorrell. Design and analysis of a claw pole permanent magnet motor with molded soft magnetic composite core. *IEEE Trans. Magn.*, 45(10):4582–4585, 2009.

[30] G. Lei, J. Zhu, Y. Guo, K. Shao, and W. Xu. Multilevel design optimization of a FSPMM drive system by using sequential subspace optimization method. *IEEE Trans. Magn.*, 50(2):7017704, 2014.

[31] R. Goldstein. Induction heating and heat treatment. *ASM Handbook*, 4C:633–645, 2014.

[32] R. Ruffini, N. Vyshinskaya, V. Nemkov, and R. Goldstein. Innovations in Soft Magnetic Composites and their Applications in Iinduction Systems. *Proceedings of the 27th Heat Treating Society Conference*, 2013.

[33] N. Nishiyama, K. Tanimoto, and A. Makino. Outstanding efficiency in energy conversion for electric motors constructure by nanocrystalline soft magnetic alloy "NANOMET" cores. *AIP Adv.*, 6(5):055925, 2016.

[34] T. Ishikawa, S. Sato, S. Takeguchi, and A. Matsuo. Design of a DC motor made of soft magnetic composite core by the experimental design method. *IEEE Transactions on Magnetics*, 48(11):3132–3135, 2012.

[35] M. M. Dias, H. J. Mozetic, J. S. Barboza, R. M. Martins, L. Pelegrini, and L. Schaeffer. Influence of resin type and content on electrical and magnetic properties of soft magnetic composites (SMCs). *Powder Technology*, 237:213–220, 2013.

[36] P. Kollár, V. Vojtek, Z. Birčáková, J. Füzer, M. Fáberová, and R. Bureš. Steinmetz law in iron-phenolformaldehyde resin soft magnetic composites. *J. Magn. Magn. Mater.*, 353:65–70, 2014.

[37] C. G. Oliver and H. G. Rutz. Powder metallurgy in electronic applications. *Adv. Powder. Metall. Part. Mater.*, 3(11):87–102, 1995.

[38] W. Liu, W. Zhong, H. Jiang, N. Tang, X. Wu, and Y. Du. Highly stable alumina-coated iron nanocomposites synthesized by wet chemistry method. *Surf. Coat. Technol.*, 200:5170–5174, 2006.

[39] M. Strečková, L'. Medvecký, J. Füzer, P. Kollár, R. Bureš, and M. Fáberová. Design of novel soft magnetic composites based on Fe/resin modified with silica. *Mater. Lett.*, 101:37–40, 2013.

[40] S. Wu, A. Sun, Z. Lu, C. Cheng, and X. Gao. Magnetic properties of iron-based soft magnetic composites with $SiO_2$ coating obtained by reverse microemulsion method. *J. Magn. Magn. Mater.*, 381:451–456, May 2015.

[41] X. Zhong, Y. Liu, J. Li, and Y. Wang. Structure and magnetic properties of FeSiAl-based soft magnetic composite with AlN and $Al_2O_3$ insulating layer prepared by selective nitridation and oxidation. *J. Magn. Magn. Mater.*, 324:2631–2636, 2012.

[42] S. Wu, A. Sun, W. Xu, Q. Zhang, F. Zhai, P. Logan, and A. A. Volinsky. Iron-based soft magnetic composites with Mn-Zn ferrite nanoparticles coating obtained by sol-gel method. *J. Magn. Magn. Mater.*, 324(22):3899–3905, November 2012.

[43] G. Zhao, C. Wu, and M. Yan. Fe-based soft magnetic composites with high $B_s$ and low core loss by acidic bluing coating. *IEEE Trans. Magn.*, 51(11):2002094, 2015.

[44] W. R. Nolan. *Electrically Insulating Phosphate Coatings for Iron Powder Based Electromagnetic Core Applications*. Massachusetts Institute of Technology, June 2009.

[45] G. Uozumi, M. Watanabe, R. Nakayama, K. Igarashi, and K. Morimoto. Properties of soft magnetic composite with evaporated MgO insulation coating for low iron loss. *Mater. Sci. Forum*, 534-536:1361–1364, 2007.

[46] A. H. Taghvaei, H. Shokrollahi, M. Ghaffari, and K. Janghorban. Influence of particle size and compaction pressure on the magnetic properties of iron-phenolic soft magnetic composites. *J. Phys. Chem. Solids*, 71:7–11, 2010.

[47] C. Cyr, P. Viarouge, S. Clénet, and J. Cros. Methodology to study the influence of the microscopic structure of soft magnetic composites on their global magnetization curve. *IEEE Trans. Magn.*, 45(3), March 2009.

[48] K. J. Sunday, K. A. Darling, F. G. Hanejko, B. Anasori, Y. C. Liu, and M. L. Taheri. $Al_2O_3$ "self-coated" iron powder composites via mechanical milling. *J. Alloys Compd.*, 653:61–68, 2015.

[49] M. Sugimoto. The Past, Present, and Future of Ferrites. *J. Am. Ceram. Soc.*, 82(2):269–280, 1999.

[50] S. R. Spurgeon. *Correlating Interfacial Structure and Magnetism in Thin-Film Oxide Heterostructures Using Transmission Electron Microscopy and Polarized Neutron Reflectometry.* PhD thesis, Drexel University, October 2014.

[51] G. Zhao, C. Wu, and M. Yan. Enhanced magnetic properties of Fe soft magnetic composites by surface oxidation. *J. Magn. Magn. Mater.*, 399:51–57, 2016.

[52] K. J. Sunday, F. G. Hanejko, and M. L. Taheri. $Fe_3O_4$-coated Iron Powder Composites for SMC Applications. *PowderMet Conference Proceedings*, June 2016.

[53] K. J. Sunday, F. G. Hanejko, and M. L. Taheri. Magnetic and microstructural properties of $Fe_3O_4$-coated Fe powder soft magnetic composites. *J. Magn. Magn. Mater.*, 423:164–170, 2017.

[54] Y. Peng, J. Nie, W. Zhang, J. Ma, C. Bao, and Y. Cao. Effect of the addition of $Al_2O_3$ nanoparticles on the magnetic properties of Fe soft magnetic composites. *J. Magn. Magn. Mater.*, 399:88–93, 2016.

[55] L. P. Lefebvre, S. Pelletier, and C. Gélinas. Effect of electrical resistivity on core losses in soft magnetic iron powder materials. *J. Magn. Magn. Mater.*, 176(2-3):L93–L96, 1997.

[56] M. De Wulf, L. Anestiev, L. Dupré, L. Froyen, and J. Melkebeek. Magnetic properties and loss separation in iron powder soft magnetic composite materials. *Journal of Applied Physics*, 91(10), May 2002.

[57] Hoganas AB. Somaloy technology for electric motors, March 2011.

[58] C. W. Chen. *Magnetism and Metallurgy of Soft Magnetic Materials.* Dover Publications, NY, 1986.

[59] N. A. Spaldin. *Magnetic Materials: Fundamentals and Applications.* Cambridge University Press, 2 edition, 2011.

[60] A. Hubert and R. Schafer. *Magnetic Domains: The Analysis of Magnetic Microstructures.* Springer, 1998.

[61] T. Schafter, J. Burghaus, W. Pieper, F. Petzoldt, and M. Busse. New concept of Si–Fe based sintered soft magnetic composite. *Powder Metall.*, 58(2):106–111, 2014.

[62] A. H. Bahrami, H. Ghayour, and S. Sharafi. Evolution of microstructural and magnetic properties of mechanically alloyed $Fe_{80-x}Ni_{20}Si_x$ nanostructured powders. *Powder Technology*, 249:7–14, 2013.

[63] E. A. Périgo, S. Nakahara, Y. Pittini-Yamada, Y. de Hazan, and T. Graule. Magnetic properties of soft magnetic composites prepared with crystalline and amorphous powders. *J. Magn. Magn. Mater.*, 323:1938–1944, 2011.

[64] A. Goldman. *Modern Ferrite Technology.* Springer, 2 edition, 2006.

[65] L. Svensson, K. Frogner, P. Jeppsson, T. Cedell, and M. Andersson. Soft magnetic moldable composites: Properties and applications. *J. Magn. Magn. Mater.*, 324:2717–2722, 2012.

[66] M. Shiozaki and Y. Kurosaki. The effects of grain size on the magnetic properties of nonoriented electrical steel sheets. *Journal of Materials Engineering*, 11(1):37–43, 1989.

[67] M. Anhalt. Systematic investigation of particle size dependence of magnetic properties in soft magnetic composites. *J. Magn. Magn. Mater.*, 320(14), 2008.

[68] A. Sumper and A. Bahhini. *Electrical Energy Efficiency: Technologies and Applications.* John Wiley and Sons, 2012.

[69] O. de la Barriere, C. Appino, F. Fiorillo, R. Carlo, H. B. Ahmed, M. Gabsi, F. Mazaleyrat, and M. LoBue. Loss separation in soft magnetic composites. *J. Appl. Phys.*, 109, 2011.

[70] Standard test method for high-frequency (10 khz - 1 mhz) core loss of soft magnetic core components at controlled temperatures using the voltmeter-ammeter-wattmeter method. ASTM Standard A103, ASTM International.

[71] O. de la Barriere, C. Appino, C. Ragusa, F. Fiorillo, F. Mazaleyrat, and M. LoBue. High frequency rotational losses in different soft magnetic composites. *J. Appl. Phys.*, 115, 2014.

[72] A. Revesz, T. Ungar, A. Borbely, and J. Lendvai. Dislocations and grain size in ball-milled iron powder. *Nanostructure Materials*, 7(7):779–788, 1996.

[73] Y. Kimura, H. Hidaka, and S. Takaki. Work-hardening mechanism during super-heavy plastic deformation in mechanically milled iron powder. *Materials Transactions*, 40(10):1149–1157, 1999.

[74] S. Hallstrom, L. Hoglund, and J. Agren. Modeling of iron diffusion in the iron oxides magnetite and hematite with variable stoichiometry. *Acta Materialia*, 59:53–60, 2011.

[75] C. Appino, O. de la Barrie're, F. Fiorillo, M. LoBue, F. Mazaleyrat, and C. Ragusa. Classical eddy current losses in soft magnetic composites. *J. Appl. Phys.*, 113:17A322, 2013.

[76] M. E. McHenry, M. A. Willard, and D. E. Laughlin. Amorphous and nanocrystalline materials for applications as soft magnets. *Prog. Mater. Sci.*, 44:291–433, 1999.

[77] C. Oikonomou, D. Nikas, E. Hryha, and L. Nyborg. Effect of heat treatment in air on surface composition of iron-phosphate based soft magnetic composite components. *Mater. Sci. Eng., B*, 189:90–99, 2014.

[78] M. Yaghtin, A. H. Taghvaei, B. Hashemi, and K. Janghorban. Effect of heat treatment on magnetic properties of iron-based soft magnetic composites with $Al_2O_3$ insulation coating produced by sol-gel method. *J. Alloys Compd.*, 581:293–297, 2013.

[79] A. H. Taghvaei, A. Ebrahimi, M. Ghaffari, and K. Janghorban. Analysis of the magnetic losses in iron-based soft magnetic composites with MgO insulation produced by sol-gel method. *J. Magn. Magn. Mater.*, 322(23):3748–3754, 2010.

[80] M. A. Malik, M. Y. Wani, and M. A. Hashim. Microemulsion method: A novel route to synthesize organic and inorganic nanomaterials. *Arab. J. Chem.*, 5(4):397–417, 2012.

[81] H. Bruncková, M. Kabátová, and E. Dudrová. The effect of iron phosphate, alumina and silica coatings on the morphology of carbonyl iron particles. *Surf. Interface Anal.*, 42:13–20, 2010.

[82] Y. W. Zhao, T. Zhang, and J. Q. Xiao. Explosion compacted FeCo particles coated with ferrites: A possible route to achieve artificial soft ferrites. *J. Appl. Phys.*, 93:8014, 2003.

[83] R. Guicheteau, J. L. Bobet, Y. F. Lu, M. L. Troedec, and J. F. Silvain. Ferrite coating on iron particles in aqueous solution: Effect of surface functionalization. *Materials Science and Engineering*, 4(5), 2015.

[84] J. S. Salazar, L. Perez, O. de Abril, L. T. Phuoc, D. Ihiawakrim, M. Vazquez, J. M. Greneche, S. Begin-Colin, and G. Pourroy. Magnetic iron oxide nanoparticles in 10-40 nm range: Composition in terms of magnetite/maghemite ratio and effect on magnetic properties. *Chemistry of Materials*, 23(6):1379–1386, 2011.

[85] J. Sun, S. Zhou, P. Hou, Y. Yang, J. Weng, X. Li, and M. Li. Synthesis and characterization of biocompatible $Fe_3O_4$ nanoparticles. *Journal of Biomedical Materials Research A*, 80(2):333–341, 2007.

[86] D. H. Liu, Y. Liu, D.-P. Zhao, Y. Wang, J.-H. Fang, Y.-R. Wen, and Z.-M. Liu. Effect of ball milling time on microstructures and mechanical properties of mechanically-alloyed iron-based materials. *Trans. Nonferr. Met. Soc. China*, 20(5):831–838, 2010.

[87] T. T. Bui, X. Q. Le, D. P. To, and V. T. Nguyen. Investigation of typical properties of nanocrystalline iron powders prepared by ball milling techniques. *Adv. Nat. Sci. Nanosci. Nanotechnol.*, 4, 2013.

[88] K. N. Rozanov, D. A. Petrov, A. N. Maratkanova, A. A. Chulkina, and S. F. Lomayeva. Microwave properties of powders produced by high-energy milling of iron with paraffin. *The Physics of Metals and Metallography*, 115(7):642–649, 2014.

[89] I. Hemmati, H. R. Madaah Hosseini, and A. Kianvash. The correlations between processing parameters and magnetic properties of an iron-resin soft magnetic composite. *J. Magn. Magn. Mater.*, 305:147–151, 2006.

[90] C. Wu, H. Chen, H. Lv, and M. Yan. Interplay of crystallization, stress relaxation and magnetic properties for FeCuNbSiB soft magnetic composites. *J. Alloys Compd.*, 673:278–282, 2016.

[91] K. S. Narasimhan, F. G. Hanejko, and M. L. Marucci. Effect of particle size and 2P2C technology on the soft magnetic properties of composite iron compacts. In *APMA International Conference, Yokohama, Japan*, page 7p, October 2012.

[92] A. Krings, M. Cossale, A. Tenconi, J. Soulard, A. Cavagnino, and A. Boglietti. Characteristics comparison and selection guide for magnetic materials used in electrical machines. In *2015 IEEE International Electric Machines  Drives Conference (IEMDC)*, pages 1152–1157, 2015.

[93] A. H. Taghvaei, A. Ebrahimi, M. Ghaffari, and K. Janghorban. Investigating the magnetic properties of soft magnetic composites based on mechanically alloyed nanocrystalline Fe-5wt% Ni powders. *J. Magn. Magn. Mater.*, 323:150–156, 2011.

[94] C. Suryanarayana and C. C. Koch. Nanocrystalline materials – current research and future directions. *Hyperfine Interact.*, 130:5–44, 2000.

[95] M. Huang, C. Wu, Y. Jiang, and M. Yan. Evolution of phosphate coatings during high-temperature annealing and its influence on the Fe and FeSiAl soft magnetic composites. *J. Alloys Compd.*, 644:124–130, 2015.

[96] G. Zhao, C. Wu, and M. Yan. Evolution of the insulation matrix and influences on the magnetic performance of Fe soft mangetic composites during annealing. *J. Alloys Compd.*, 685:231–236, 2016.

[97] B.D. Cullity and C.D. Graham. *Introduction to Magnetic Materials*. Wiley Press, 2nd edition, 2008.

[98] M. D. Scafetta, Y. Xie, M. Torres, J. E. Spanier, and S. J. May. Optical absorption in epitaxial $La_{1-x}Sr_xFeO_3$ thin films. *Applied Physics Letters*, 102:081904, 2013.

[99] G. Q. Gong, A. Gupta, G. Xiao, W. Qian, and V. P. Dravid. Magnetoresistance and magnetic properties of epitaxial magnetite thin films. *Phys. Rev. B*, 56(9), 1997.

[100] Ancorsteel 1000C Datasheet. www.gkngroup.com/hoeganaes, Hoeganaes Corporation, 2017.

[101] Spex Sample Prep: Laboratory Equipment for Sample Preparation and Handling.

[102] K. J. Sunday, K. A. Darling, F. G. Hanejko, and M. L. Taheri. $Al_2O_3$ and $Fe_3O_4$ coated SMCs: Effect of coating material and milling time on magnetic and mechanical properties. *PowderMet Conference Proceedings*, April 2015.

[103] B. D. Cullity. *Elements of X-ray Diffraction*. Addison-Wesley Publishing Company, Inc., 1956.

[104] S. Vives, E. Gaffet, and C. Meunier. X-ray diffraction line profile analysis of iron ball milled powders. *Mater. Sci. Eng., A*, 366(2):229–238, 2004.

[105] M. Bjorck. GenX: an extensible X-ray reflectivity refinement program utilizing differential evolution. *Journal of Applid Crystallography*, 40:1174, 2007.

[106] L. Reimer. *Scanning Electron Microscopy*. Springer, 2nd edition, 1998.

[107] P. W. Hawkes and J. C. H. Spence, editors. *Science of Microscopy*, volume 1. Springer, 2007.

[108] J.M.D. Coey. *Magnetism and Magnetic Materials*. Cambridge, 2009.

[109] Standard test method for direct current magnetic properties of low coercivity magnetic materials using hysteresisgraphs. ASTM Standard A773/773M, ASTM International, 2017.

[110] Standard test method for alternating-current magnetic properties of toroidal core specimens using the voltmeter-ammeter-wattmeter method. ASTM Standard A927/927M, ASTM International, 2017.

[111] Standard test method of apparent density of free–flowing metal powders using the Hall flowmeter funnel. ASTM Standard B212, ASTM International.

[112] Standard test methods for flow rate of metal powder using the Hall flowmeter funnel. ASTM Standard B213, ASTM International.

[113] Standard test method for green strength of specimens compacted from metal powders. ASTM Standard B312, ASTM International.

[114] R. Prescott and M. J. Graham. The formation of aluminum oxide scales on high-temperature alloys. *Oxid. Met.*, 38(3/4), 1992.

[115] F. Jay, V. Gauthier, and S. Dubois. Iron particles coated with alumina: synthesis by a mechanofusion process and study of the high-temperature oxidation resistance. *J. Am. Ceram. Soc.*, 89(11):3522–3528, 2006.

[116] D. A. Porter, K. E. Easterling, and M. Y. Sherif. *Phase Transformations in Metals and Alloys*. Taylor Francis Group, 3rd ed. edition, 2009.

[117] Q. Li, V. Rudolph, B. Weigl, and A. Earl. Interparticle van der Waals force in powder flowability and compactibility. *International Journal of Pharmaceutics*, 280:77–93, 2004.

[118] J. I. Langford and A. J. C. Wilson. Scherrer after sixty years: A survey and some new results in the determination of crystallite size. *Journal of Applid Crystallography*, 11:102–113, 1978.

[119] T. H. De Keijser, J. I. Langford, E. J. Mittemeijer, and A. B. P. Vogels. Use of the Voigt function in a single-line method for the analysis of X-ray diffraction line broadening. *Journal of Applid Crystallography*, 15:308–314, 1982.

[120] H. Shin, S. Lee, H. .S. Jung, and J.-B. Kim. Effect of ball size and powder loading on the milling efficiency of a laboratory-scale wet ball mill. *Ceram. Int.*, 39:8963–8968, 2013.

[121] R. K. Khatirkar and B. S. Murty. Structural changes in iron powder during ball milling. *Mater. Chem. Phys.*, 123:247–253, 2010.

[122] K. Konopka and A. Ozięblo. Microstructure and the fracture toughness of the $Al_2O_3$-Fe composites. *Mater. Charact.*, 46:125–129, 2001.

[123] Y.L. Huang, D. S. Xue, P. H. Zhou, Y. Ma, and F. S. Li. $\alpha$-Fe-$Al_2O_3$ nanocomposites prepared by sol-gel method. *Materials Science and Engineering A*, 359:332–337, 2003.

[124] Z. Li J. Ma, J. Hu and C.-W. Nan. Recent progress in multiferroic magnetoelectric composites: from bulk to thin films. *Adv. Mater.*, 23(9):1062–1087, 2011.

[125] J. S. Moodera, J. Nassar, and G. Mathon. Spin-tunneling in ferromagnetic junctions. *Annual Review of Materials Science*, 29:381–432, 1999.

[126] J. M. Slaughter. Materials for Magnetoresistive Random Access Memory. *Annual Review of Materials Science*, 39:277–296, 2009.

[127] H. Yamada, Y. Ogawa, Y. Ishii, H. Sato, M. Kawasaki, H. Akoh, and Y. Tokura. Engineered interface of magnetic oxides. *Science*, 305:646–648, 2004.

[128] X. Jin, C. McEvoy, and I. Shvets. Studies of heteroepitaxial growth of $Fe/MgO/Fe_3O_4$ multilayer MgO (100) substrates for fabrication of magnetic tunnel junctions. *J. Magn. Magn. Mater.*, 286:128–133, 2005.

[129] R.-G. Huang and J. R. Heath. Silicon nanowire charge-trap memory incorporating self-assembled iron oxide quantum dots. *Small*, 8(22):3417–3421, 2012.

[130] S. Vangelista, R. Mantovan, S. Cocco, A. Lamperti, O. Salicio, and M. Fanciulli. Chemical vapor deposition growth of $Fe_3O_4$ thin films and $Fe/Fe_3O_4$ bi-layers for their integration in magnetic tunnel junctions. *Thin Solid Films*, 520(14):4617–4621, 2012.

[131] F. Greullet, E. Snoeck, C. Tiusan, M. Hehn, D. Lacour, O. Lenoble, C. Magen, and L. Calmels. Large inverse magnetoresistance in fully epitaxial $Fe/Fe_3O_4/MgO/Co$ magnetic tunnel junctions. *Applied Physics Letters*, 92(5):53508, 2008.

[132] T. Kado, H. Saito, and K. Ando. Room-temperature magnetoresistance in magnetic tunnel junctions with $Fe_3O_4$ electrode. *J. Appl. Phys.*, 101:09J511, 2007.

[133] A. A. Shokri, Z. H. Ebrahiminejad, and S. F. Masoudi. The interfacial roughness effect on spin-dependent transport in nonplanar junctions with double magnetic barriers. *Thin Solid Films*, 519:2193–2200, 2011.

[134] S. R. Spurgeon, J. D. Sloppy, R. Tao, R. F. Klie, S. E. Lofland, J. K. Baldwin, A. Misra, and M. L. Taheri. A study of the effect of iron island morphology and interface oxidation on the magnetic hysteresis of Fe-MgO (001) thin film composites. *J. Appl. Phys.*, 112:013905, 2012.

[135] T. J. Moran and B. Lüthi. Elastic and magnetoelastic effects in magnetite. *Phys. Rev.*, 187:710, 1969.

[136] R. V. Chopdekar, B. B. Nelson-Cheeseman, M. Liberati, E. Arenholz, and Y. Suzuki. Role of magnetic anisotropy in spin-filter junctions. *Phys. Rev. B*, 83:224426, 2011.

[137] J. Orna, L. Morellon, P. Algarabel, J. Pardo, S. Sangiao, C. Magen, E. Snoeck, J. De Teresa, and M. Ibarra. $Fe_3O_4/MgO/Fe$ heteroepitaxial structures on magnetic tunnel junctions. *IEEE Trans. Magn.*, 44(11):2862, 2008.

[138] F. Bonell, S. Andrieu, C. Tiusan, F. Montaigne, E. Snoeck, B. Belhadji, L. Calmels, F. Betran, P. Le Fevre, and A. Taleb-Ibrahimi. Influence of misfit dislocations on the magnetoresistance of MgO-based epitaxial magnetic tunnel junctions. *Phys. Rev. B*, 82:092405, 2010.

[139] G. H. Jaffari, A. K. Rumaiz, J. C. Woicik, and S. I. Shah. Influence of oxygen vacancies on the electronic structure and magnetic proeprties of $NiFe_2O_4$ thin films. *J. Appl. Phys.*, 111:093906, 2012.

[140] Y. Y. Huang, C. Liu, and G. P. Flecher. Magnetization of ultrathin bcc Fe films on MgO. *Phys. Rev. B*, 47(1):183–188, 1993.

[141] J. Orna, P. A. Algarabel, L. Morellon, J. A. Pardo, J. M. de Teresa, R. Lopez Anton, F. Bartolome, L. M. Garcia, J. Bartolome, J. C. Cezar, and A. Wildes. Origin of the giant magnetic moment in epitaxial $Fe_3O_4$ thin films. *Phys. Rev. B*, 81:144420, 2010.

[142] K. Matsubara, M. Ohtake, F. Kirino, and M. Futamoto. Microstructure and magnetic properties of Fe and Fe-alloy thin films epitaxially grown on MgO (100) substrates. *Journal of Physics: Conference Series*, 203, 2011.

[143] G. Dixit, J. P. Singh, R. C. Srivastava, H. M. Agrawal, R. J. Choudhary, and A. Gupta. Structural and magnetic behavior of $NiFe_2O_4$ thin film grown by pulsed laser deposition. *Indian Journal of Pure Applied Physics*, 48:287–291, 2010.

[144] J. M. Teixeira, R. F. A. Silva, J. Ventura, A. M. Pereira, F. Carpinteiro, J. P. Araujo, J. B. Sousa, S. Cardoso, R. Ferreira, and P. P. Freitas. Domain imaging, MOKE and magnetoresistance studies of CoFeB films for MRAM applications. *Mater. Sci. Eng., B*, 126:180–186, 2006.

[145] T. Nagahama, H. Kubota, and S. Yuasa. Growth and magnetic properties of ultrathin $Ni_{1+x}Fe_{2-x}O_4$ films for spin filter junctions. *Thin Solid Films*, 519:8239–8242, 2011.

[146] E. F. Rauch, J. Portillo, S. Nicolopoulos, D. Bultreys, S. Rouvimov, and P. Moeck. Automated nanocrystal orientation and phase mapping in the transmission electron microscope on the basis of precession electron diffraction. *Zeits. Kristallogr.*, 225:103–109, 2010.

[147] R. Zuberek, K. Fronc, W. Paszkowicz, and H. Szymczak. Magnetic anisotropy and magnetoelastic constants of ultrathin Fe/GaAs (001) films sputtered in hydrogen atmosphere. *J. Magn. Magn. Mater.*, 283:28–33, 2004.

[148] S. Kale, S. Bhagat, S. Lofland, T. Scabarozi, S. Ogale, A. Orozco, S. Shinde, T. Ventkatesan, B. Hannoyer, B. Mercey, and W. Prellier. Film thickness and temperature dependence of the magnetic properties of pulsed-laser-deposited $Fe_3O_4$ films on different substrates. *Phys. Rev. B*, 64:205413, 2001.

[149] F. C. Voogt, T. T. M. Palstra, L. Niesen, O. C. Rogojanu, M. A. James, and T. Hibrma. Superparamagnetic behavior of structural domains in epitaxial ultrathin magnetite films. *Phys. Rev. B*, 57:R8107, 1998.

[150] R. Shomski and J. Coey. Giant energy product in nanostructured two-phase magnets. *Phys. Rev. B*, 48:15817, 1993.

[151] K. Zakeri, T. Khebe, J. Lindner, and M. Farle. Magnetic anisotropy of Fe/GaAs (001) ultrathin films investigated by in situ ferromagnetic resonance. *J. Magn. Magn. Mater.*, 299:L1, 2006.

[152] E. Schlomann. Spin-wave analysis of ferromagnetic resonance in polycrystalline ferrites. *J. Phys. Chem. Solids*, 6:257, 1958.

[153] I. Bernal-Villamil and S. Gallego. Electronic structure and polaronic charge distributions of Fe vacancy clusters in $Fe_{1-x}O$. *Phys. Rev. B*, 90:195126, 2014.

[154] Y. Peng, Y. Yi, L. Li, H. Ai, X. Wang, and L. Chen. Fe-based soft magnetic composites coated with NiZn ferrite prepared by a co-precipitation method. *J. Magn. Magn. Mater.*, 428:148–153, 2017.

[155] M. Strečková, R. Bureš, M. Fáberová, P. Kurek, P. Roupcova, H. Hadraba, V. Girman, and J. Strecka. A novel composite material designed from FeSi powder and $Mn_{0.8}Zn_{0.2}Fe_2O_4$ ferrite. *Advances in Materials Science and Engineering*, 2015.

[156] K. J. Sunday and M. L. Taheri. Soft magnetic composites: recent advancements in the technology. *In press, Corrected proof: Metal Powder Report*, 2016.

[157] S. A. Howard and K. D. Preston. Profile fitting of powder diffraction patterns: Review of mineralogy. *Mineralogical Society of America, Washington, DC*, 20, 1989.

[158] D. R. Lide, editor. *Handbook of Chemistry and Physics*. CRC Press, New York, USA, 2008.

[159] S. Nakahara, E. A. Périgo, Y. Pittini-Yamada, Y. de Hazan, and T. Graule. Electric insulation of FeSiBC soft magnetic amorphous powder by a wet chemical method: Identification of the oxide layer and its thickness control. *Acta Materialia*, 58(17):5695–5703, October 2010.

[160] Gkn sinter metals develops motor using smc materials, July/August 2013.

[161] C. Oikonomou, D. C. Gutierrez, M. Monclus, J. M. Molina-Adareguia, and L. Nyborg. Assessment of the compacting and annealing process steps on the performance of finished soft magnetic composite components. *Euro PM2015 - Functional Materials*, 2015.

[162] D. R. G. Mitchell. *Microscopy Research and Technique*, 71:588–593, 2008.

[163] J. Smit and H. P. J. Wijn. *Ferrites*. Cleaver-Hume Press Ltd., 1959.

[164] M. C. Dimri, A. Verma, S. C. Kashyap, D. C. Dube, O. P. Thakur, and C. Prakash. Structural, dielectric and magnetic properties of NiCuZn ferrite grown by citrate precursor method. *Mater. Sci. Eng., B*, 133(1-3):42–48, 2006.

[165] M. L. Taheri, E. E. Carpenter, V. Cestone, M. M. Miller, M. P. Raphael, M. E. McHenry, and V. G. Harris. Magnetism and structure of $Zn_xFe_{3-x}O_4$ films processed via spin-spray deposition. *J. Appl. Phys.*, 91(10):7595, 2002.

[166] Resonant Acoustic Mixing: Coating of Micron Materials With Nanopowder. Technical report, Resodyn$^{TM}$ Acoustic Mixers, Inc., 2017.

[167] E. Rezlescu, L. Sachelarie, P. D. Popa, and N. Rezlescu. Effect of substitution of divalent ions on the electrical and magnetic properties of Ni–Zn–Me ferrites. *IEEE Trans. Magn.*, 36(6):3962–3967, 2000.

# Vita

**Katie Jo Sunday**

## Education

- PhD – Materials Science and Engineering – Drexel University, Philadelphia, PA – June 2017
- M.S. – Materials Science and Engineering – Drexel University, Philadelphia, PA – June 2014
- B.S. – Mechanical Engineering – Polytechnic Institute of NYU, Brookyln, NY – May 2012

## Research Experience

- Graduate Research Assistant – Drexel University, Philadelphia, PA
  Advisor: Dr. Mitra L. Taheri – 2012-2017
- Technology Summer Intern – Carpenter Technology, Reading, PA
  Mentor: Dr. Ryan DiSabella – 2010-2011

## Honors and Awards

- Books and Bagels Presenter – Office of Graduate Studies, Drexel University – 2016
- Outstanding Student Award – Alumni Association, Drexel University – 2016
- Young Member Award – ASM Philadelphia Liberty Bell Chapter – 2016
- Teaching Excellence Award – Office of Graduate Studies, Drexel University – 2016
- Alpha Sigma Mu Honor Society Inductee – Philadelphia Chapter, Drexel University – 2015
- Higher Education Advocate Travel Award (HEATA) – Office of Graduate Studies, Drexel University – 2015
- Teaching Excellence Award – Highly Commended – Office of Graduate Studies, Drexel University – 2015
- C.F. Burns Student Poster Contest ($1^{st}$ place) – ASM Philadelphia Liberty Bell Chapter – 2015

## Teaching Experience

- Graduate Teaching Fellow – ENGR 101, 102, 103 – Freshman Engineering Design Lab – College of Engineering, Drexel University – 2014-2017
- Camp Leader and Organizer – ASM Philadelphia Liberty Bell Chapter Materials Camp – Drexel University – 2013-2015
- Lab Instructor and Grader – MATE 366 – Processing of Metallic Materials – Materials Science and Engineering Department, Drexel University – 2012-2014
- Lab instructor – MATE 541 – Introduction to Transmission Electron Microscopy – Materials Science and Engineering Department, Drexel University – 2013